Spring 5-7-2021

Circulation and Transport Timescales in Tidally Dominated Estuaries

Sohaib Alahmed
University of Maine, sohaib.alahmed@maine.edu

CIRCULATION AND TRANSPORT TIMESCALES IN TIDALLY DOMINATED ESTUARIES

By

Sohaib Alahmed

B.A. University of Mosul, 2011

M.S. University of Maine, 2017

A DISSERTATION

Submitted in Partial Fulfillment of the

Requirements for the Degree of

Doctor of Philosophy

(in Civil and Environmental Engineering)

The Graduate School

The University of Maine

May 2021

Advisory Committee:

Lauren Ross, Assistant Professor of Civil and Environmental Engineering, Advisor

Bill Davids, Professor of Civil and Environmental Engineering

Kimberly Huguenard, Assistant Professor of Civil and Environmental Engineering

Shaleen Jain, Professor of Civil and Environmental Engineering

Sean Smith, Associate Professor of Earth and Climate Science

Aldo Sottolichio, Professor of Ocean and Continental Environments and Paleoenvironment

CIRCULATION AND TRANSPORT TIMESCALES IN TIDALLY DOMINATED ESTUARIES

By Sohaib Alahmed

Dissertation Advisor: Dr. Lauren Ross

An Abstract of the Dissertation Presented
in Partial Fulfillment of the Requirements for the
Degree of Doctor of Philosophy
(in Civil and Environmental Engineering)
May 2021

The susceptibility of estuaries to pollution has increased in the past few decades due to the increased anthropogenic inputs. The vulnerability of these estuaries to pollution is closely related to the circulation and transport in these estuaries. This work, therefore, aims to understand the transport of water-born materials in tidally dominated estuaries in relation to residual circulation and estuarine shape. The role of river discharge, tide, density gradient, and advection in altering the residual circulation and the transport timescales (flushing and residence time) are investigated. Three-dimensional hydrodynamic Eulerian-Lagrangian models are developed considering mesotidal (2 m <tidal range <4 m) and macrotidal (tidal range >4 m) estuaries as the tidal could be significant compared to the mean flow. The Frenchman Bay (a mesotidal) in Maine, USA, and The Gironde estuary (macrotidal) in France are considered as study sites. The results show that density gradient and river discharge can be an important driver for the residual circulation and the flushing in wide estuaries with relatively simple geometry (simple bed profile and no constriction, headlands, or island). The results also demonstrate that the density gradient is more important to the transport than the river discharge in mesotidal

estuaries and the river discharge is more important than the density gradient in macrotidal estuaries due to the increase of friction. The presence of complex morphological features gives arise for the advection to drive the residual circulation in estuaries and may affect the transport timescale. It is shown that advection can decrease the flushing time by 100% at the location where advection dominates the creation of residual circulation.

It is shown that the residual circulation can be complex. Regardless of the complexity of the flow in estuaries, it is demonstrated that it is possible to predict what mechanism (river, tide, density gradient) drive the transport process in estuaries and whether to expect high or low flushing time based on simple metrics such as estuarine width and tidal excursion (the distance traveled by a water parcel over half tidal cycle). Such knowledge can facilitate better water-quality management as it provides a general idea about the transport and the water quality in estuarine environments.

DEDICATION

In the hope that my work may in some way express my love and gratitude to my wife, Anfal Fadhil, and my two kids, Mohammed and Maya, I dedicate this dissertation to them.

ACKNOWLEDGEMENTS

First and foremost, I would like to thank my advisor, Dr. Lauren Ross, for all her help and guidance that she has provided for me over the past four years. Dr. Ross did not only make me a better scientist, but she also brought the best of me. I also wish to acknowledge Dr. Aldo Sottolichio and Dr. Sean smith for their remarkable contribution to my work. Special thanks go to Dr. Shaleen Jain for being a great source of support for me during my academic journey at the University of Maine. I also would like to express my profound gratitude to Dr. Kimberly Huguenard for her insightful questions and critiques. I also wish to let Dr. Bill Davids know that I took a lot of him and his knowledge as he introduced the world of numerical modeling to me. I would like to thank Dr. Neil fisher for his help in the fieldwork and data collection. I also express my gratitude to Dr. Bridie McGreevy and Acadia Aqua Farms for their help and support. Many thanks to my family and my friends and my colleagues to be an amazing part in my journey.

TABLE OF CONTENTS

LIST OF TABLES

LIST OF FIGURES

CHAPTER 1

INTRODUCTION

Estuaries are defined as semi-enclosed bodies of water with connection to the ocean where freshwater from land and salt water from the ocean meet and mix (Cameron & Pritchard, 1963). Examples are the Chesapeake and Delaware Bays in the United States and the Thames Estuary in Britain. Estuaries are vital ecosystems that provide critical habitat for many marine and land species (Costanza et al., 1997), offer a unique environment for aquaculture farms and commercial fishing, and provide critical navigable waterways for commercial and recreational shipping (Bárcena et al., 2017). Besides, a considerable amount of the world's population resides on estuary shorelines, including 22 out of the 32 largest cities in the world (Liu et al., 2020 ; Ross, 1995).

Elevated water quality issues and human activities in estuaries during the 20th century have affected sensitive habitat areas and aquatic communities (Kennish, 1991). This necessitates effective management and careful planning to sustain their ecological, economical, and recreational values (Smolders et al., 2013). Attaining this requires fundamental knowledge of the hydrodynamics of these estuaries and the exchange rate of their water with the adjacent ocean water (Haddout et al., 2020; Huijts et al., 2009). The flow in estuaries exhibits spatial and temporal variation, which influences transport timescales, defined as the time required for a water parcel or dissolved matter to be transported within or out of a specified waterbody, therefore affecting water quality.

The transport of sediment and contaminants, and thus the health of estuaries, depends heavily on the residual circulation (Burchard & Hetland, 2010; Prandle, 2004; Stacey et al., 2001; Wong, 1994). Residual circulation is defined as the velocity averaged over the dominant tidal period (Zimmerman, 1979) and can be referred to as tidally averaged flow or subtidal circulation. Many studies on residual flow (e.g. Burchard et al., 2011; P. Cheng et al., 2011, 2017; Huijts et al., 2009; Jiang & Feng, 2011; Li & O'Donnell, 1997, 2005; Stacey et al., 2001; Wong, 1994 have been developed to understand the residual flow current structure and dynamics (forcing mechanisms) in different types of estuaries (different tidal range, shape, etc.) providing insights on predicting transport regimes and water quality. However, some studies have shown that, besides the residual flow, the oscillating tide can play a role in transporting water-born materials (e.g. contaminants), complicating their motion (Geyer & Signell, 1992; Signell & Butman, 1992; Zimmerman, 1979). Using an idealized model, Zimmerman (1979) showed that particle motion in a field of multiple residual eddies was completely random when the tide was imposed. In this case relying only on residual flows to predict transport pathways or transport timescales is not sufficient, and this proves to be of particular importance in estuaries with complex geometries and strong tidal forcing. Little attention has been dedicated to understanding the interaction between residual flow, tide, and transport in tidal estuaries despite the relevance of the topic to water quality and estuarine management. Thus, the overarching goal of this dissertation is to understand the transport of water-born materials in tidally dominated estuaries in relation to residual circulation and estuarine shape.

To pursue the goal of this dissertation and fill the outlined research gaps, three studies are developed based on mesotidal (2 m > tidal range > 4 m) and macrotidal (tidal range > 4 m)

estuaries of different size, shape, and freshwater input. Three dimensional Eulerian-Lagrangian numerical models were developed for case study locations based on a mesotidal system of estuaries in Downeast Maine, USA, and a macrotidal estuary on the southwest coast of France, which will be elaborated upon in the following sections.

In the remainder of this chapter, section 1.1 provides a theoretical overview of tidal and residual flow, residual flow drivers as well as a brief definition of transport timescales. Sections 1.3 to 1.5 explore the three major studies developed for this thesis highlighting the research gaps and the objectives of each study, and finally, section 1.6 gives an outline of the remainder of the thesis.

1.1 Tidal and Residual Flow in Estuaries.

The current velocity and the transport of tracers such as salinity or temperature in estuaries are governed by the continuity equation, the Naiver-Stokes (N-S) equations, and the conservation of tracers as expressed below (Hervouet, 2007),

$$\frac{\partial u}{\partial \mathrm{x}} + \frac{\partial v}{\partial \mathrm{y}} + \frac{\partial w}{\partial \mathrm{z}} = 0 \qquad 1.1$$

$$\frac{\partial u}{\partial t} + u\frac{\partial u}{\partial x} + v\frac{\partial u}{\partial y} + w\frac{\partial u}{\partial z} = -\frac{1}{\rho}\frac{\partial P}{\partial x} + \frac{\partial}{\partial z}\left(A_z\frac{\partial u}{\partial z}\right) + F_x \qquad 1.2$$

$$\frac{\partial v}{\partial t} + u\frac{\partial v}{\partial x} + v\frac{\partial v}{\partial y} + w\frac{\partial v}{\partial z} = -\frac{1}{\rho}\frac{\partial P}{\partial y} + \frac{\partial}{\partial z}\left(A_z\frac{\partial v}{\partial z}\right) + F_y \qquad 1.3$$

$$\frac{\partial w}{\partial t} + u\frac{\partial w}{\partial x} + v\frac{\partial w}{\partial y} + w\frac{\partial w}{\partial z} = -\frac{1}{\rho}\frac{\partial P}{\partial z} - g + \frac{\partial}{\partial z}\left(A_z\frac{\partial w}{\partial z}\right) + F_z \qquad 1.4$$

$$\frac{\partial T}{\partial t} + u\frac{\partial T}{\partial x} + v\frac{\partial T}{\partial y} + w\frac{\partial T}{\partial z} = \frac{\partial}{\partial z}\left(A_k\frac{\partial T}{\partial z}\right) + Q \qquad 1.5$$

where Eq. 1. 1 is the conservation of mass, Eqs. 1. 2-1. 4 describe the conservation of momentum in the x, y, and z directions respectively, and Eq. 1. 5 expresses the conservation of tracers. In these equations, u, v, and w are the velocities in the x, y, and z directions respectively, ρ denotes the density of water, P refers to pressure, g is gravity (-9.81 m/s^2), A_z and A_k are the vertical eddy viscosity and eddy diffusivity for velocity and tracers respectively, F_x, F_y and F_z are the source or sink of an extra force (e.g. wind and Earth's rotation) in x, y and z directions respectively, Tdenotes the tracer concentration and Q is the source or sink of the tracer, T. By solving the N-S equations, the velocity, water level, and density can be obtained at any point in the considered domain. In this work, the above equations are numerically solved using a Finite Element model as will be described in the following chapters.

The current velocity in any direction (x, y, and z), and at any point in tidal estuaries can be decomposed into an oscillating and mean (residual) component (Zimmerman, 1981) as shown in Figure 1. 1a. This can be expressed using the flowing equation.

$$U = U_o + U_{tide} \qquad 1.6$$

where U_o represents the residual flow and U_{tide} refers to the oscillating current of the tide. The oscillating current can be composed of many harmonics. Herein, the dominant harmonic is the semi-diurnal (M2) astronomical tide which is the dominant tidal constituent in most of the world's oceans that occurs at a period of 12.4 hours (Valle-Levinson, 2010). The semi-diurnal tide is due to the gravitational force of Earth-Moon system. The neap-spring (fortnightly) variation of the tide occurs at period of approximately 14.7 days (Gerkema, 2019), and is a result of the sun, Earth and moon system. Water level is at its highest and the tidal currents are strongest when

the sun and moon are aligned, called spring tide. When the Moon is 90^0 with respect to Earth-Sun system the water levels and tidal currents are minimal, and this is referred to as neap tide (Figure 1. 1b). The residual and tidal currents are obtained by performing a least-squares fit on the current velocities (Foreman & Henry, 1989). The oscillating component of the tide (U_{tide}) can be expressed as a sum of multiple harmonics as follows,

$$U_{tide} = \sum_{j=1}^{M} A_j \cos(\sigma_j t - \phi_j) \qquad 1.7$$

where M is the number of tidal constituents (e.g. M2 tide with 12.42 h period, K1 with 23.93 h period), t is a time vector, A_j, σ_j, and ϕ_j are the amplitude, frequency, and phase of the tidal constituent j respectively. The mean of the oscillating tidal current over a tidal cycle is zero. The residual flow (mean flow) is steady relative to oscillating tide and occurs at frequencies that are less than 1 cycle/day (Valle-Levinson, 2010). More details on this analysis are provided in section 2.3 in Chapter 2 and section 3.2.1 in chapter 3.

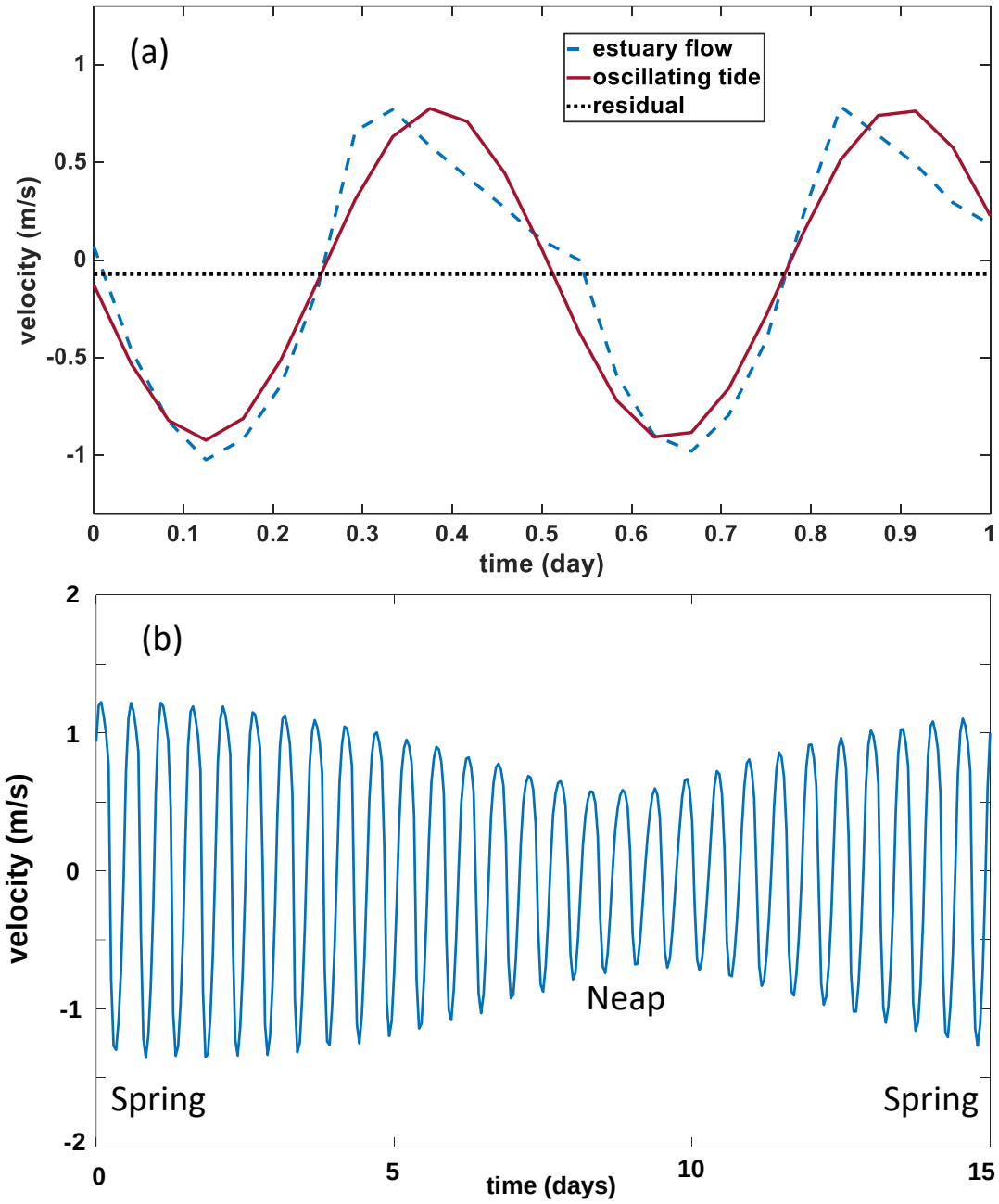

Figure 1. 1. Example diagram of the current velocity in an estuary over one day decomposed into mean (residual) and oscillating component obtained by performing a least squares fit considering only M2 (12.42 h) tide (a), and the current velocity over 15 days highlighting the spring-neap variation of tide (b).

Exploring the tidally-averaged momentum balance helps to understand the dynamics of residual flows in estuaries. For the sake of demonstration and simplicity, only the along channel momentum balance is discussed here. The pressure gradient term ($-\frac{1}{\rho}\frac{\partial P}{\partial x}$) in the along-channel momentum balance (Eq. 1. *2*) can be divided into barotropic and baroclinic pressure gradients as follows (Geyer & MacCready, 2014)

$$-\frac{1}{\rho}\frac{\partial P}{\partial x} = -g\frac{\partial \eta}{\partial x} + \frac{g}{\rho}\int_{-H}^{\eta}\frac{d\rho}{dx}\,dz \qquad 1.\,8$$

where the first and the second terms on the RHS of Eq. 1. *8* are the barotropic and the baroclinic pressure gradients respectively, η is the water free surface elevation and H is the water depth. The tidally averaged momentum equation can be obtained by performing a temporal (tidal) average on Eq. 1. *2*. The tidally averaged along-channel momentum equation considering Eq. 1. *8* and assuming no extra force ($F_x = 0$) reads,

$$\overline{u\frac{\partial u}{\partial x}} + \overline{v\frac{\partial u}{\partial y}} + \overline{w\frac{\partial u}{\partial z}} = -g\frac{\partial \bar{\eta}}{\partial x} + \overline{\frac{g}{\rho}\int_{-H}^{\eta}\frac{d\rho}{dx}\,dz} + \overline{\frac{\partial}{\partial z}\left(A_z\frac{\partial u}{\partial z}\right)} \qquad 1.\,9$$

where the overbar indicates a tidal average.

The first three terms on the left-hand side of Eq. 1. *9* are the advective accelerations. Advection may be defined as the movement of mass entrained in the flow as a result of flow heterogeneity (Chang, 1968; Fitts, 2013). Advection can be a leading order term in the momentum balance when an estuary features complex geometry such as estuary width constrictions or along- and cross-channel bathymetric variations (Alahmed et al., 2020; Basdurak & Valle-Levinson, 2012; P. Cheng & Valle-Levinson, 2009; Scully et al., 2009). A non-uniform flow

in the horizontal plane (*x* and *y*) in a simplified channel is considered in Figure 1. 2. The flow field in the channel is described by two velocity components: u the longitudinal (along-channel) velocity, and v the lateral (across-channel) velocity. The longitudinal divergence of the along channel velocity $\frac{\partial u}{\partial x}$ (which has a positive value in Figure 1. 2) is transported downstream by the longitudinal velocity u (which also has a positive value) resulting in a positive value of the longitudinal advective term ($u\frac{\partial u}{\partial x}$) and the slower moving water is advected over the faster moving water, attenuating the downstream flow.

The same concept applies when considering a positive lateral advection $v\frac{\partial u}{\partial y}$. When transporting the positive lateral divergence of the longitudinal velocity ($+\frac{\partial u}{\partial y}$) by a positive lateral velocity ($+v$) shown in Figure 1. 2, the downstream flow in this case is attenuated due to the positive lateral advection at that location. This is because the relatively slower along channel velocity u is advected over a relatively faster one causing flow attenuation. To generalize, positive advective accelerations in Eq. 1. *9* result in local flow attenuation while negative advection value results in enhancing (strengthening) the local flow.

As demonstrated above, advection results due to flow heterogeneity which is induced by the interaction of the flow with the boundaries (channel morphology). Models based on simplified shape with no advection, therefore, may fail in describing the residual flow in estuaries of complex bathymetry (notable change in the channel depth).

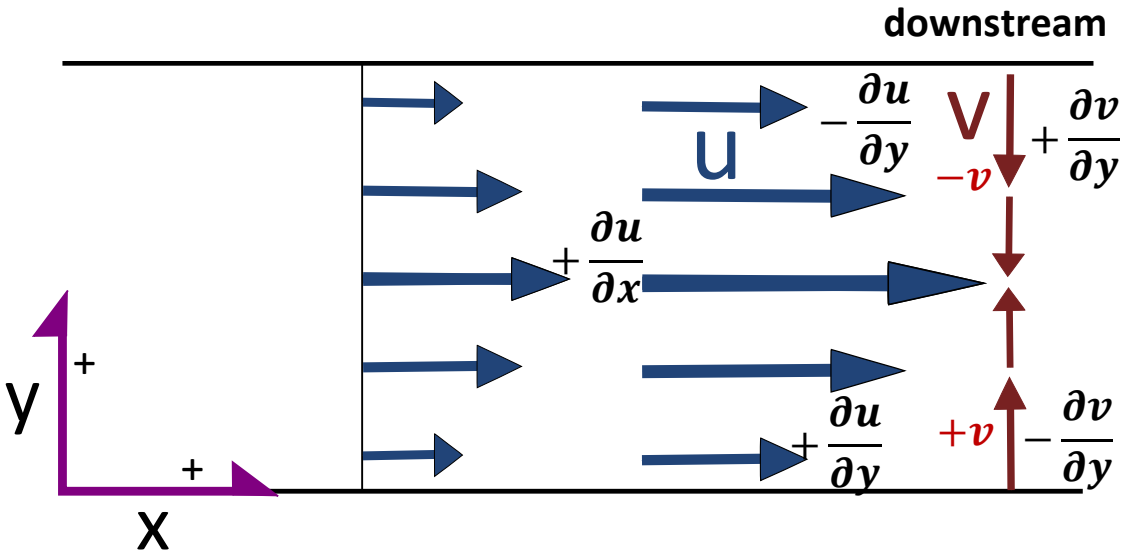

Figure 1. 2. A 2-dimentional flow field with longitudinal (u) and lateral (v) velocity components in a simplified channel. The arrows' head refers to the flow direction while the arrows' length refers to the magnitude of the flow.

In estuaries, the density difference between the salty ocean water and the freshwater from the river (Figure 1. 3a) induces the baroclinic pressure gradient (the second term on the RHS of Eq. 1. 9) and results in a vertically sheared flow with a landward flow in the bottom layer and seaward flow in the surface layer as portrayed in Figure 1. 3b. This flow is induced due to the balance between the barotropic pressure gradient, baroclinic pressure gradient and friction. Theoretically, the baroclinic pressure gradient induces a landward (in-estuary) flow that has a zero value at the surface (depth is zero) and maximum value near the bottom (maximum depth) assuming no bottom drag as detailed in Figure 1. 3d. This baroclinic flow engenders a seaward tilt in the water free surface elevation (to conserve mass), creating the barotropic pressure gradient (the first term on the RHS of Eq. 1. 9). The latter produces a vertically uniform (assuming no bottom drag) and seaward flow compensating the landward flow due to the baroclinic pressure gradient as shown in Figure 1. 3c.

The barotropic pressure gradient can be also generated by the river discharge and/or by the barotropic tide (Li & O'Donnell, 1997). Due to the bottom friction and viscous nature of the water, the pressure gradients, as well as other drivers (i.e. advection), are balanced by the stress divergence term (the third term on the RHS of Eq. 1. 9) and shown in Figure 1. 3e.

Other mechanisms such as Coriolis accelerations due to Earth's rotation and centrifugal accelerations due to channel curvature can be included in the momentum equations. These terms become particularly influential in forcing lateral (or secondary) residual flows (Chant, 2002). As this study focuses on the longitudinal residual flow, Coriolis and curvature are not of leading order and are therefore briefly discussed in chapter 3.

1.2 Transport Timescales

The water quality of aquatic systems can be assessed by transport time scales. These timescales are quantified by using Lagrangian particle tracking where fluid parcels and their properties are tracked as they move from one point to another in space (Zimmerman, 1979). The timescales can be defined as flushing time, residence time and age (Lucas, 2010).

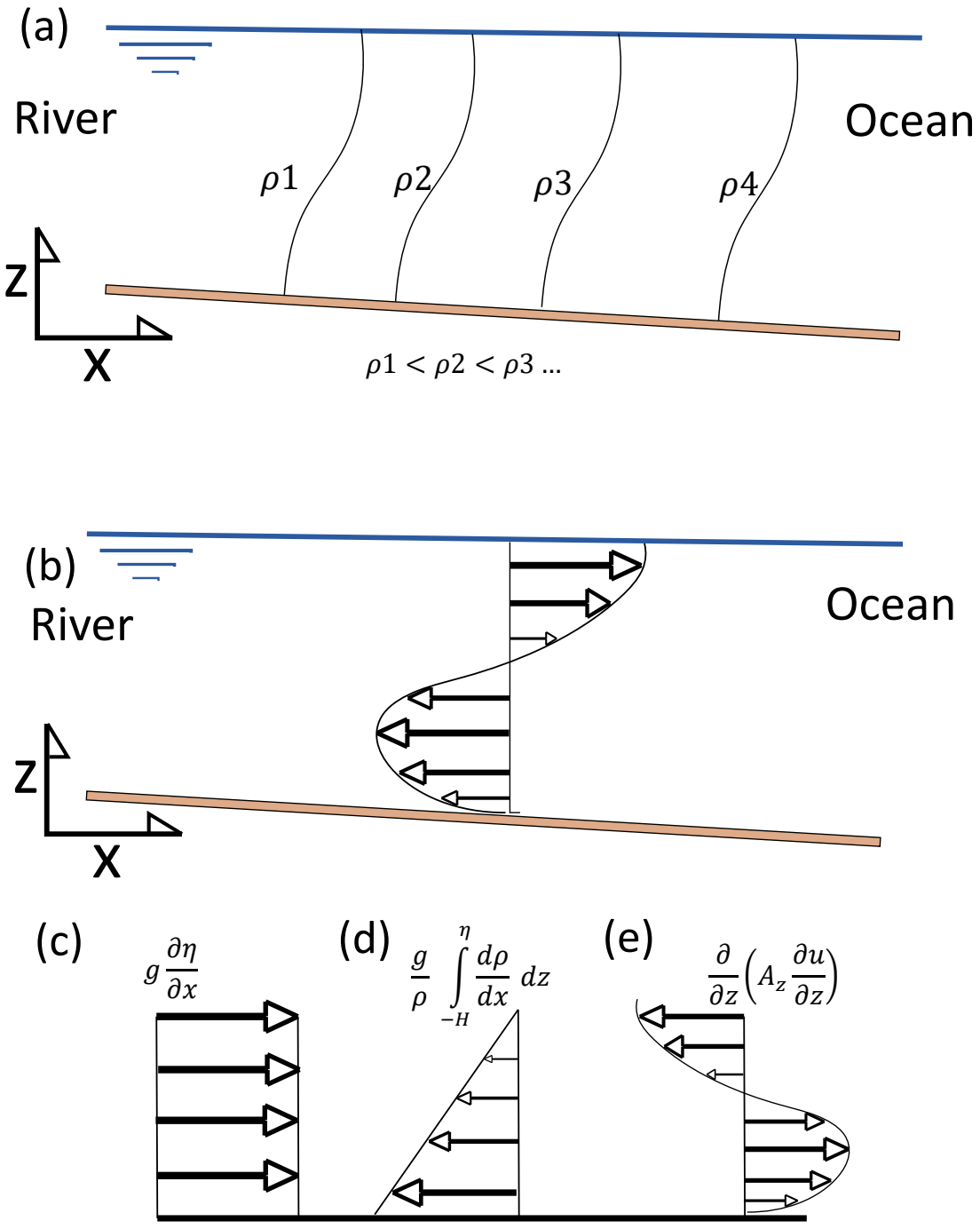

Figure 1. 3. A conceptual plot of density distribution in the vertical plane depicted by isopycnals (a) and the resultant flow (b) induced by the barotropic (c) $g\frac{\partial \eta}{\partial x}$ and baroclinic (d), $\frac{g}{\rho}\int_{-H}^{\eta}\frac{d\rho}{dx}\,dz$ pressure gradients as well as the stress divergence $\frac{\partial}{\partial z}\left(A_z\frac{\partial u}{\partial z}\right)$ (e). The arrows' head refers to the direction of the flow and the arrows' size refers to the magnitude of the flow.

Flushing time is defined as the time required to renew the initial water mass in a waterbody. It measures the overall behavior of the aquatic systems and, therefore, provides no spatial detail on the transport processes inside a given system (Monsen et al., 2002). Practically, estuaries with short flushing times are less vulnerable to pollution as they quickly exchange the estuary water with new water from the adjacent coastal ocean (John et al., 2020). The flushing time is quantified by tracking the evolution of the total water mass (total number of particles) initially found in the water body until most of the mass (particles) permanently leave the system. Residence time is the time needed for a water particle found anywhere in a waterbody to leave that system (Zimmerman, 1976). Residence time provides spatial information on transport timescales within the estuarine domain. Estuary regions with relatively short residence times are less likely to have water quality issues than regions with high residence times (Kenov et al., 2012). The residence time is quantified by tracking each water particle individually from an initial location until they exit the system for the first time.

The transport of tracer is dictated by Eq. 1. *5*. However, for the transport of the Lagrangian particles, the impact of diffusion as well as the sink and source terms (RHS of Eq. 1. *5*.) are not considered in this work. The three-dimensional position of any Lagrangian particle is described by the following equations,

$$X^{n+1} = X^n + \Delta t\, u \qquad 1.\ 10$$

$$Y^{n+1} = Y^n + \Delta t\, v \qquad 1.\ 11$$

$$Z^{n+1} = Z^n + \Delta t\, w \qquad 1.\ 12$$

where X, Y and Z are the three-dimensional coordinates of a particle, n is the time step-index and Δt is the time step. Note that no diffusion is assigned to the Lagrangian particles and therefore the motion is influenced only by the flow field and no particle separation may occur due to the diffusion effect. Previous studies have adopted the random walk approach to account for diffusion impact on particles motion (Du et al., 2020; Zimmerman, 1979). Introducing the diffusion process to Eq. 1. 10, for example, reads

$$X^{n+1} = X^n + \Delta t\, u + R\sqrt{C\, K_x\, \Delta \mathrm{t}} \qquad 1.\ 13$$

were R is a uniform random number between -1 to 1, C is a constant number, K_x is the diffusion coefficient (m^2/s) in the x direction. The expression in Eq. 1. 13 indicates that the motion of the particles may occur even in case of still water (zero velocity) through diffusion effect. Examples of this phenomena are dye dilution and salinity diffusion in a still water. The particle transport in this work also does not account for the production or decay associated with biomass transport (i.e. the particles in this work does not dye or produce). The production or decay rate depends on multiple factors such as temperature, salinity, sun light (UV radiation), predation, and nutrients (Bordalo et al., 2002). Therefore, estimating the production or decaying rate may depends of the type of the biomass (e.g. bacterial, phytoplankton, etc.). Once the production and decaying rate are known, one can estimate the number of the particles in a given estuarine region as follows,

$$Np^{n+1} = Np^n + P\, Np^n - D\, Np^n + Qp\, \Delta t \qquad 1.\ 14$$

Where Np denotes the number of the particles at any time in a given estuarine domain, P and D is the production and decaying rate of the particles and Qp is the number of particles that enter

or leave the domain over a certain time. Other particles feature considered in this study is that the particles are neutrally buoyant (i.e. they particles motion is not affected by the density of water). The particles outcome in this research may be interpreted with care.

Though, the transport of tracers and biomass (e.g. bacteria) may be under predicted by the Lagrangian approach adopted in this study due to the limitation mentioned above, the Lagrangian analysis in this study is important to draw a general understanding on the transport process in estuaries (Van Sebille et al., 2018).

The following subsection provides details regarding specific research gaps and objectives in relation to residual flow and transport timescales.

1.3 Residual Flow and Coastal Transport Timescales in Mesotidal Estuaries of Different Geometries

Elevated river discharge can alter the circulation in estuaries, which has been found to decrease evacuation times of the freshwater inflow into the coastal ocean (Du et al., 2020). However, this can be complicated by the interaction of the river discharge, density gradients, tide, and bathymetry. Chapter 2 describes the residual circulation, flushing times and residence times in mesotidal estuaries with varying levels of geometric complexity and river discharge. The systems studied are all dynamically 'short', which is defined as the tidal excursion (distance a water particle will travel over ½ tidal cycle) being of the same order of the length of the estuary.

The impact of river discharge on residence time in the Caloosahatchee Estuary in the Gulf of Mexico was investigated by Wan et al. (2013) using a three dimensional numerical model. They found that when the river discharge increased from 0 to 283 $m^3 s^{-1}$, the average estuarine

residence time decreased from 60 days to 5 days. Additionally, they demonstrated that the region of maximum residence time in the estuary migrated downstream as the river discharge increased. Also, based on observations in the Sumjin River Estuary on the south coast of Korea, Shaha et al. (2012) showed that the flushing time varied with river discharge from 15 days to 5 days as it increased from 5 to 80 $m^3 s^{-1}$. Shaha et al. (2012) also investigated the impact of the fortnightly variability of the tide on flushing time (spring-neap cycle). They found that during spring tide the flushing time is close to the semidiurnal (12.42 h) tidal period and is twice as long during neap tide.

In their study on Willapa Bay in Washington, USA, Banas & Hickey (2005) indicated that the presence of complex morphological features (e.g. constrictions, curvature, etc.) along estuaries can be of importance in driving the transport of particles and the exchange of water masses in and between estuaries. Another key factor that affects transport processes includes density gradients, which are typically driven by changes in salinity in coastal areas due to the input of fresh water from rivers mixing with salty ocean water. Meyers & Luther (2008) in their study on Tampa Bay in Florida, USA, showed that during periods when density-induced circulation peaks, the flushing time of the system reduces by a factor of 4 (from 156 to 36 days).

The above-mentioned studies have led us to understand what mechanisms are influential in altering transport timescales in specific estuarine systems. To date, however, it is still unclear why estuaries of varying morphology have different transport timescales and residual flow patterns when freshwater input is elevated, or tidal forcing is varied. The goal of this study, therefore, is to link residual flow structure to transport timescales considering the impact of

freshwater input, tide, and estuarine morphology. To reach this goal, the objectives of this study are to 1) Identify and generalize relations between estuary tidal dynamics, density gradients, freshwater inflows, and particle transport timescales through hydrodynamic scenario simulations, and to 2) Generalize the relationship between the hydrodynamics and coastal geomorphological conditions. The latter will provide better guidance for coastal resource managers to scale up observations and implement strategies for monitoring and response to pollution problems in varied coastal settings. Now, the residual circulation and the transport timescales in estuaries with length that is an order of magnitude longer than the tidal excursion will be investigated.

1.4 Residual Flow in a Macrotidal Estuary

The density gradient can play a major role in altering the residual circulation and the transport of sediment in macrotidal and convergent estuaries. Nonetheless, Allen et al. (1980) suspected that tidal processes can be as or more important than density processes in macrotidal and convergent estuaries. To date, this has not yet been confirmed. Chapter 3 investigates residual flow patterns and forcing mechanisms along a macrotidal estuary where the tidal excursion is an order of magnitude less than the length of the system.

In the macrotidal and convergent Gironde estuary, Ross et al. (2017) found that cross-channel variations in tidal nonlinearities (advective accelerations) affected the lateral strength and structure of subtidal flows and that this effect varied from neap to spring tide. This result was surprising since previous work on this system (Allen, 1980) indicated that subtidal flows were solely a product of along-channel density gradients. The transverse variation in strength and structure of residual flows has been found to be affected by bathymetry, channel width, and

depth and (Chant, 2002; Li & O'Donnell, 1997, 2005; Valle-Levinson et al., 2003; Wong, 1994; J T F Zimmerman, 1978). A study by Burchard et al (2011) showed that in tidally energetic estuaries with a parabolic cross-channel shape (idealized), the density gradients create a laterally sheared flow in shallow channels and vertically sheared flow in the deep channels. The study also showed that advective accelerations produce a laterally sheared flow with inflow in the channel and outflow over the shoals, and that the relative contribution of advection-induced flow to the total residual circulation increases as the channel narrows and deepens. Idealized estuary-based studies have provided crucial insight on how residual flow magnitude and structure, and the relative contribution of individual driving mechanisms, are affected by lateral and longitudinal changes in bathymetry, tide, and freshwater input (salinity gradients). It is still unclear how along-channel residual flow pattern and individual driving mechanisms (terms in the along channel momentum balance, Eq. 1. 9) evolve along a macrotidal and convergent estuary with realistic geometry in response to change in bathymetry. Therefore, the goal of Chapter 3 is to determine the longitudinal and transverse variation of along-channel residual flow structure and forcing mechanisms in a macrotidal and convergent estuary using realistic bathymetry. The objectives of Chapter 3 study are to 1) Investigate the along-channel variation of the residual flow structure and driving mechanisms, 2) Determine the relative contribution of density gradients to the total residual circulation, and 3) Evaluate the relative importance of advection to the along-channel momentum balance in response to the along-channel variation in estuarine geometry.

1.5 Transport Timescales in a Macrotidal Estuary

Residual flow structure was found to vary along a macrotidal and convergent estuary due to changes in estuarine bathymetry modifying the influence of residual flow forcing mechanisms

(Alahmed et al., 2020). The change in residual flow structure and drivers along an estuary could manifest in transport timescales, which directly affects water quality in estuaries. Chapter 4 investigates the flushing and residence time in a macrotidal and convergent estuary and aims to determine if there is a link between along-channel variations in residual flow structure and drivers, as described in Chapter 3, and the transport timescales.

Previous studies have quantified transport timescales in macrotidal estuaries (Banas & Hickey, 2005; de Brye et al., 2012; John et al., 2020; Lin & Liu, 2019; Yuan et al., 2007). For example, Haddout et al (2020), investigated the impact of river discharge and tidal amplitude on flushing time in Bourgreg and Loukkos estuaries using the freshwater fraction method. They found that the flushing time in the Bourgreg estuary reduced from 6.3 days to 2.7 days as the river discharge increased from 17 to 22 m^3/s, and from 3.4 days during neap tide to 2.7 days during spring tide, indicating that the influence of river discharge can overshadow that of fortnightly tidal variations even in macrotidal and convergent estuaries. However, using the freshwater fraction method does not provide any spatial information about the transport timescales nor the particle pathways in relation to the circulation in the estuary. Residual circulation in macrotidal estuaries can control the transport timescales. Mitra et al (2020) showed that in macrotidal estuaries, residence time can be increased due to the development of residual eddies that prevent particles from leaving the estuary.

A study by Alahmed et al. (2020) investigated the along-channel variations of residual flows and drivers in the Gironde estuary and found that the influence of density gradients, advection and river discharge vary along the estuary. They were unable to link the along-channel variations of residual flow structure and drivers to transport timescales in this system. The goal of Chapter

4 is to investigate how variations in density gradients, river discharge and advection alter transport timescales in macrotidal estuaries. The objectives of Chapter 4 study are to 1) Investigate the impact of density gradients, advection, and river discharge in altering the flushing time in a macrotidal and convergent estuary, 2) Determine the role of river discharge in flushing the estuary water and identify the estuary regions that are most sensitive to river inflow and density gradients, and 3) Compare the transport timescales and residual flow outcomes of a macrotidal estuary of relatively simple geometry in relation to mesotidal estuaries with complex geometries.

The studies that will be presented in Chapters 2 to 4 advance our knowledge of circulation and transport in estuaries of varying size, shape, and freshwater inflow. The findings will help to facilitate science-based decisions related to water quality assessment and management in estuaries. The overall structure of the research studies conducted in this dissertation is summarized in Figure 1. 4.

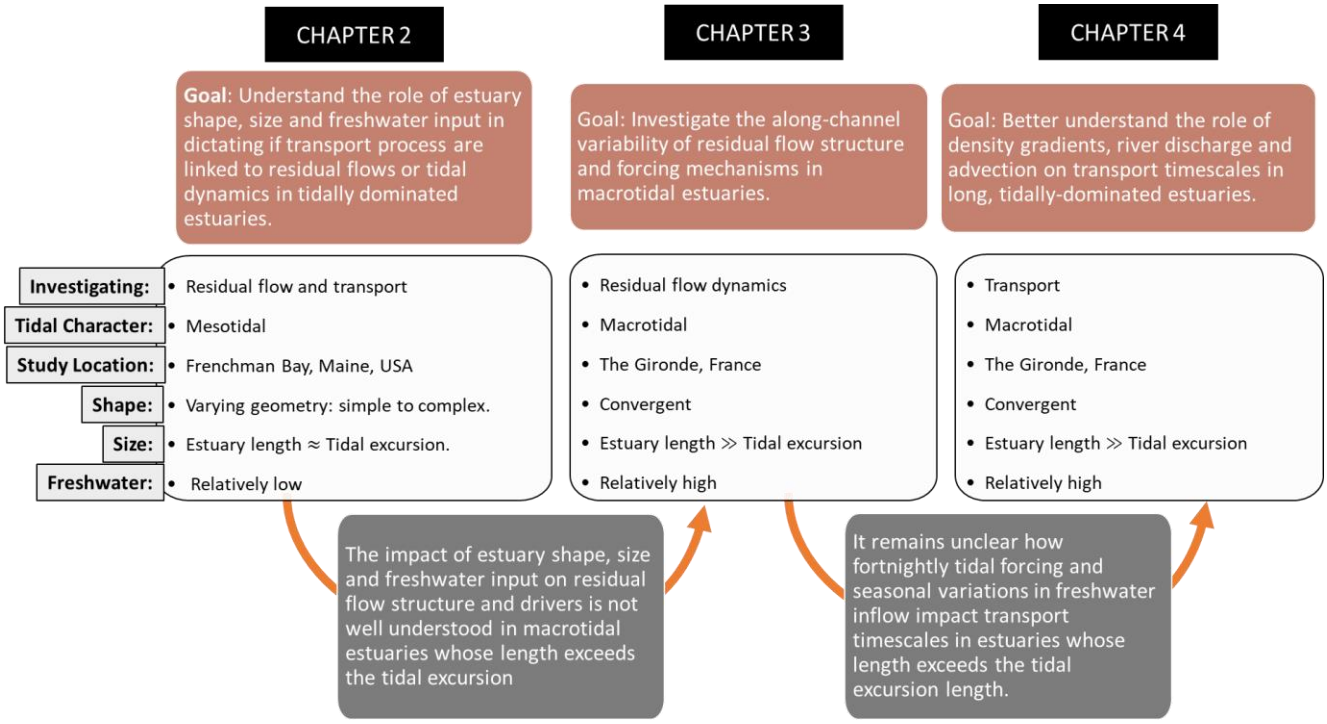

Figure 1. 4. A diagram that summarizes the structure of the research studies carried out in this dissertation.

1.6 Uncertainties

Predicting the behavior of circulation and transport in estuaries will inherently include uncertainties (Oberkampf et al., 2002). Uncertainties can arise from errors in model structure from an oversimplification of temporally or spatially small-scale processes, errors in the input data that are used as forcing, and physical misrepresentation and parametrization including simplifications in bottom profiles or geometry (Camacho et al., 2014). Uncertainties that may arise from numerical errors including time steps and turbulence closure schemes are explored in the following chapters. A description of other uncertainty sources are provided in Table 1. 1.

Table 1. 1. Sources of uncertainties that may affect the numerical outcome and prediction of estuarine circulation and transport.

Source	Type	Details
Water surface elevation at the ocean boundary	Input data error from TPXO model	The error in the free surface elevation forced at the ocean boundary of the model can reach up to $\pm$23 cm (Stammer et al., 2014).
Model Bathymetry	Input data error from NOAA	The uncertainty result from the error in the measurements and from gridding procedures (resolution). The error in bathymetry is around $\pm$2m un the horizontal positioning and $\pm$0.15 m in the vertical plane (Camacho et al., 2014).
River Discharge	Input data error from StreamStats USGS	The river discharge is forced at the model boundary based on StreamStats USGS model (Ries III et al., 2008). StreamStats gives estimates the monthly averaged stream flow for any given basin. Given the fact that the imposed river values in this work do not represent the daily variation in the river discharge and that they are estimated, uncertainties in the river discharge values are expected.
Stationary Bed Type and Bed Formation	Oversimplification	The formation of the bed (e.g. ripples and dunes) as well as the transport of bottom materials (mobile bed). The formation of the bed and bottom materials affect the bottom drag and, as such, the flow in the system. The positive feedback loop between the flow and the transport of the bed materials may lead to, if not considered, a notable error in the numerical model outcomes.
Friction Factor	Misrepresentation	The friction factor is considered as a tuning parameter to optimize the model predictive skill. The friction factor is determined based on the measured data at few locations over the estuarine domain. Therefore, the friction factor may lack the necessary spatial variation to minimize the error of the numerical prediction over the entire domain.
Wind	Oversimplification	The wind impact on the flow and the transport processes is not considered in this study.
Truncation and Precision Error	Modeling Error	These errors arise due to the discretization of the PDEs that describe the physical processes in natural systems and duo to the fact that computer machine has a limited precision. This error is detailed in section 2.5.2

1.7 Outline

This dissertation consists of five chapters. The remainder of this dissertation is organized as follows:

Chapter 2 presents the residual flow, flushing, and residence time in multiple mesotidal estuaries of varying shape and freshwater input using a three-dimensional Eulerian-Lagrangian numerical model based on Frenchman Bay system in Maine as a case study site. The model

validation and limitation are shown and discussed in this chapter highlighting uncertainties that arise due to the numerical calculations. The chapter examines how some regions in the estuaries exhibit relatively long timescales compared to other regions due to the estuary morphology and flow dynamics.

Chapter 3 presents the residual flow along a macrotidal and convergent estuary. A three-dimensional hydrodynamic model is developed based on the Gironde estuary in France as a case study site. The model validation against measurements as well as the model limitations are discussed in this chapter. The chapter shows how residual flow patterns vary along the estuary in response to the variation of the forcing mechanisms due to changes in estuarine bathymetry. The material in this chapter has been published as Alahmed et al. (2020)

Chapter 4 furthers the findings of chapter 3 by presenting the impact of residual flow drivers (density gradients, advection and river discharge) on flushing and residence times in a macrotidal and convergent estuary. A three-dimensional Eulerian-Lagrangian numerical model is developed based on the Gironde estuary in France as a case study site. This chapter shows that river discharge plays a major role in flushing the system due to the residual flow pattern in the system.

Finally, Chapter 5 concludes the main results of the three studies presented in this dissertation. The chapter puts together the results of residual flows and transport timescales found in mesotidal and macrotidal estuaries and underlines the estuaries similarities and differences informed by the conclusion made in each chapter.

CHAPTER 2

RESIDUAL FLOW AND TRANSPORT TIMESCALES IN A SYSTEM OF MULTIPLE ESTUARIES

This chapter surveys the residual flow and the transport timescales in multiple mesotidal estuaries (tidal range>2 and <4) with different geometries. A relationship between tide, estuarine shape, and the flushing of the systems is drawn to facilitate a better water quality assessment for policymakers and stakeholders.

2.1 Introduction

Human activities along coastlines in the past two centuries have increased the susceptibility of coastal and estuarine waters to water quality problems linked to elevated loadings of nutrients, sediment, bacteria, and other pollutants (Bilgili et al., 2005; Carpenter et al., 1998; Iglesias et al., 2020; Nixon, 1995). The loading of pollutants from freshwater runoff can have consequences to estuarine water quality, aquatic habitat, and the economies of coastal communities. In Maine, coastal pollution problems provide an example of how water quality impairments can result in temporary or permanent closures of coastal areas where clamming and blue mussel and oyster aquaculture activities occur (Hillyer, 2019; MDMR, n.d.; True, 2018). The closures based on fecal coliform concentration sampling have contributed to the loss of $3.6 million over a nine-year period (Evans et al., 2016) and have created complex social issues in coastal communities (McGreavy et al., 2018). Coastal pollution management strategies in Maine and other locations influenced by land-sea connections can be improved with better information about the physical processes that control the transport of pollutants and nutrients in estuaries connected to terrestrial watersheds by freshwater flows (Greening & Janicki, 2006; John et al., 2020). It has been shown that vulnerability to pollution problems at a location can depend on

pollutant concentrations entering from watershed runoff, the duration of time that pollutants spend in the estuaries (Du et al., 2020), and the rate of estuary exchange with the ocean (Ribeiro et al., 2016). This research is framed to provide a basis on how estuary hydrodynamics linked to watershed runoff and ocean exchange can be quantified to guide water quality and natural resource management policies and strategies.

Flushing and residence time are two commonly used measures of water quality in marine systems (Lin & Liu, 2019). The terms are widely known but often interchangeably used despite the fundamental difference in the processes they describe (Lucas, 2010; Monsen et al., 2002). Flushing time is the duration necessary to fully renew the initial water mass in a waterbody, describing exchange within a waterbody but without spatial details related to transport processes (Monsen et al., 2002). Estuaries with short flushing times are considered to be resilient to pollution problems as they quickly exchange water with the adjacent coastal ocean (John et al., 2020). In contrast, the residence time is the time required for a water parcel found anywhere in a waterbody to be evacuated from the system (Zimmerman, 1976), providing spatial information on transport timescales within the estuary domain. Coastal locations with short residence times are less likely to have pollution problems than systems with high residence times because of the relatively short amount of time necessary for contaminants to travel out of the estuary (Kenov et al., 2012). The residence time of an estuary can be quantified by Lagrangian particle tracking approaches implemented within an estuarine domain.

The transport of a dissolved substance (Shen & Wang, 2007) and water parcel trajectory prediction (Signell & Butman, 1992) are influenced by the residual flow in an estuary. Unlike

residence time or other transport timescales, residual flow estimates in an estuarine system can inform the decomposition of forcing mechanisms that govern particle transport. A tidally averaged flow rate that quantifies residual flow is defined as the current velocity averaged over the dominant tidal period (Zimmerman, 1979). providing a basis to estimate exchange flow magnitude and structure in estuaries, and therefore a first indication of transport capacities (Li & O'Donnell, 1997, 2005). Residual flows can be driven by changes in density (usually salinity) (Hansen & Rattray, 1965), barotropic tide (Li & O'Donnell, 2005), tide-estuarine morphology interaction (Zimmerman, 1978), wind (X. Guo & Valle-Levinson, 2008; Sanay & Valle-Levinson, 2005; Wong, 1994), river discharge (Santana et al., 2018), Earth's rotation (Valle-Levinson et al., 2003; Winant, 2008), and channel planform curvature (Chant, 2002). Here we highlight the relative contributions of freshwater input and tidal circulation patterns in altering the transport timescales in estuaries with varied geometry along the coast of Maine (USA).

Freshwater river inflows to estuaries, tidal currents, and estuarine morphometry can collectively produce varied outcomes in terms of residual flow and transport timescales over a range of conditions (Defne & Ganju, 2015). Wan et al. (2013) used three-dimensional simulations to quantify decreases in residence time and adjustment in the location of maximum residence time with increases in river discharge into the Caloosahatchee Estuary in the Gulf of Mexico. Shaha et al. (2012) observed reductions in flushing time varied with increases in river discharge into the Sumjin River Estuary on the south coast of Korea. Meyers & Luther (2008) highlighted the relevance of density gradients to residence time in Tampa Bay in Florida, USA, revealing a fourfold reduction in estuary flushing time caused by salinity changes linked to intermixing of freshwater inputs from rivers with saltwater from the ocean. The study by Shaha et al. (2012)

also documented the role of ocean inputs to estuaries, specifically fortnightly tide variability, observing flushing times close to those associated with a semidiurnal tidal period during a spring tide but twice as long during a neap tide. The added influence of coastal morphometry on hydrodynamics was highlighted by Banas & Hickey (2005) who documented relations of estuary constrictions and planform alignments to particle transport and the exchange of water masses in and between estuaries in Willapa Bay in Washington, USA. The observations from these investigations collectively describe the varied outcomes produced from varied combinations of river flow, tidal currents, and estuarine morphometric conditions in coastal areas.

The challenge ahead for most coastal locations is to use observations of these complex interactions involving the three primary drivers of estuary hydrodynamics to guide predictions and management strategies. The dynamics that govern physical estuarine conditions have been described and governing relations have been derived for individual processes, but the capacity to predict estuary hydrodynamics at specific locations and moments in time is limited in most places because multiple factors and dynamics are simultaneously influencing the outcome. The persistent information gap can be closed through strategic implementation of numeric simulations to guide the prediction of hydrodynamic outcomes from coastal scenarios defined by freshwater input from rivers, ocean exchange and tides, and estuary morphometry. The design, implementation, and interpretation of scenario simulations involving the three primary drivers of estuary hydrodynamics influencing pollutant transport and residence time serve as the focus of our research.

The analyses we summarize are designed to demonstrate the implementation and interpretation of estuary hydrodynamic scenario simulations to advance pollution prediction capacity and related management decision support. A Lagrangian particle-tracking approach is used with a validated numerical model to simulate the estuarine hydrodynamics and quantify transport timescales. Three primary objectives frame the research that examines varied combinations of freshwater river input and tidal dynamics in three coastal Maine locations that are similar in terms of watershed rainfall-runoff response and tidal regime but varied in terms of morphometry defined by estuary shape and bathymetry. The objectives are to:

1) Identify and generalize relations between estuary tidal dynamics, density gradient, freshwater inflows, and particle transport timescales through hydrodynamic scenario simulations,
2) Characterize estuary conditions where and when particle transport timescales are relatively more sensitive to freshwater river inflow rates, and
3) Interpret research hydrodynamic outcomes in relation to coastal geomorphological conditions to provide better guidance for coastal resource managers to scale up observations and implement strategies for monitoring and response to pollution problems in varied coastal settings.

The objectives are framed to guide coastal stakeholders to identify the primary drivers of hydrodynamic flushing patterns in estuaries and predict the location of estuaries with elevated timescales for flushing based on the coastal geomorphic conditions and tidal dynamics.

The remainder of this chapter includes detailed information regarding the case study site around Frenchman Bay and Blue Hill Bay in Section 2.2. Details on data collection, numerical model setup and validation, and on the Lagrangian particle tracking approach used to quantify the transport timescales and particle pathways is described in Section 2.3. In Section 2.4 the flushing and residence time results are presented and compared to estuarine residual flow in the three estuaries considered. Section 2.5 discusses the role of the shape of the estuaries in governing the transport and the study findings are generalized. Model uncertainties and limitations are also discussed. Finally, the concluding remarks are provided in Section 2.6.

2.2 Study Site: Frenchman Bay and Blue Hill Bay Systems in Maine, USA

Located on the mid-coast of Maine (Figure 2. 1a), Frenchman Bay, Blue Hill Bay and their adjacent estuaries house an abundance of oyster and mussel farms and provide vast intertidal areas for harvesting clams (see Disney, 2015; "Frenchman Bay," n.d.). The tidal height in this area ranges from 2 m during neap tide to 4.5 m during spring tide. Thus, the systems can be classified as mesotidal and macrotidal (Davies, 1964). Frenchman and Blue Hill Bays are separated by Mount Desert Island and are connected upstream through a small opening (~30 m wide) near Thompson Island (Figure 2. 1b). Each bay is hydraulically connected with multiple estuaries and smaller bays: Flanders, Sullivan, Skillings and Jordan River estuaries are connected to Frenchman Bay and Union and Morgan estuaries and Western Bay are connected to Blue Hill Bay. Among these estuaries, three systems (Union River Estuary, Jordan River Estuary and Sullivan Estuary) are the focus of this study given their morphological differences and differences in watershed size.

The Union River Estuary is 10.3 km long, has an average width of 2.8 km, an average depth of 16 m and is the largest of the three estuaries considered. The cross-section shape of the Union River Estuary is parabolic-like with no abrupt change in depth in the transverse direction and no presence of multiple channels. There is little longitudinal variation in morphology (no headlands, constrictions or islands). The major source of freshwater to the system is the Union River with a mean annual discharge of 28 $m^3 s^{-1}$ (Table 2. 1) based on USGS streamflow application StreamStats (www.usgs.gov/ss/). The Jordan River Estuary is narrow and shallow compared to the Union River Estuary. It is 5.4 km long, has an average width of 0.7 km, and has an average depth of 2.0 m. The lateral and longitudinal bed profiles in the Jordan River Estuary are complex with abrupt changes in depth in the lateral direction and the presence of multiple bends. The estuary receives freshwater from three streams: Jordan River, Foster Brook and Crippens Brook with a combined mean annual discharge of 0.35 $m^3 s^{-1}$ (Table 2. 1). The Jordan River Estuary features extensive tidal flats at its shoals and at its head where the upstream ~1.5 km reach is exposed during low tide. The Sullivan Estuary, which includes Taunton Bay upstream, features multiple islands, headlands, and constrictions along channel. The system features 'reversing falls' at the mid-reaches due a 170 m wide constriction. The estuary is 18 km long, has an average width of 1 km and has an average depth of 6 m. Three streams contribute to the freshwater in

Sullivan: Card Mill Stream, Mill Brook and Egypt Stream with combined mean annual discharge of 3.41 $m^3 s^{-1}$ (Table 2. 1).

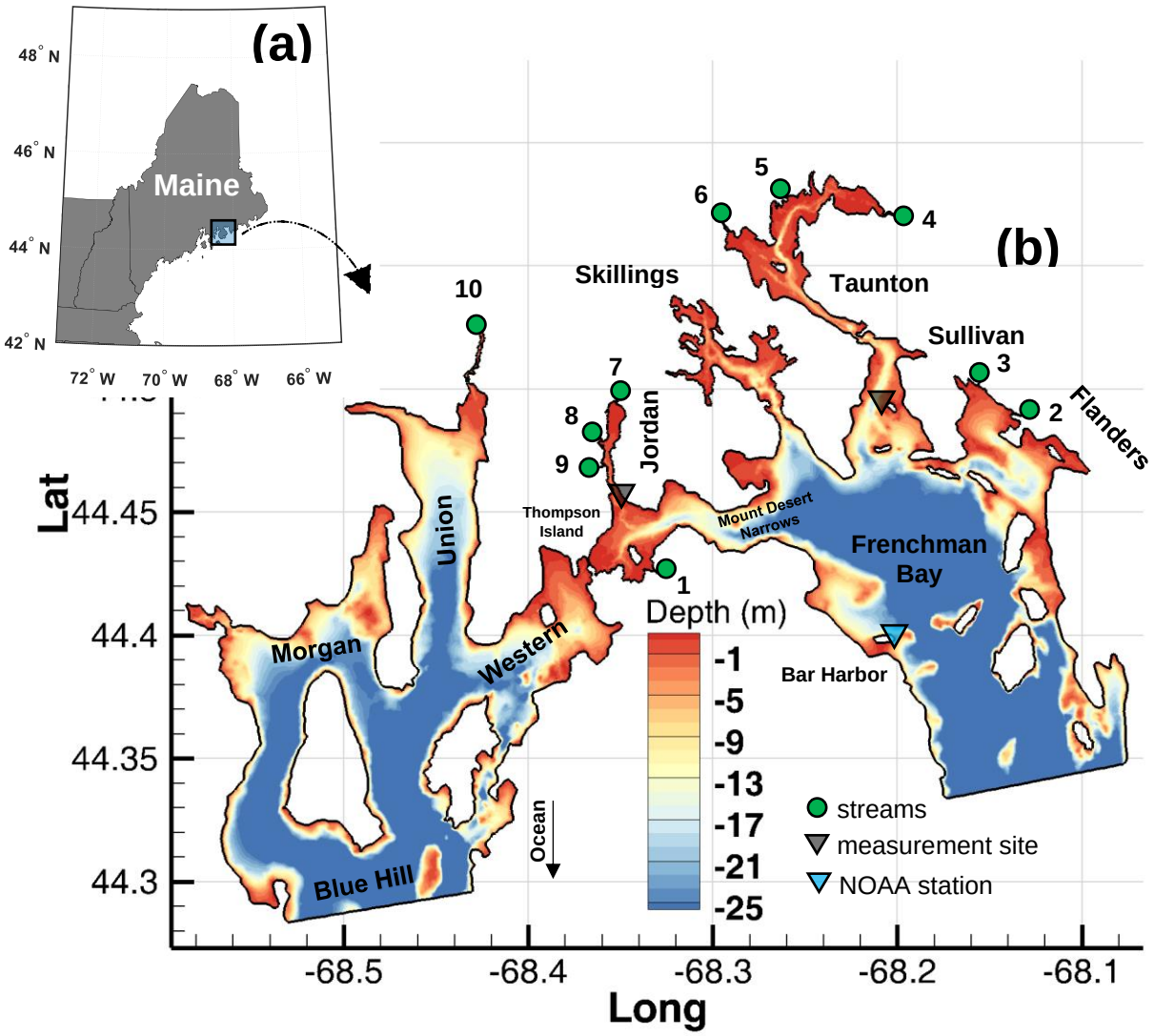

Figure 2. 1. (a) Map of Maine highlighting the location of Frenchman-Blue Hill bays, (b) The study site detailing Frenchman-Blue Hill bay systems and the adjacent estuaries as well as bathymetry (color shade). The green circles signify the streams considered in the study labeled from 1-10. The black triangle shows the location where measurements of velocity, water depth and salinity were taken.

2.3 Methodology

2.3.1 Numerical Model

A three-dimensional numerical model was used to investigate the hydrodynamic processes responsible for material transport in the Frenchman-Blue Hill Bay region. The modeling platform was Telemac3D, which is an integrated finite element tool for free surface flow simulation (Hervouet, 2007; Moulinec et al., 2011). The model domain extends from (44.24° N, 68.52° W) to (44.24° N, 68.52° W) (Figure 2. 1b). The model is forced by tides at the two ocean boundaries derived from the TPXO database (Egbert & Erofeeva, 2002). Freshwater input is included from 10 rivers (green circles in Figure 2. 1b) at the upstream boundaries (Table 2. 1). A constant salinity value (35 psu) was applied at the ocean boundaries. Bathymetry for the system, including the intertidal areas, was obtained from NOAA (maps.ngdc.noaa.gov) at 30 m resolution. Temperature, wind and ambient ocean currents are not included.

The model domain is discretized by an unstructured mesh with horizontal resolution ranging from 250 m near the ocean boundary to 1.0 m near the upstream boundaries. There are 15 terrine-following layers in the vertical plane. The vertical eddy viscosity and diffusivity are given by Tsanis mixing-length turbulence closure (Tsanis, 1989) coupled with the Munk and Anderson damping function (Uittenbogaard, 1994) to represent the stratified flow. The horizontal eddy viscosity and diffusivity are evaluated by the Smagorinsky turbulence model.

The explicit MURD (Multidimensional Upwind Residual Distribution) tidal flat scheme and the Characteristics scheme are utilized for the advection of salinity and velocity, respectively (Hervouet, 2007).

Table 2. 1. The rivers considered in the study with their minimum, maximum and mean annual discharge.

river no:	river name	min flow m^3s^{-1}	max flow m^3s^{-1}	mean annual flow m^3s^{-1}	system
1	Northeast Creek	0.0818	2.16623	0.70	Frenchman Bay
2	Morancy Stream	0.047	1.08	0.4	Flanders
3	Flanders Stream	0.116	1.212	0.70	
4	Card Mill Stream	0.3	3.25	1.91	Sullivan
5	Mill Brook	0.105	1.798	0.75	
6	Egypt Stream	0.1	2.05	0.75	
7	Jordan River	0.005	0.212	0.07	Jordan
8	Foster Brook	0.013	0.42	0.14	
9	Crippens Brook	0.7012	0.424	0.14	
10	Union River	7.05	75.32	27.7	Union

Quadratic friction is used to represent the shear stress at the bed. The friction coefficient Cd is evaluated at each time step based on Nikuradse's Law (Nikuradse, 1950; Tassi & Villaret, 2014) by the following formula,

$$Cd = 2\left[\frac{k}{\log\left(\frac{12h}{k_s}\right)}\right]^2 \qquad 2.1$$

in which, $k = 0.4$ is the von Karman constant, h is the water depth varying with time, and $k_s = 0.001$ is the bed roughness height, which is used as a tuning parameter for model calibration.

The model runs with a time step of 10 s with output saved hourly after the completion of one year of model spin-up to ensure the salinity field is fully developed.

2.3.2 Data Collection and Model Validation

The model predictive skill is assessed based on the method of Willmott (1981) which provides a quantitative measure for the agreement between the numerical outcomes and observations as follows,

$$Skill = 1 - \frac{\sum |X_{model} - X_{observed}|^2}{\sum (|X_{model} - \overline{X_{observed}}| + |X_{observed} - \overline{X_{observed}}|)^2} \qquad 2.2$$

where X_{model} and $X_{observed}$ denote the numerical and the measured value of any quantity, respectively. The over bar denotes a time average. If the model outputs are in perfect agreement with the observations, Eq. 2. 2 yields a skill value of one. The model skill is evaluated for the water level data obtained from a NOAA tide gage station near Bar Harbor (https://tidesandcurrents.noaa.gov/) and for the measured water depth, salinity, and velocity in the Jordan River Estuary as well as the water depth in the Sullivan Estuary (see Figure 2. 1b). The water depth in the Jordan River Estuary was measured using a Solinst Levelogger pressure sensor at 10-minute intervals deployed in the thalweg near the estuary mouth from Aug 16th to Sep 14th, 2018. The pressure sensor was calibrated based on a barometric pressure logger that was installed nearby on land. Horizontal current velocities were collected for a full tidal cycle (12.5 hours) over a cross-channel transect (~450 m wide) near the mouth of the Jordan River Estuary on Sep 13, 2018 using a 1200 kHz RDI Workhorse Acoustic Doppler Current Profiler (ADCP). Measurements were collected in 0.25 m vertical bins at 2 pings per ensemble. A Garmin GPS was

integrated into the ADCP software to track the measurement locations during data collection. A total of 29 transects were completed over the tidal cycle. Measurements within 10% of the bottom were excluded due to side lobe effects, data ensembles with a signal return of 85% or less were excluded, and error velocities greater than 5% of the maximal flow were omitted. The remaining data were then corrected using a comparison of bottom track velocities measured by the ADCP to instrument velocities derived by the GPS data following the method of Joyce (1989) and were interpolated onto a regular grid.

During the tidal cycle survey, salinity and temperature were also measured at the center of the ADCP transect (in the navigation channel) using a Sontek Castaway Conductivity, Temperature, and Depth (CTD) profiler which sampled at 5 Hz with ± 0.1 psu and ± 0.05^{o} C accuracy for salinity and temperature respectively.

The water level data at Bar Harbor and water depth in the Jordan River Estuary as well as the current velocity and salinity data were compared with model output. The skill values reported in Figure 2. 2a suggest that the model agrees well (skill>0.99) with the observed water level near Bar Harbor and with water depth Figure 2. 2b and velocity Figure 2. 2d in the Jordan River Estuary. The model shows less predictive skill for salinity (Figure 2. 2c, skill=0.65). This is likely because the streamflow values applied in the model are estimated monthly averages. Accurate measurements for the freshwater input and long term data for salinity are recommended to better assess the model, but for the objective of this study the predictive skill is considered satisfactory. Although, the model was calibrated/validated based on 2018 data, the model outcome was also compared with the measured water depth in the Sullivan Estuary (Figure 2. 1)

from Jun 16th to Aug 24th of 2020 as an extra test for the model validity. The model reports a skill of 0.994 (Figure 2. 2e) indicating a good agreement with the measured data.

2.3.3 Residual Flow and Streamlines

The along-channel residual flow is evaluated using a least square analysis (Foreman & Henry, 1989), which is commonly used to decompose the flow signal into the oscillating component from the tide and a residual component (R. Cheng & Gartner, 1985). The residual flow and the tidal amplitude are evaluated considering 24 h of data (two semidiurnal tidal cycles) and the semidiurnal (M2, 12.42 h), quarter-diurnal (M4, 6.21 h), and sixth-diurnal (M6, 4.14 h) tidal species are extracted. Residual streamlines are determined by the residual flow field. A residual streamline is defined as a curve that is tangent to the residual velocity vector (see Zimmerman, 1981). The length of the residual streamline at a specific location along the estuary is quantified based on the major diameter of the largest residual eddy at that location. In case of multiple eddies, the average of the major axis of the largest eddies is considered as residual streamline length. It is worth mentioning that "residual eddy" in this article refers to eddies in the horizontal plane. In the absence of eddies, the length of the streamline is simply quantified using the Arc Length method as follows

$$S = \int_{p1}^{p_{end}} \sqrt{(dx^2 + dy^2)}\, ds \qquad 2.3$$

where S is the length of the streamline, dx and dy are the spatial distance in the x and y coordinates between two points along the streamline, and the integration is performed over the points that are connected by that streamline ($p1\ to\ p_{end}$).

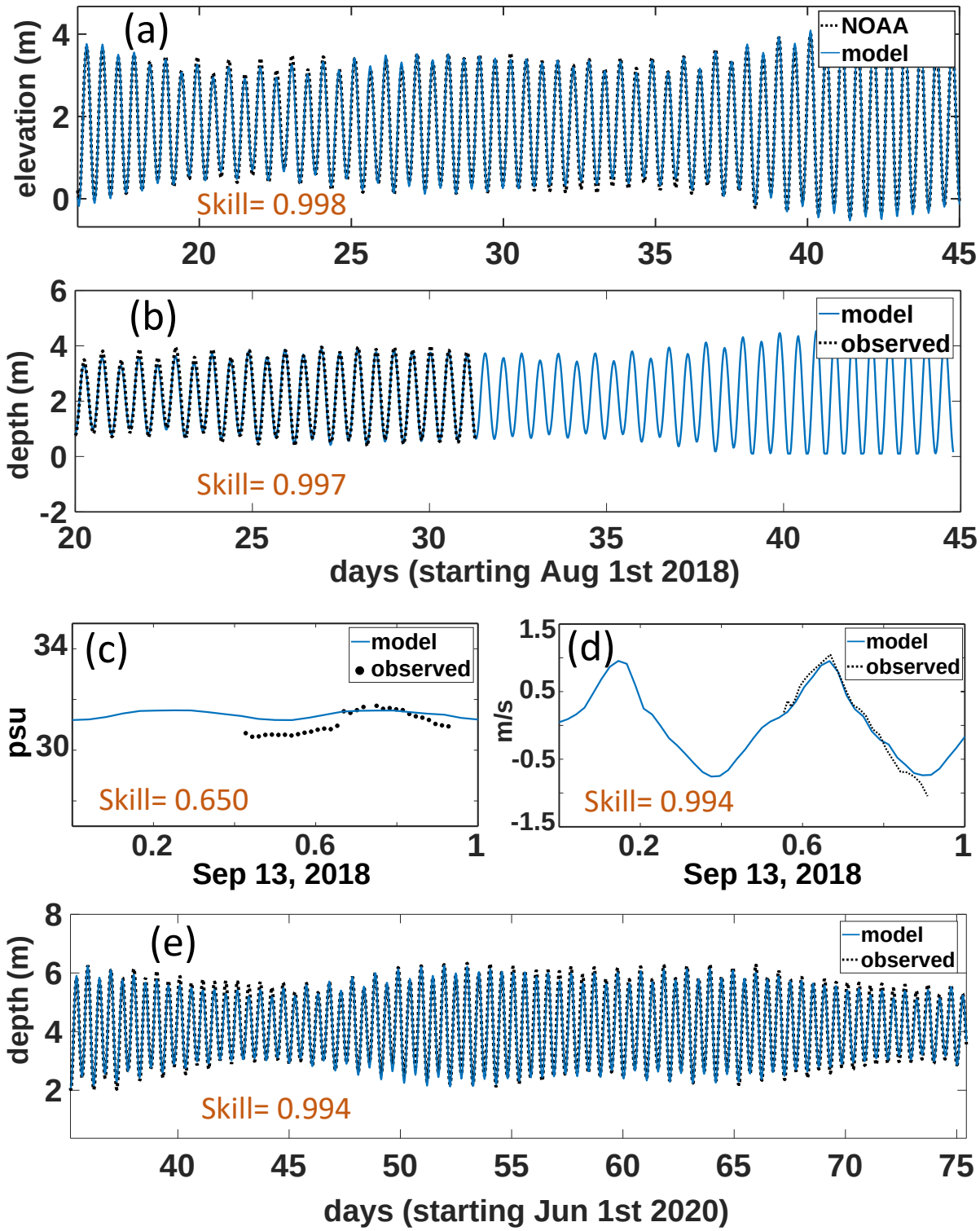

Figure 2. 2. Comparison of observed and modeled time series of free surface elevation at (a) Bar harbor NOAA station, (b) water depth in Jordan River, (c) salinity in Jordan River, (d) velocity at the channel of Jordan River mouth, and (e) water depth in Sullivan estuary. The predictive skills of the model are reported on the left corner of each subplot.

If the streamline extends from the river to the mouth of the estuary, then the length of the streamline will be the distance from the river to the mouth.

2.3.4 Lagrangian Particle Tracking as a Proxy for Pollution Transport

Lagrangian particle tracking is used as a proxy for constituent (pollution) transport and to determine transport pathways and connectivity between adjacent bays and estuarine systems (Van Sebille et al., 2018). One of the challenges in defining transport timescales is determining the delineations of estuaries and bays within which the timescales are quantified, as values such as residence times are sensitives to the boundaries of the water body being considered. To ensure that the transport timescales quantified in this study were relevant to decision makers and how they manage coastal pollution issues, the Maine Department of Marine Resources (MDMR) representatives were consulted during the Coastal Bacteria Pollution Research and Management Coordination Meeting on February 6th, 2019 to define estuary boundaries. MDMR drew estuary delineation lines along the entire coast of Maine, with the Frenchman-Blue Hill Bay systems included. The result of this exercise arrived at 11 sub-regions around the bays as illustrated in Figure 2. 3a. At each sub-region, Lagrangian particles were released in three layers: near the surface, mid water column, and near the bottom (Figure 2. 3b). In each vertical layer, the particles were initially spaced 100 m apart. Approximately 100,000 particles were placed in the domain. A unique identity number (tag) was assigned to each particle so it could be tracked during the simulation until it leaves the domain through an ocean boundary, where the particles are not allowed to re-enter. The particles are passive (do not affect the dynamics of the flow), conservative (do not die or reproduce), and are neutrally buoyant (can move in three dimensions based on the current direction).

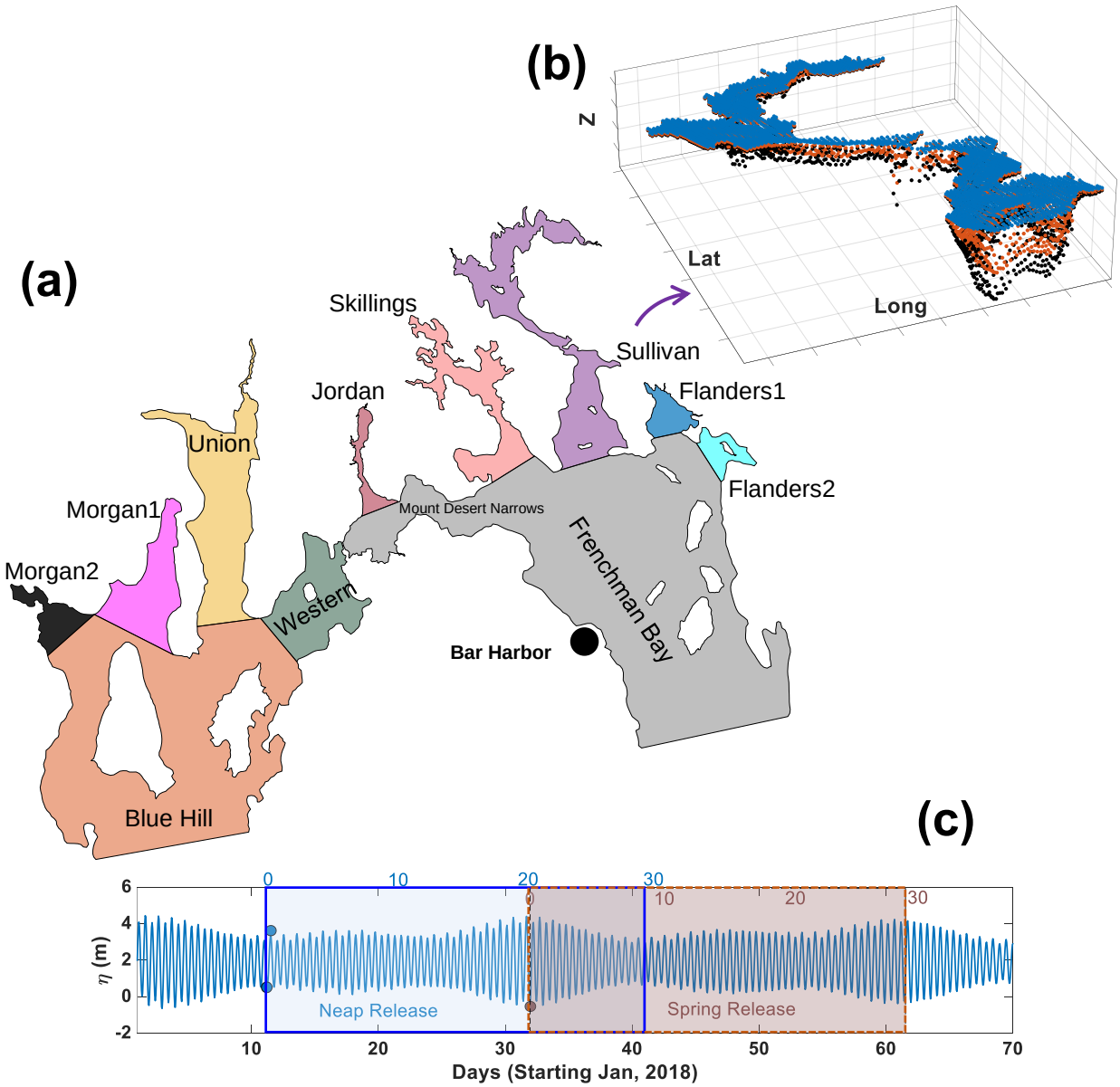

Figure 2. 3. (a) Estuary delineations subdivided based on color for quantification of residence and flushing times. (b) Example of the vertical placement of particles in the model domain at the surface, mid water column and near bottom, and (c) the water level in Frenchman Bay detailing the particle release times (circles) and simulation period (blue box color for neap release and rosy-brown box color for spring release) for all of the simulations detailed in Table 2.2.

The particle trajectories were recorded at 2 h intervals and were used to evaluate the residence and flushing time in each sub-region as well as the connectivity between sub-regions.

Four simulations (i.e., cases) were completed to evaluate scenarios related to river inflow, tidal range, and water density influence on estuary particle movement (Table 2. 2):

I. River inflow varying from constant minimum versus maximum river discharge rates (R1 vs R2);
II. Fortnightly variation in tide associated with neap versus spring tide conditions (R1 vs R3);
III. Different water density gradients associated with high to zero salt concentration (R1 vs R4).

In each case, the particles were released during low tide and tracked for 30 days as shown in Figure 2. 3c. Low tide was chosen as a 'worst case' scenario since the particles would not immediately leave the estuary. Three additional cases were performed to explore sensitivity of the results to turbulence closure and numerical time step as will be discussed in section 2.5.2.

Table 2. 2. The set of the numerical experiments performed. The primary simulations (R1-R4) are used to study residence and flushing time considering high-low river discharge, neap-spring cycle and baroclinic-barotropic conditions. The complementary simulations (C1-C3) are used primarily for a sensitivity analysis.

	Primary Simulations				Complementary Simulations		
	R1	R2	R3	R4	C1	C2	C3
River	low	high	low	high	high	low	low
Tidal Condition	neap	neap	spring	neap	neap	neap	neap
Density Gradient	on	on	on	off	on	on	on
Time Step	10 s	10 s	10 s	10 s	10 s	5 s	1 s
Vertical Closure	mixing length	mixing length	mixing length	mixing length	$k\varepsilon$	mixing length	mixing length
Water Level	low tide	low tide	low tide	low tide	low tide	low tide	low tide

2.3.5 Residence Time, Flushing Time and Connectivity

The residence time was quantified throughout the model domain by determining the time particles spend in each estuary before they exit the estuary the first time. The depth-averaged residence time at any location in the estuary is evaluated by averaging the residence time of the particles released at the same horizontal location at different depths (surface, mid and bottom particles). The estuary-wide residence time was estimated as the average of the residence times of all the particles inside the delineated estuary domain.

Flushing time provides no spatial details on transport time scale in water systems, rather, it measures the transport time for a waterbody as one integrative system. The concentration of

particles (C) released in a specific sub-region (*i=1 to 11*) decays based on the following remnant function (Bilgili et al., 2005; Braunschweig et al., 2008; Signell & Butman, 1992),

$$C_i(t) = \frac{N_i(t)}{N_{i_0}} \qquad 2.4$$

where $N_{i_0}$is the initial number of particles released in the region i and N_i is the number of the particles initially released in region i and remains in region i after time t. C_i, therefore, varies between 1 (at $t = 0$) and 0 when the system is completely flushed.

Assuming that particles are fully mixed and distributed evenly over the domain after one tidal cycle to represent a continuously stirred tank reactor, and $C_i(t)$ will exponentially decrease with time (Wan et al., 2013; Zhu et al., 2015) as,

$$C_i(t) = C(0)\, e^{-t/T_f} \qquad 2.5$$

where T_f denotes flushing time and $C(0) = 1$ based on Eq. 2.4. The exponential behaver of $C_i(t)$ in Eq. 2.5 suggests that the water system is considered to be flushed ($t = T_f$) when $C_i(t) = 0.37$ (37% of the initial particles remain in the system). $C_i(t)$ is directly calculated from the numerical simulations and flushing time for each sub-region is defined when $C_i(t) = 0.37$.

For regions that are hydraulically connected, a particle released in region i can be found in region j after a certain amount of time (Kämpf et al., 2010; Thompson et al., 2002). Regions i & j are connected if 37% or more of the particles initially released in region i are transported to region j within the flushing time window of region i. The concentration of the particles from region i found in region j can be expressed as,

$$C_{ij}(t) = \frac{N_{ij}(t)}{N_{i_0}} \qquad 2.6$$

in which $N_{ij}(t)$ is the fraction and the number of the particles initially released region i and found at j after time t.

2.4 Results

The flushing time and connectivity of the Union River, Jordan River, and Sullivan estuaries are presented to provide a general idea about how long it will take pollutants to be evacuated on a system-wide scale and if pollutants can be transported between estuaries. The residence time is then investigated to extrapolate the findings of the flushing time onto a finer spatial scale within each estuary. Finally, the Eulerian residual flows are presented and are compared with the transport timescales in each considered estuary.

2.4.1 Flushing Time and Connectivity

The Jordan River Estuary has a shorter flushing time (~1-2 days) than the Union River Estuary or Sullivan estuary (~3-5 days for both systems; Figure 2. 4) when density variations are included in the system. When density variations are excluded and only tidal forcing is considered, the flushing time in the Union River Estuary and the Sullivan Estuary increase by over 40 days and 5 days, respectively, while the flushing time in the Jordan River Estuary remains similar. Therefore, the response of the flushing time to river discharge, density variations, and the spring/neap tidal range varies substantially in each estuary.

The Union River Estuary shows a minimum flushing time (FT) of 3.4 days during neap tide and high river discharge (Figure 2. 4a, R2). For low river discharge, and during neap (R1) and

spring releases (R3), the FT is nearly the same (~5.8 days; Figure 2. 4a). However, when the density gradient is suppressed (Figure 2. 4a, R4), the FT is higher (48.7 days) compared to each baroclinic run (R1-R3). The Union River Estuary is connected with Blue Hill Bay (Figure 2. 1b).The fraction of particles from the Union River Estuary that are later found in Blue Hill Bay increases to approximately 0.4 (40%) (on average for R1-R3; Figure 2. 4a) after ~6 days and then subsequently decreases as the particles are flushed to other systems further downstream.

In the barotropic run, the number of particles from the Union River Estuary going into Blue Hill Bay monotonically increases throughout the simulation period (30 days; Figure 2. 4a, R4).

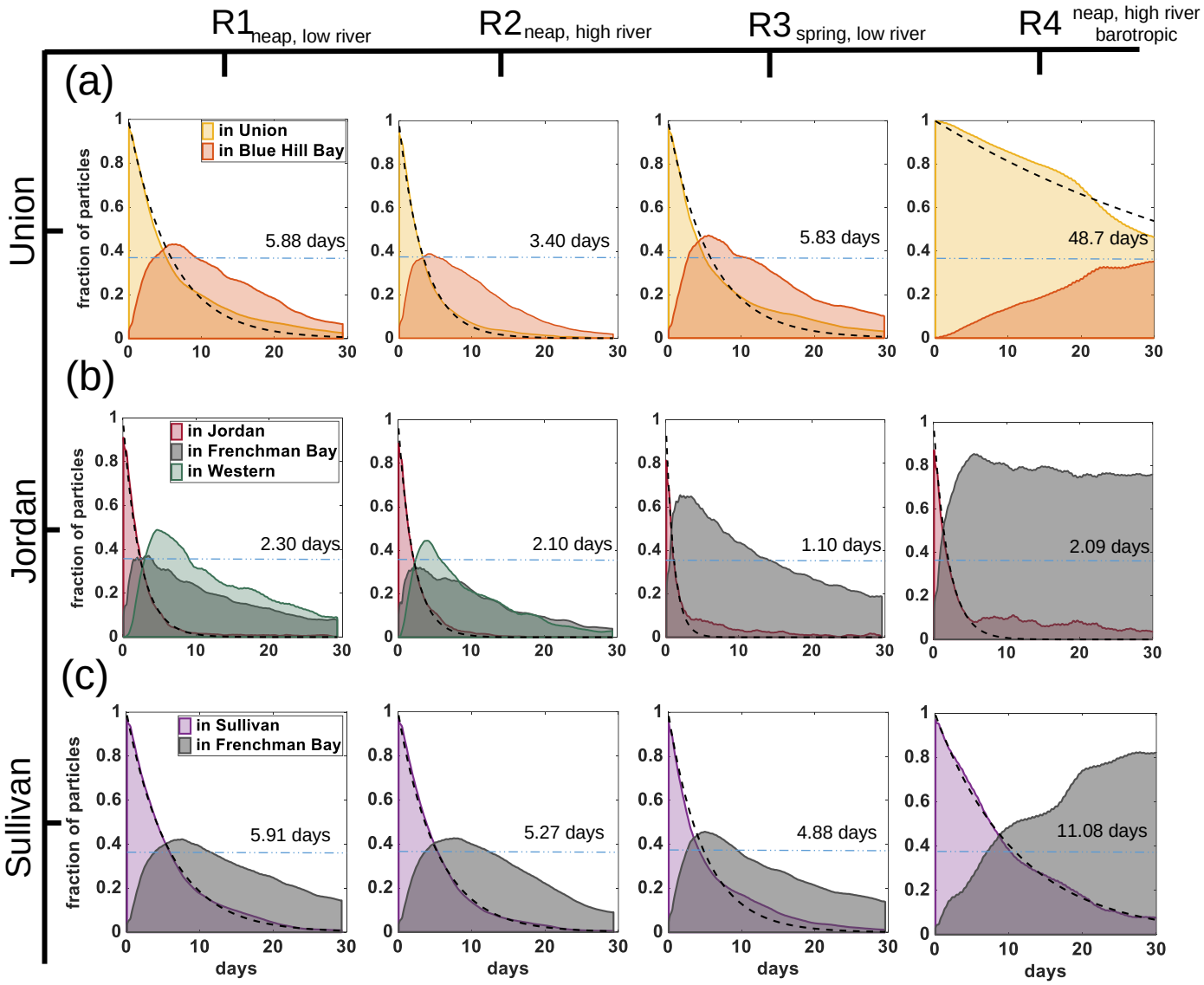

Figure 2. 4. Flushing time and connectivity for (a) Union, first row, (b) Jordan, second row, and (c) Sullivan, third row. Each column refers to a specific simulation case (R1-R4) from left to right detailed in Table 3. The flushing time value is reported in days for each case and for each system when 37% (0.37, the blue dashed line) of the particles remain in the system of release. The curves are color-coded based on the system where particles are found.

The Jordan River Estuary shows a minimum FT (1.1 days) during the spring tide release (Figure 2. 4b, R3) indicating that the dynamics of the estuary is dominated by the semidiurnal tide. The change in river discharge (R1 and R2) and baroclinicity (R4) show trivial impact on FT (all ~2.0 days; Figure 2. 4b, R1, R2 and R4). The estuary is connected with both Frenchman and Western Bays during the neap tide releases (Figure 2. 4b, R1 and R2), where particles from the Jordan River Estuary begin to appear in both bays in less than one tidal cycle (<12.42 h). The number of particles from the Jordan River Estuary increase in both Frenchman and Western Bays initially, reaching maximums of ~37% and ~50% after 4 days in Frenchman Bay and after 6 days in Western Bay, respectively (Figure 5b; R1 and R2). Interestingly, the Jordan River Estuary is only connected with Frenchman Bay during the spring releases (R3) and for the barotropic case (R4). During spring, ~65% of the particles released in the Jordan River Estuary evacuate to Frenchman Bay after 5 days (Figure 2. 4b, R3). In the barotropic run, 85% of the particles from the estuary are transported to Frenchman Bay after 7 days (Figure 2. 4b, R4). The particles linger in Frenchman Bay (Figure 2. 4b, R4) and Blue Hill Bay (Figure 2. 4a, R4) throughout the simulation time (30 days) in the barotropic case, which suggests that the circulation in these systems is altered when suppressing the density gradient.

The minimum flushing time in the Sullivan Estuary (4.8 days) is observed during the spring tide release (Figure 2. 4c, R3) and is ~1 day less than the highest FT of the baroclinic cases, which during neap tide and low river discharge (5.91 days, Figure 2. 4c, R1). An increase in the river discharge decreases the flushing time from 5.91 days to 5.27 days (Figure 2. 4c, R2). In the barotropic case, FT in Sullivan increases to 11 days (Figure 2. 4c, R4). The Sullivan estuary is connected with Frenchman Bay only. On average, 40% of Sullivan particles appear in Frenchman

Bay after 7 days. In the barotropic case (R4), however, particles that exit the system spend more time in Frenchman Bay compared to the baroclinic cases (R1-R3). This suggests that the circulation in Frenchman Bay is influenced by density as was also found from the Jordan River results.

2.4.2 Residence Time

The Jordan River Estuary has the shortest spatially averaged residence time for all cases (<2 days) compared to Union River (5-23 days) and Sullivan (4-6 days) estuaries. When the density gradient was not included, during neap and high river discharge (R4), the spatially averaged residence times in the Union River Estuary was considerably increased (23.6 days; Figure 2. 5a, R4) compared to the similar run with density gradient included (R2; 5.19 days), indicating that density-driven residual flows are likely influential in this system. When density gradients are included, increasing river discharge reduces the spatially averaged residence time from ~9 days to ~5 days (Figure 2. 5a, R1 and R2) suggesting the importance of river flow in this estuary. When river discharge is low and comparing neap tide to spring tide release, the spatially averaged residence time reduces from 9 days to ~7 days (Figure 2. 5a, R1 and R3).

Comparing the spatial variability of the residence time within each estuary, the most profound difference is found in the Union River Estuary between the baroclinic cases (R1-R3 cases) and the barotropic case (R4). For the baroclinic cases (R1-R3), the residence time over the western side of the estuary is longer than it over the eastern side (Figure 2. 5a, R1-R3) due to the large influence of fresh water from the Union River in the upper estuary. For the barotropic case

(Figure 2. 5a, R4), the residence time more than two times larger than the barotropic cases at most spatial locations in the domain.

Unlike the Union River Estuary, the absence of density gradients in the Jordan River Estuary do not impact the spatially averaged residence times value (Figure 2. 5a, b). In all cases, the minimum residence time values (<1 day) in Jordan River Estuary are found near the mouth of the system while the maximum residence times (around 2.5 days) are observed upstream. The shortest spatially averaged residence time (4.7 days) in the Sullivan Estuary is during the spring tide release (Figure 2. 5c, R3) while the highest value (6.6 days) is observed when the density gradient is suppressed (Figure 2. 5c, R4), indicating that density-driven residual flows could be influential in this system. However, when density gradients are included and the river discharge is increased (R1 and R2), the spatially averaged residence time is only reduced by only 0.6 days (Figure 2. 5c). In all scenarios in Sullivan estuary (Figure 2. 5c), the residence time is higher (>6 days) in the upper estuary than the lower estuary (<2 days) since particles in the upstream have to travel a longer distance to leave the system than those in the downstream.

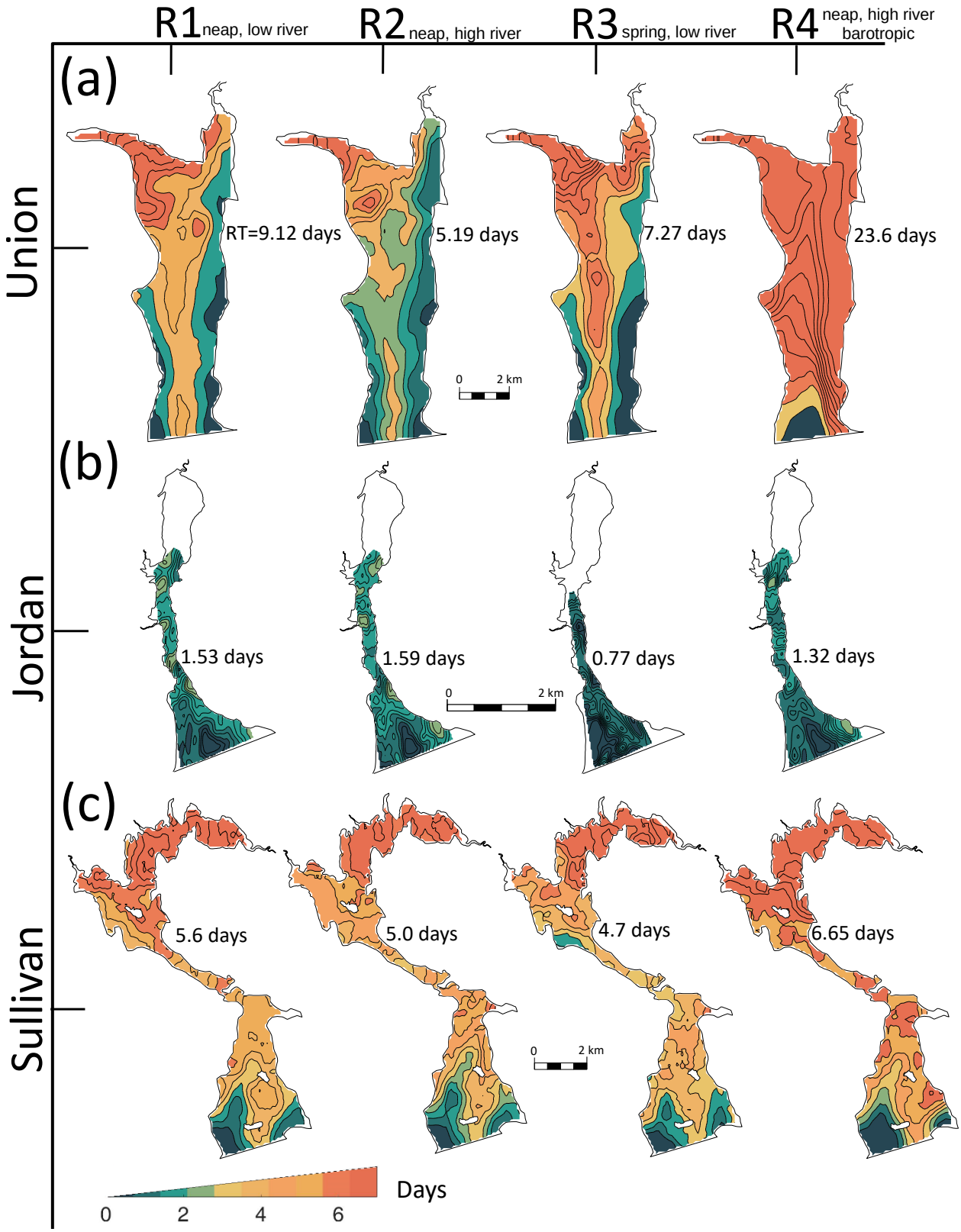

Figure 2. 5. Residence time map for (a) Union, first row form top, (b) Jordan, second row, and (c) Sullivan, third row from top. Each column refers to a specific simulation case (R1-R4) from left to right. The area averaged residence time is reported in days on the right side of each case for each system.

2.4.3 Residual Flow

In the Union River Estuary, the structure and magnitude of the residual flows are driven by river discharge and density gradients. Transects investigated near the estuary mouth show a vertically sheared along channel residual flow structure (outflow at the surface and inflow at depth) when density gradients are included (Figure 2. *6*a, R1-R3), which persist along the entire length of the estuary. The residual flows are larger during neap and high river discharge (R2 run) than during spring and low river discharge (R3 run) due to variations in the tidally averaged salinity gradient, which varied from 0.12 psu/km during neap and high river discharge to 0.049 psu/km during spring and low river discharge. Suppressing the density gradient in the Union River Estuary resulted in a significant reduction in the magnitude (16 times less than R2) and considerable alteration in the structure (laterally sheared instead of vertically sheared) of the along-channel residual flow (Figure 2. *6*a, R4). This suggests that density gradients are a main driver of residual flows in the Union River Estuary despite the large tidal range, which could lead to the higher flushing (Figure 2. 4a, R4) and residence times (Figure 2. 5a, R4) in Union River Estuary compared to the other systems.

In Jordan River Estuary, the along-channel, depth and tidally averaged salinity gradient is, approximately 0.06 psu/km during low river discharge and 0.32 psu/km during high river discharge. Despite the elevated salinity gradient during high river discharge in the Jordan River Estuary compared to that found in the Union River Estuary (0.12 psu/km), the density gradient has less of an impact on the magnitude of the residual flows. This suggests that the barotropic tide is more critical to the residual flow creation than the density gradient in the Jordan River. This is apparent on residual flow (magnitude and structure) when looking at a cross-channel

transect near the estuary mouth. The residual flow structure is laterally and vertically sheared during the neap tide release for both low and high river discharge conditions (Figure 2. *6*b, R1 and R2) with approximately same magnitude (0.01 m/s, absolute, area averaged). For the barotropic case (Figure 2. *6*b, R4), the residual flow shows the same magnitude (0.01 m/s) with laterally sheared structure (outflow in the channel and inflow over the shoals). The structure of residual flow is also latterly sheared during spring tide (Figure 2. *6*b, R3) with outflow in the channel and inflow over the shoals. The residual flow magnitude is amplified (0.02 m/s) during spring tide (R3) corresponding to the amplification in the tidal signal compared to neap tide. Also, during spring tide the minimum flushing (Figure 2. 4b, R3) and residence times (Figure 2. 5b, R3) are observed in the system. In the Sullivan Estuary the tide and density gradients both influence the residual flow magnitude and structure. For the neap tide release and low (R1) and high (R2) river discharge, the along-channel residual flow is vertically sheared (Figure 2. *6*c). During the spring tide release (R3) and for the barotropic run (R4) the along-channel residual flow structure becomes laterally and is ~50% larger than the neap tide cases (Figure 2. *6*c). The salinity gradient (tidally, along-channel, and depth averaged) over the channel was ~0.1 psu/km and 0.12 psu/km during neap tide and for low (R1) and high river discharge (R2), respectively. During spring tide and low river discharge (R3) the salinity gradient decreased to 0.016 psu/km. When salinity gradient was suppressed, a laterally sheared flow developed (R4), indicating that although the density gradient varies significantly in this estuary from low to high river discharge, the effects of the tide overpower the residual circulation and likely the flushing and residence times as well.

These results indicate that there is a correlation between the strength of the residual flows and the residence and flushing times in the three considered estuaries, where the residence and

flushing times are higher in estuaries with higher magnitude residual flows. The role of estuary shape, including length, width and along-channel features such as bends, constrictions and headlands in shaping this correlation will be elaborated upon in the discussion section.

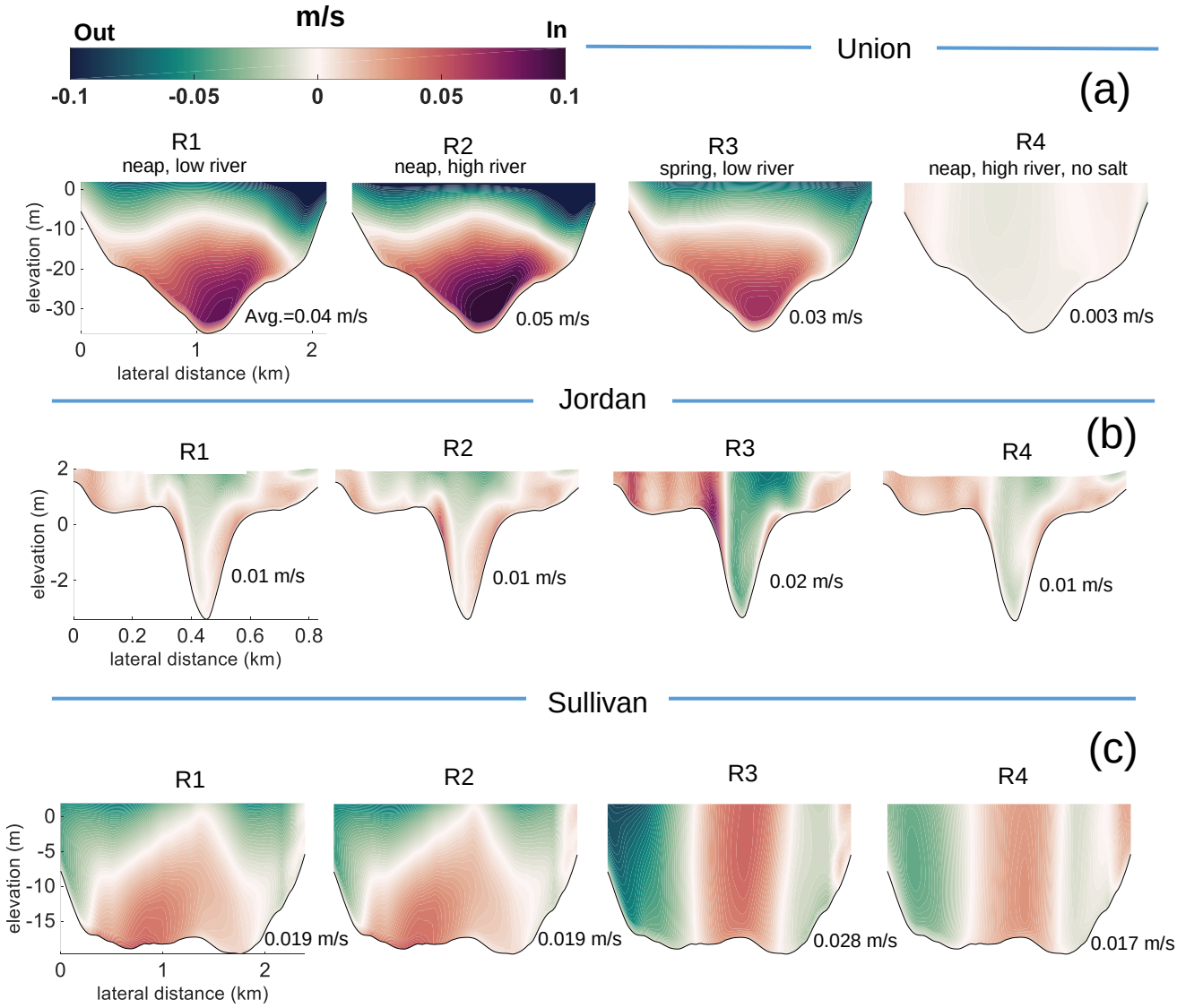

Figure 2. 6. Transects of along-channel residual flow near (a) the mouth of the Union River Estuary, (b) the mouth of the Jordan River Estuary, and (c) the mouth of the Sullivan estuary for different scenarios (R1: neap and low river discharge, R2: neap and high river discharge, R3: spring and low river discharge, and R4: neap, high river and barotropic). The perspective of all transects is landward. Red indicates in-estuary flow and green indicates out estuary flow.

2.5 Discussion

Results indicated that transport timescales are sensitive to density gradients driven by freshwater input in the Union River Estuary, to fortnightly tidal variations in the Jordan River estuary and to both tide and density gradients in the Sullivan Estuary. What remains unclear is if we can determine the drivers of the transport timescales in the studied estuaries by solely considering tidal range, freshwater input and estuary shape and generalize this procedure to be easily applied by stakeholders.

2.5.1 Linking Hydrodynamics to Particle Transport

Lagrangian particle trajectories can be chaotic, exhibiting random motion instead of following residual flow streamlines (Zimmerman, 1976). Relations between residual flow and Lagrangian particle trajectories rely on the scale of residual eddies relative to the tidal excursion (Zimmerman, 1979) where the tidal excursion ($L_{ex} = \frac{2U}{\sigma}$) is defined as the tidal velocity amplitude, U, over half of tidal frequency, σ, (Parsa & Shahidi, 2010). Streamlines of residual flow can provide a reasonable approximation of the net Lagrangian particle trajectories when the tidal excursion is small compared to residual eddy length (Signell & Butman, 1992). Exploring the relations between residual eddy length and tidal excursion in relation to particle transport can therefore explain why residence and flushing times can vary in estuaries of different dimensions exposed to different forcing by tides and freshwater input and density gradients.

In the Union River Estuary, during high river discharge (R2), residual streamlines directed up-estuary in the bottom half of the water column and down-estuary near the surface were found along the entire estuary (same pattern is observed for other baroclinic runs, R1 and R3) as

shown in Figure 2. 7a. This implies that the length scale of the streamlines are comparable to the estuary length (>10 km; Figure 2. 7b). The tidal excursion along the estuary is an order of magnitude shorter than the residual streamline length (Figure 2. 7b). This implies that the distance traveled by particles under the influence of the tide is shorter than the influence of the residual streamlines and residual flow dominates particle transport in this system. When visualizing the particle pathways with depth and along-channel distance, it becomes clear that the transport is dictated by the density-driven flow or typical estuarine gravitational circulation with particles released near the surface travelling down-estuary and particles released near the bottom travelling up-estuary (Figure 2. 7a, bottom layer), which reinforces that transport is dictated by residual flow (Figure 2. 6a). When the length of the residual streamlines are longer than the tidal excursion, estuary transport timescales become sensitive to the drivers of the residual flow. This explains why suppressing the density gradient in the Union River Estuary resulted in elevated residence (Figure 2. 5a, R4 and R2) and flushing times (Figure 2. 4a, R4 and R2).

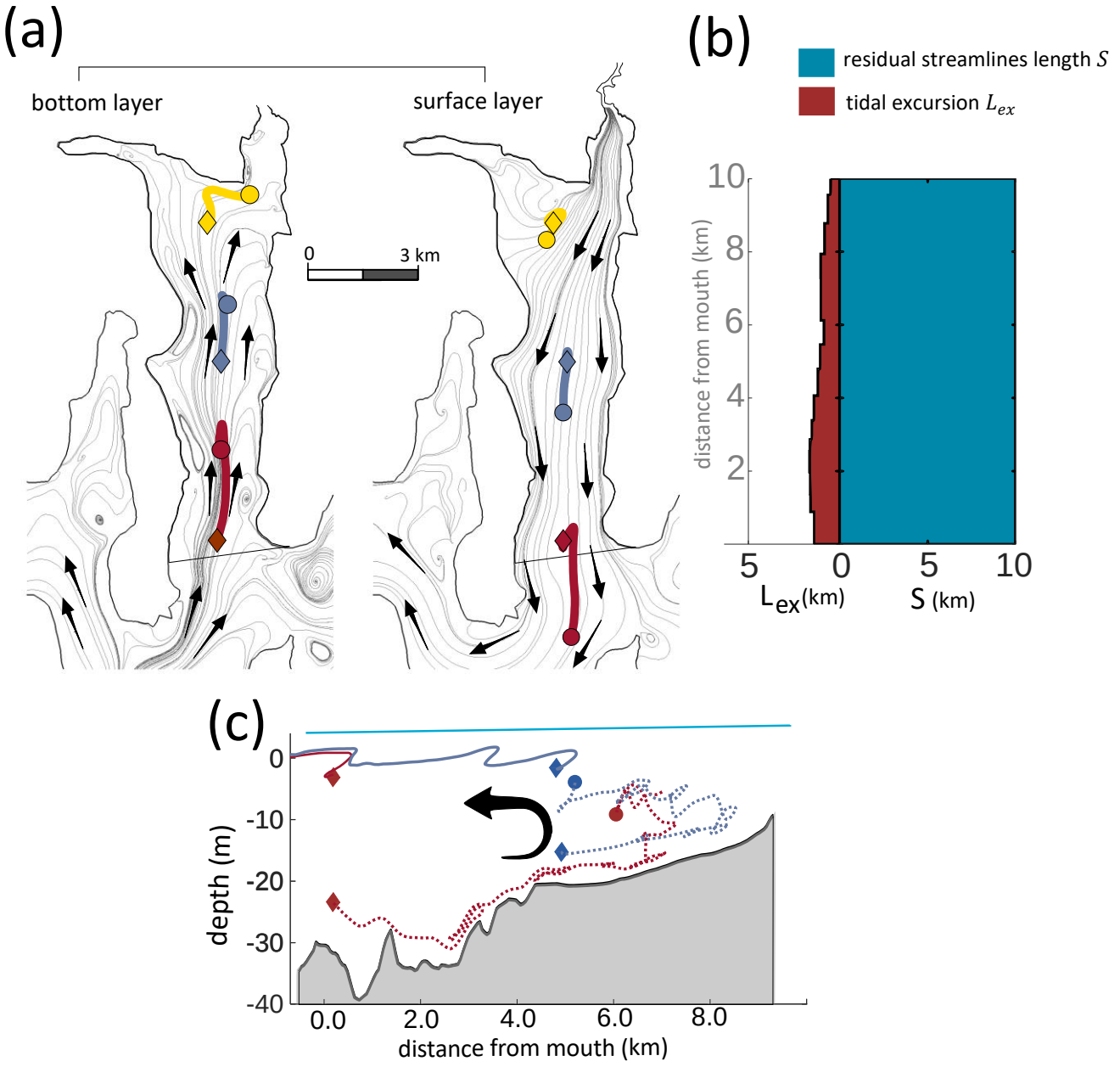

Figure 2. 7. For neap tide and high river discharge (case R2) (a) Residual streamlines in the surface and bottom layer in the Union River Estuary along with surface and bottom particle trajectories for one tidal cycle (diamond and circle refer to initial and final location respectively), (b) the tidal excursion (red) and residual streamline length in the system, (c) particle trajectories in the vertical plane for particles released near the surface (solid line) and near the bottom (dashed line). The arrows over the streamlines show the direction of the residual flow.

In other tidal systems such as the Danshuei River in Taiwan, Liu et al. (2008) showed that including the density decreased the residence time (approximately by 27%). They also demonstrated that particles released near the bottom of the system remain in the system more than the particles released near the surface conforming to gravitational circulation. Also, in Chesapeake Bay (Shen & Wang, 2007), when the density-induced circulation is reduced, the transport timescales increased by 50%. Similar to the residence time pattern in the Union River Estuary (Figure 2. 5a, R1-R3), Du & Shen (2016) showed that in the Chesapeake Bay, the residence time is longer at depth than it is in the surface layer due to the residual flow structure being dominated by gravitational circulation, reiterating the importance of residual flow structure and strength to particle transport. In Galveston Bay, Du et al. (2020) demonstrated that when the river discharge significantly increased due to hurricane Harvey, the transit time (average time for the particles to leave the bay) of the bay was reduced to 1.5 days instead of 60-90 days under normal river flow conditions. They showed that during the hurricane particle pathways were not influenced by the tide and particles moved seaward along the bay. In Caloosahatchee Estuary in Florida, USA, Wan et al. (2013) showed that introducing freshwater to the system, the average residence time considerably decreased (4 days with $57 m^3/s$ freshwater discharge) compared to the case with no freshwater (no density-gradient) case (60 days). Caloosahatchee Estuary behaved in a similar manner to Union River estuary in response to density gradient. Wan et al. (2013) reasoned that the long residence time in no density-gradient (no freshwater) case is engendered because only tide drives the flushing of the system. This articles, however, suggests that it is likely that in Caloosahatchee Estuary, residual flow circulation, the expected driver of

residence time when tidal current is relatively weak, is weakened when density-gradient is absence causing a remarkable increase in residence time.

In contrast to the Union River Estuary, the tidal excursion in the Jordan River Estuary is longer than the residual eddy length along the system. At the mid-reaches of the Jordan River Estuary (0.7 to 4 km from mouth) during high river discharge the tidal excursion length is equivalent to the estuary length (~ 5 km), while the residual eddy length is equivalent to estuary width (0.2- 1 km; Figure 2. 8b). This indicates that the distance traveled by particles due to the tide is an order of magnitude longer than the length of the residual eddies (Figure 2. 8a). Hence, the transport timescale in this system is more sensitive to changes in the tidal amplitude (spring-neap variation) and less sensitive to residual flows. During spring tide, the tidal excursion increases by 40% in the Jordan River. This explains why the minimum residence (*Figure 2. 5*b) and flushing time (Figure 2. 4b) in the system are found during spring tide; not because the residual flow magnitude is stronger but because the tidal excursion is longer. Also, when the tidal excursion is equivalent to estuary length, the residence time is expected to be in the same order of magnitude as the tidal period (Figure 2. 5b, R1-R4). This is because particles can travel over the entire estuary length within one tidal cycle regardless of their initial location. This implies that estuaries that are longer than the tidal excursion likely experience high residence times since the water particles are translated back and forth within the estuary due to tide before they leave. Although the tide drives the motion of the particles in the Jordan River Estuary, each eddy, depending on its magnitude and direction, gives a nudge to the particle pathway, augmenting the impact of the tide. For this reason, particles are not trapped in a closed loop, rather their motion is random. Predicting the particle location after one tidal cycle is therefore extremely

difficult, yet how far particles can travel (back and forth) is known through the tidal excursion. Even at locations where the tidal excursion is longer than the residual eddy size, such as the Jordan River Estuary, residual flows can be important in driving bed load materials (e.g. sediment) because the transport timescale of such materials is remarkably less than the scale of tidal periods (Signell & Butman, 1992).

Outside of the Jordan River Estuary in the Mount Desert Narrows (MDN) the tidal excursion reduces and residual eddy size increases as the width of increases in MDN (Figure 2. 8c) compared to Jordan River Estuary (MDN, Figure 2. 1b and 2. 8a). The residual flow, therefore, becomes more relevant to the particle motion once they leave the Jordan River Estuary. This can affect flushing time in the Jordan River Estuary since particles can be advected back into the system due to the tide, causing the flushing time to increase. The residual streamlines (Figure 2. 8a) developed in MDN drive the particles to Western Bay during neap and high river discharge condition. This elucidates why Jordan is connected to Western Bay during neap tide in the baroclinic cases (Figure 2. 4b, R1 and R2). When density gradient is suppressed, serval eddies develop in MDN changes instead of streamlines directed from west to east. This explain why Jordan River and Western Bay are not connected when no density gradient is involved. During spring tide, the tidal excursion increases in MDN compared to the residual streamlines and the particles motion are governing by the tide. The tidal excursion during spring tide is shorter than the MDN system. As such particles stay longer in the system during spring compared to neap tide (Figure 2. 4b)

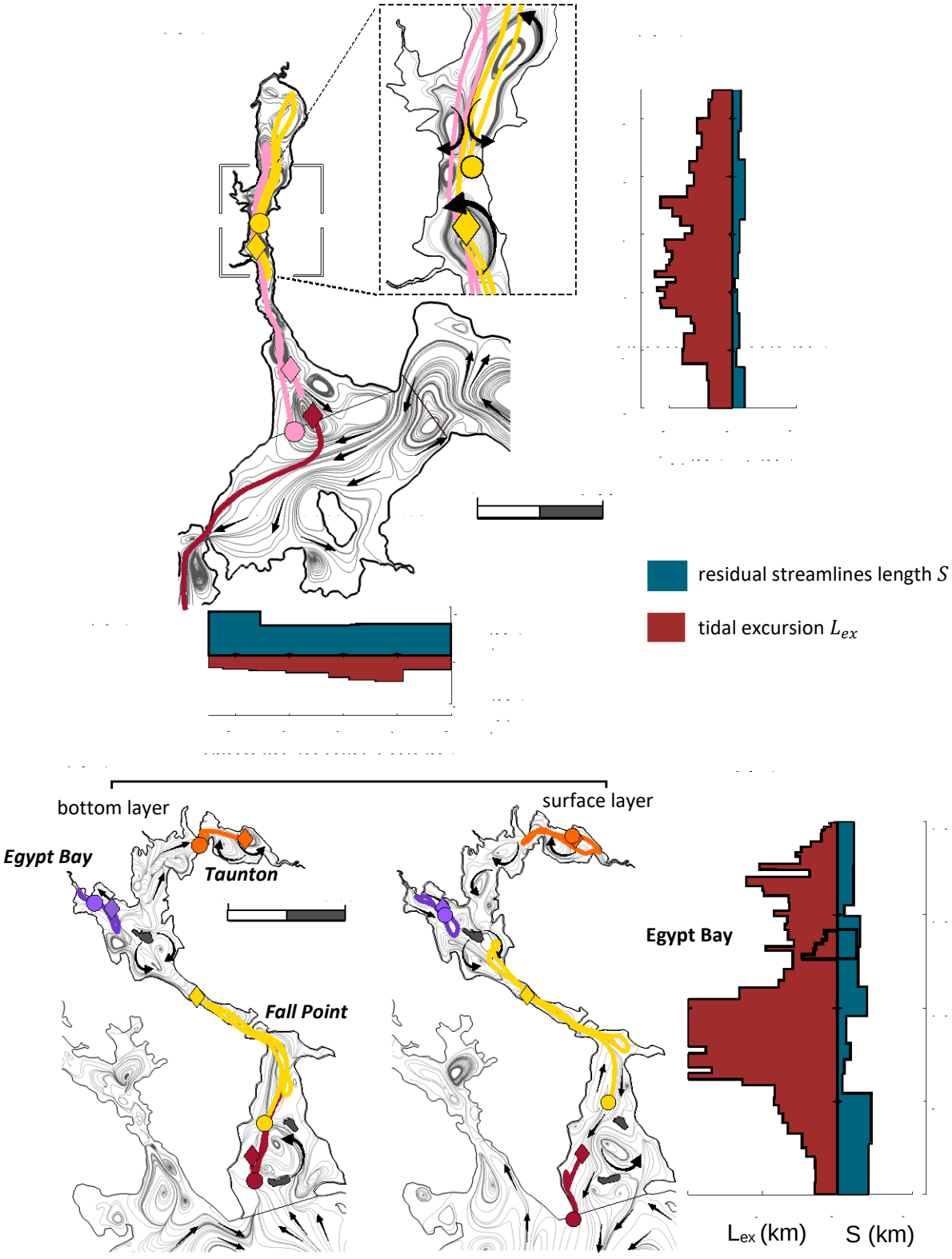

Figure 2. 8. For neap tide and high river discharge for one tidal cycle, (a) depth averaged residual streamlines and particles trajectories (b) and (c) are the tidal excursion (red) and residual eddy size (blue) in Jordan River and Mount Desert Narrows (MDN) respectively, (d) bottom and surface residual streamlines and particles trajectories for in Sullivan estuary, (e) the tidal excursion and residual eddy size in Sullivan. The arrows over the streamlines show the direction of the residual flow. Diamond and circle refer to initial and final location respectively.

Similar to the Jordan River Estuary, the tidal excursion length exceeds the residual eddy length scale at most locations in the Sullivan estuary (Figure 2. 8e), especially near the mid-reaches (6-8 km from the mouth) where the tidal excursion is ~10 km while the residual eddy length is ~0.5 km indicating particle motion is driven by the tide (Figure 2. 8d). However, near the mouth and head of the estuary (in Taunton and Egypt Bays), the tidal excursion reduces to ~ 1 km and the residual eddy length (~ 2.5 km) is more influential to the particle motion. Therefore, the mechanisms that drive particle motion inside the Sullivan Estuary vary spatially. The presence of islands and headlands as well as the width constriction in the Sullivan Estuary limits the eddy size allowing the tide to affect the transport timescales of the system. This is in accordance with Geyer & Signell (1992), as they argued that in systems with headlands and complex morphological features, tides play a major role in dictating the flushing time. This is why an increase in tidal excursion during spring tide in the Sullivan Estuary leads to a decrease in residence and flushing times (Figure 2. 5c and Figure 2. 4c). However, due to the spatial variation in estuary shape, the transport time scale is affected by both tide and residual flows due to the relationship between tidal excursion and residual eddy length.

The dimensions of residual eddies that determine whether tidal currents or residual flows drive particle transport are difficult to quantify and assess, and an insurmountable task for resource managers to estimate without access to simulation data from computational models. However, it can be assumed that the maximum eddy length is constrained by the width of the system or the distance between two prominent morphological features such as islands and constrictions in an estuary (Geyer & Signell, 1992). Based on hydraulic simulation case studies, it can be reasonably assumed that residual flow is likely to dominate the transport timescales if the

width of a system is larger than the tidal excursion length. An estuary with a width shorter than the tidal excursion length will be dominantly driven by tidal currents. This is evident through the relationship between the estuarine width and tidal excursion explored in Figure 2. 9 considering neap and high river discharge. The width of the Union River estuary exceeds the tidal excursion length (width > L_{ex}, Figure 2. 9), indicating that residual flow will govern the transport of particles in the system. This is in line with what it is deduced from the hydrodynamic simulations. The tide dominates particle transport in the Jordan River estuary because the eddy length is confined by the width of the system, which is less than the tidal excursion length (narrow estuary; width < L_{ex}). By the same token, the transport timescales in Sullivan Estuary are driven by the tide at most of the locations (width < L_{ex}).

Geomorphically induced eddies can produce particle trapping if the eddy length is longer than the tidal excursion length in a localized area. or quick flushing if the eddy length is shorter than the tidal excursion length. Transport patterns and mechanisms can thereby vary along-estuary in estuaries with internal variations in estuary morphology. Near the mouth of the Sullivan Estuary, the width is comparable to the tidal excursion length, which puts this along-estuary location in the category with residual flow-driven particle transport (width =2.8 km and tidal excursion =2.4 km, Figure 2. 9).

Exploring the relations between estuarine width, morphology, and tidal excursion length provides a practical guide for coastal managers to determine dominant controls of particle transport in a location of interest and provide a basis for assessing coastal vulnerability to pollution problems.

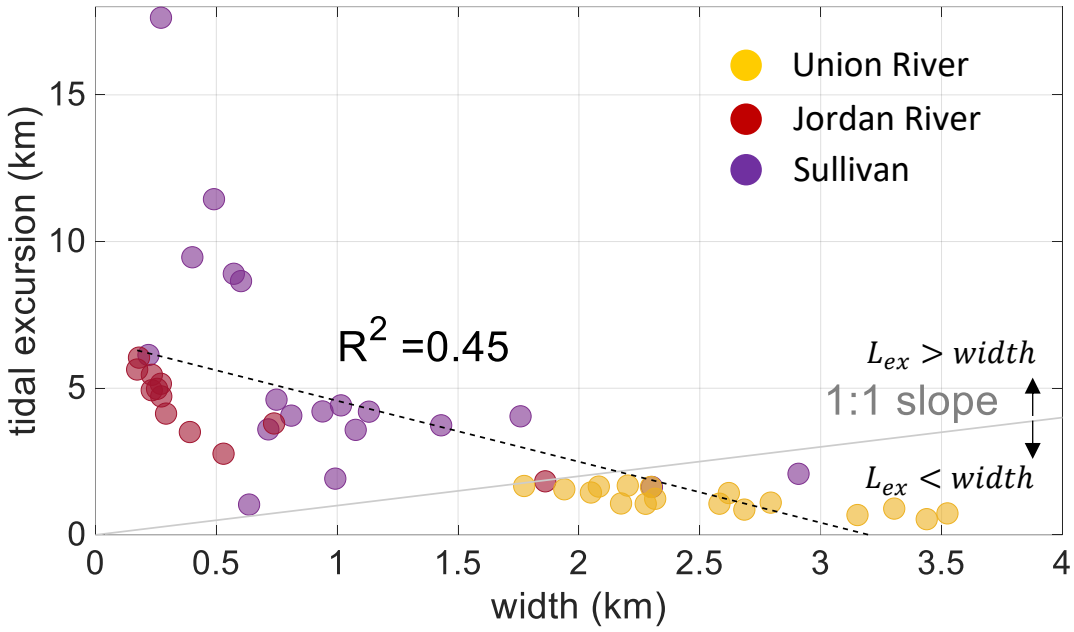

Figure 2. 9. The relationship between the estuary width and tidal excursion indicating that when the width is less (greater) than the tidal excursion, the oscillating tide (does not) contribute to the flushing of the system and the flushing is tidal sensitive (residual flow sensitive).

2.5.2 Model Limitations and Uncertainties

Incorporating additional information such as wind, temperature and realistic time varying river discharge measurements could further improve the model prediction of particle motion. Wind can affect residual flow and salinity structure, which affects residence and flushing times in estuaries (Geyer, 1997; Guo & Valle-Levinson, 2008). In studies that require precise predictions particle motion such as hindcasting/forecasting (Du et al., 2020) or backward tracking of particles (Callies et al., 2011), the influence of wind becomes important and is exacerbated in systems where residual flow dictates the Lagrangian particle motion. Considering time varying river discharge and temperature is also important as they alter the density gradients and, consequently, influence the residual circulation.

Aside from the physical setup of the model, issues related to numerical setup pose another source of uncertainty. When using the $k\varepsilon$ model instead of the mixing length model for turbulence closure in some cases the flushing time reduced by an average of 0.8 days in all considered systems as shown in Figure 2. 10.

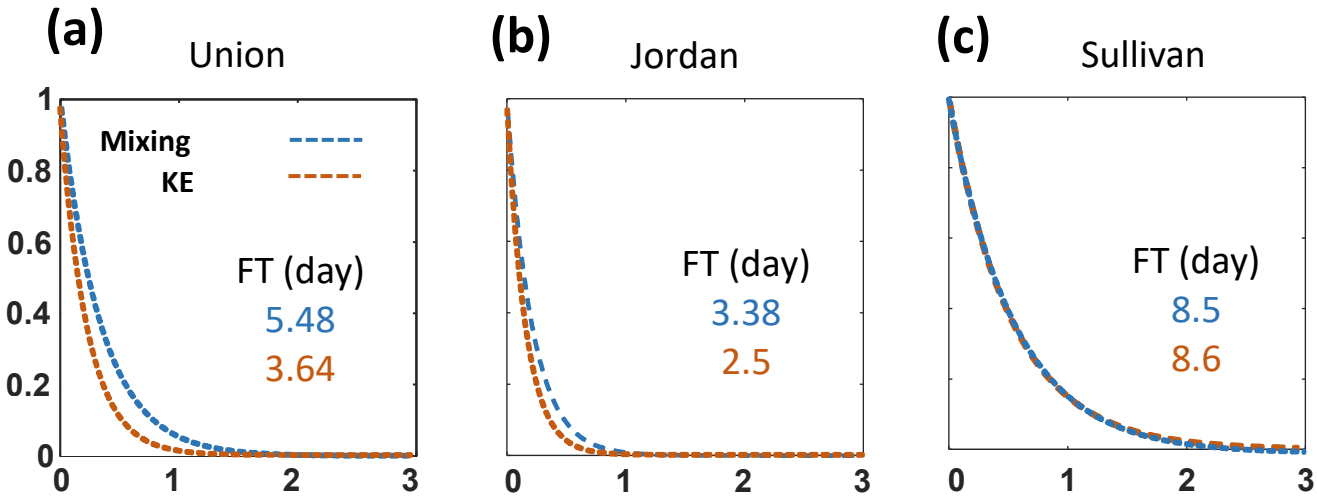

Figure 2. 10. Flushing time in (a) Union River, (b) Jordan River, and (c) Sullivan estuary using the Mixing Length and κε turbulence closure models.

The impact of changing the turbulence closure is mostly apparent in Union River Estuary (Figure 2. 10a) as the flushing time reduced to 3.6 days when using $k\varepsilon$ (C1 case in Table 2. 2) as appose to 5.5 days when using the mixing length (R2 case in Table 2. 2). The flushing time in Jordan River Estuary is reduced by around 0.8 day when using $k\varepsilon$ in lieu of the Mixing Length (Figure 2. 10b). The Sullivan Estuary, on the other hand showed no sensitivity to the change in turbulence model (Figure 2. 10c).

The numerical time step (the rate at which N-S equations are solved marching forward in time) could be a critical factor in altering the numerical outcomes. The impact of the numerical time step on the flushing time in Jordan River and Sullivan Estuary is portrayed in Figure 2. 11

where the cases R4, C2 and C3 in Table 2. 2 are considered and compared. Generally, changing the numerical time step (from 10 s to 5 and 1 s) varied the flushing time by 0.3 days on average with standard deviation of 0.3 days.

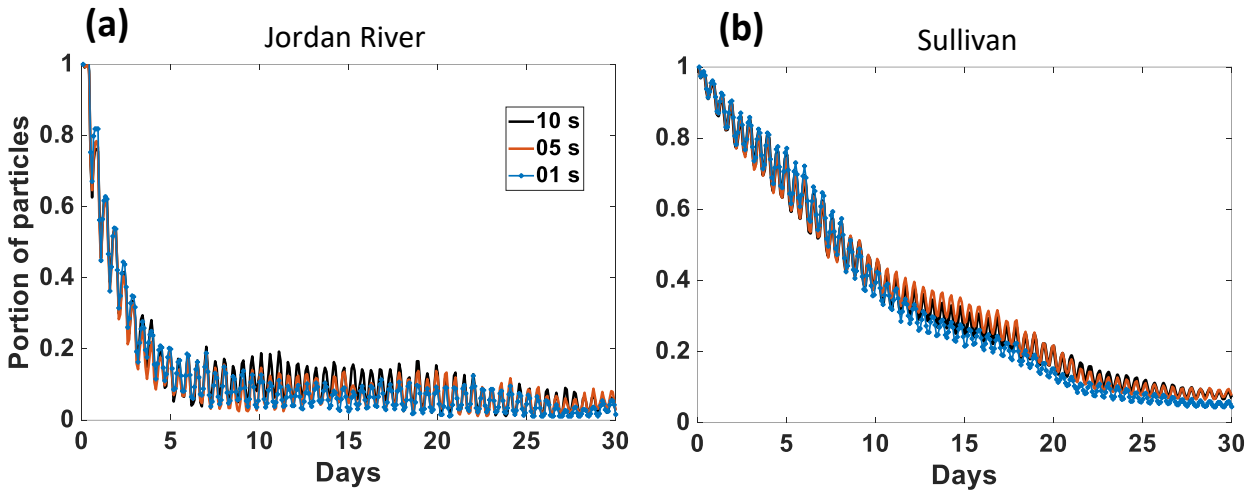

Figure 2. 11. The flushing time in (a) Jordan River and (b) Sullivan Estuary highlighting the influence of changing the numerical time step.

Although, the average transport timescales (i.e. flushing time) are not extremely sensitive to change in numerical time step, individual particles pathway may change dramatically when changing the time step as shown in Figure 2. 12. The latter details a five days' trajectory of two particles from R4 run (10 s timestep) and C2 run (5 s timestep) released at the same location in Sullivan system. The particles followed a similar pathway over a relatively short time (two tidal cycles) before they started to follow two different pathways. This can be ascribed to the truncation error and machine precision (round off error) since the solution at each time step is rounded to the 10^{-8} digit (not infinite precision). Thus, for the same model with a different time step, a slight shift in the particle trajectory at each time step due to these small errors accumulates resulting in a difference in the particle pathway over sufficiently long periods. As a

result, individual particles can show a variation in residence time that could reach up to ±2 days when changing the time step. For this reason Cucco et al. (2009) argued that using an Eulerian approach to describe the long-term transport timescale is better than the Lagrangian approach due to the chaotic behavior of the particles. Another limitation of the current model is that biological and biochemical processes were not included. Thus, particle numbers (mass) cannot be a direct indication to the mass of pollutants.

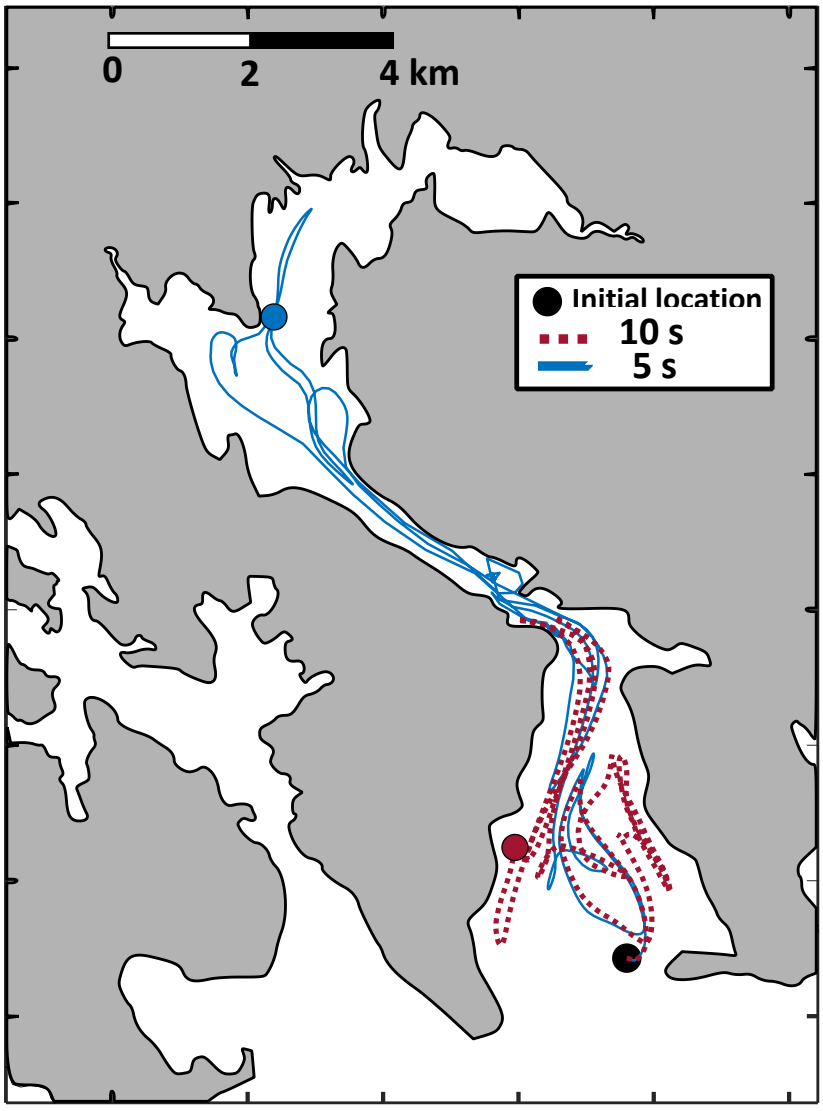

Figure 2. 12. *Particles pathways in five days is Sullivan Estuary with 10 s and 5 s time numerical timestep.*

2.6 Conclusion

Lagrangian analysis in hydraulic scenario simulations provides a basis to evaluate flushing and residence times in a system of connected estuaries in Frenchman and Blue Hill Bays in Maine, USA. Neutrally buoyant and conservative particles were released and tracked over a period of thirty days considering high-low river discharge, spring-neap tidal cycles, and baroclinic-barotropic conditions. Residual flows drive the particle movement and control the transport timescales in estuaries where residual eddy length is longer than the tidal excursion length as illustrated in Figure 2. 13b and c. Residual flow drivers such as river inflow rates and density gradients related to salt concentration can play a major role in determining estuary flushing behavior. Suppressing the density gradient in such systems results in an order of magnitude increase in residence and flushing time. In addition, particles can be trapped in the residual eddies developed due to the shape of the system resulting in an increase in the transport timescales (Figure 2. 13d).

Narrow channels and the presence of complex morphological features in tidally driven estuaries limit the residual eddy length and enlarge the length of tidal excursion compared to the eddy size. The transport timescales in such systems are driven by tides and estuary transport times are less responsive to residual flows and more responsive to changes in tidal range (spring-neap cycle). In systems where tidal excursion length is comparable to estuary length, residence time can be less than or equal to the tidal period (Figure 2. 13a). Transport times under these conditions rely on the particle motion inside the system and on the external circulation patterns that govern whether the particles can return to the estuary during the subsequent tidal cycle. This will also affect the connectivity between estuary embayment. In locations where tidal

excursion is longer than residual eddy size and shorter than the length of the system, particles will be retained to result in long transport timescales (Figure 2. 13d).

The current observations demonstrate that the relative influence of tidal currents or freshwater inputs on particle movements and duration of the transport time in a location of interest is highly dependent on the geomorphological conditions. Coastal geomorphological attributes such as estuary width and length, as well as the presence of island landforms, provide a reasonable basis and practical approach for managers to determine primary controls on particle movements. Knowledge of the relations between coastal geomorphology and hydrodynamics driving particle movement is important to the prediction of climate and ocean change effects on coastal water quality, planning of pollution monitoring infrastructure, and determination of strategies for coastal resource sustainability solutions related to fisheries and recreation uses.

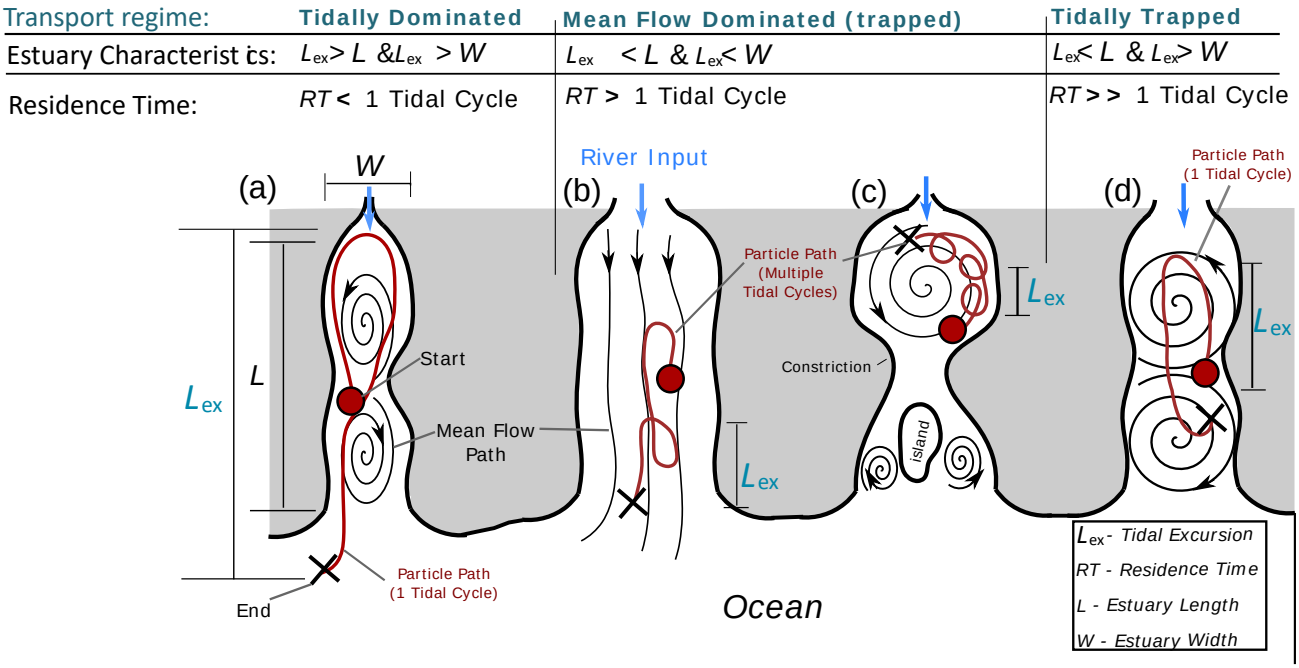

Figure 2. 13. Conceptual particle trajectories and residual streamlines systems with different shape where the width (w) and the length are shorter than the tidal excursion L_{ex} (a), the width (w) is greater than the tidal excursion L_{ex} (b), (c) and where the tidal excursion is longer than the width and shorter than the length of the system (d).

CHAPTER 3

RESIDUAL FLOW IN A MACROTIDAL ESTUARY

This chapter investigates the residual flow and the transport timescales (residence and flushing time) in a macrotidal (tidal range>4 m) and convergent estuary. The first section of the chapter concerns the along-channel residual flow pattern and drivers along the Gironde, a prototypical macrotidal and convergent estuary in France, with emphasis on density gradients and advection as forcing drivers for the residual flow. The second section of the current chapter focuses on the flushing and residence time of the Gironde and the impact of density gradients, advection and river discharge on altering the transport timescales in the system.

3.1 Residual Flow in a Macrotidal and Convergent Estuary

This section explores the along-channel residual flow (magnitude and transverse structure), forcing mechanisms and their variations along the Gironde estuary. With emphasis on the role of density gradient and the advective accelerations in the along channel momentum balance, the study outlines the along-channel residual flows and forcing mechanisms over the neap-spring tidal cycle during high and low river discharge conditions.

3.1.1 Introduction

Residual circulation (flow) is important for the net transport of sediments, contaminants, and other water-borne materials in estuarine environments (Burchard & Hetland, 2010; Prandle, 2004; Wong, 1994). As such, the health of an estuary depends heavily upon this circulation (Stacey et al., 2001). It has been long thought that gravitational circulation (the balance between the longitudinal density (salinity) gradient and stress divergence with constant eddy viscosity) is

the main driver of residual flows As proposed by Hansen & Rattray (1965). However, studies have shown that other processes such as advection (Basdurak & Valle-Levinson, 2012; Lerczak & Geyer, 2004), wind (X. Guo & Valle-Levinson, 2008; Sanay & Valle-Levinson, 2005; Wong, 1994), Earth's rotation (Valle-Levinson et al., 2003; Winant, 2008) and curvature (Chant, 2002), Eddy Viscosity-Shear covariance (Cheng et al., 2019; Dijkstra et al., 2017) (which includes tidal straining (Burchard & Hetland, 2010) can be of importance in contributing to residual flows besides gravitational circulation. To mention some examples, Burchard & Hetland (2010), using an idealized numerical model, suggested that for periodically stratified tidal estuaries, tidal straining could be twice as important as gravitational circulation in creating residual circulation. Cheng (2014) found that advective acceleration dominated over the longitudinal density gradient in generating the residual flows in his numerical study in an idealized, weakly stratified estuary. The longitudinal variation of bathymetry, estuarine width and depth were not considered in the latter two studies. When investigating residual flows from observations in the James River, Basdurak & Valle-Levinson (2012) showed that advection is as important to the along-channel momentum balance as the pressure gradient and friction. Their study was based on data collected at two transects, 1.5 km apart near the mouth of James River. As it will be demonstrated in this paper, however, it is hard to generalize findings regarding the residual flow drivers in non-idealized systems based on localized measurements. This is because the relative importance of these drivers can significantly change over a relatively short distance.

In addition to varying longitudinally, estuarine residual flows and circulation can exhibit a fortnightly variability. Scully et al. (2009) showed that the gravitational circulation is enhanced

during neap tide (40% less during spring tide) in the Hudson River estuary due to fortnightly variations of vertical mixing.

In the macrotidal and convergent Gironde estuary, Ross et al. (2017) found that cross-channel variations in tidal nonlinearities (internal tidal asymmetry and advective accelerations) affected the lateral strength and structure of subtidal flows and that this effect varied from neap to spring tide. This result was surprising since previous work on this system (Allen, 1980) indicated that subtidal flows were solely a product of along-channel density gradients. However, the study by Ross et al. (2017) was carried out using data collected in a one single cross-section at the mid-reaches of the estuary, making it impossible to determine if the reported subtidal flow patterns and drivers were maintained along the system.

The transverse variation in strength and structure of residual flows has indeed been found to be affected by bathymetry, channel width and depth and length (Chant, 2002; Li & O'Donnell, 1997, 2005; Valle-Levinson et al., 2003; Wong, 1994; Zimmerman, 1978). Wong (1994) demonstrated that gravitational circulation exhibits a two-layer flow pattern with inflow at depth and outflow at the surface (vertically sheared flow) in a rectangular channel. However, in a triangular channel, this flow pattern becomes more complex, characterized by inflow over the deepest part of the channel and outflow over the shoals (laterally sheared flow). Wong (1994) considered a constant (effective) eddy viscosity over the channel cross section, however, considering a variable eddy viscosity may be a step closer to better represent the flow in more realistic scenarios. Friedrichs & Hamrick (1996), in their study on James River, suggested that lateral changes in eddy viscosity has to be acknowledged in channels with lateral depth variations to better represent the flow in such systems. In a more complex model that includes spatial and

temporal variation in eddy viscosity as well as advective accelerations, Burchard et al (2011) showed that in tidally energetic estuaries with a parabolic cross-channel shape, the gravitational circulation produces a laterally sheared flow in shallow channels transitioning to vertically sheared flow as the depth increases. They also found that advective accelerations produce a laterally sheared flow with inflow in the channel and outflow over the shoals, and that the relative contribution of advection-induced flow to the total residual circulation increases as the channel narrows and deepens. In a channel with Gaussian bed profile and various depth-to-width ratios, gravitational circulation induces a persistent vertically sheared flow that is more pronounced in narrow compared to wide systems (Schulz et al., 2015). The study by Schulz et al. (2015) also showed that advection-induced flow exhibits a complex pattern (vertically and laterally sheared flow) in wide estuaries that negligibly contribute to the total residual flow. However, in narrow systems with parabolic cross section, the advection-induced flow becomes vertically sheared (with inflow near the bottom and outflow at the surface) and significantly contributes to the total residual flow. Although, the most of the aforementioned studies considered simplified bed profiles, similar patterns as those reported in these studies have been identified in realistic systems. Based on data from the Chesapeake Bay (bathymetry and velocity profiles), Huijts et al. (2009) and Zitman & Schuttelaars (2012), for instance, showed that the gravitational circulation is laterally sheared with inflow in the channel and outflow over the shoals. Also, both studies showed that advective accelerations produced a complex laterally sheared flow with a magnitude comparable to the gravitational circulation.

Studies focusing on idealized estuarine geometries have provided critical insight on how residual flow magnitude and structure, and the relative contribution of individual driving

mechanisms, are affected by lateral and longitudinal changes in bathymetry, tide, and freshwater input (salinity gradients). Realistic macrotidal estuaries are characterized by complex lateral bottom profiles, longitudinal variations in bathymetry and strong tidal forcing, which all affect the residual flow dynamics. Therefore, in such systems, where idealized assumptions may not hold, the residual flow can exhibit complex spatial variations and drivers. To this end, this study aims to determine the longitudinal and transverse variation of along-channel residual flow structure and forcing mechanisms in a macrotidal and convergent estuary using realistic bathymetry. To reach this goal, a three-dimensional numerical model is utilized considering the Gironde estuary as a case study. In the Gironde estuary, Allen et al. (1980) suspected that tidal processes (flow induced by the barotropic tide) is as important in driving residual flows as density processes (density-induced flow). The current study therefore pays particular attention to the relative contribution of density-driven flow to the total residual flows. Further, due to the complex bathymetry and strong tidal forcing, the role of advective accelerations in driving the residual flow will also be investigated thoroughly. The remainder of this paper will be as follows. Section 2 describes the study site, the Gironde Estuary, in detail. Section 3 elaborates on the density-driven flow definition and explains the numerical model setup and validation. The model results for high and low river discharge during neap and spring tides are reported in Section 4. Section 5 discusses the major findings of this study and how it relates to other studies. Finally, the concluding remarks are presented in Section 6.

3.1.2 Study Site: The Gironde Estuary

The study area is the Gironde estuary, located on the southwest coast of France (Figure 3. 1a). The Gironde estuary is macrotidal with a maximum spring and neap tidal range of ~5 m

and 2 m, respectively, at the mouth of the estuary (Bonneton et al., 2015). The tidal range is amplified toward the head due to the effect of channel convergence outweighing frictional influence (Bonneton et al., 2015). During dry seasons, the tidal intrusion length extends up to 180 km upstream (Jalón-Rojas et al., 2015).

The morphology of the main body of the estuary (from Pauillac to downstream Richard) has an average width of 7.5 km featuring a main channel on the western side of the estuary and shoal on the eastern side. At the mouth, the morphology becomes more sophisticated and is characterized by a constriction that reduces the width to 5.0 km, a headland, and two channels separated by a shoal in the middle (Figure 3. 1b).

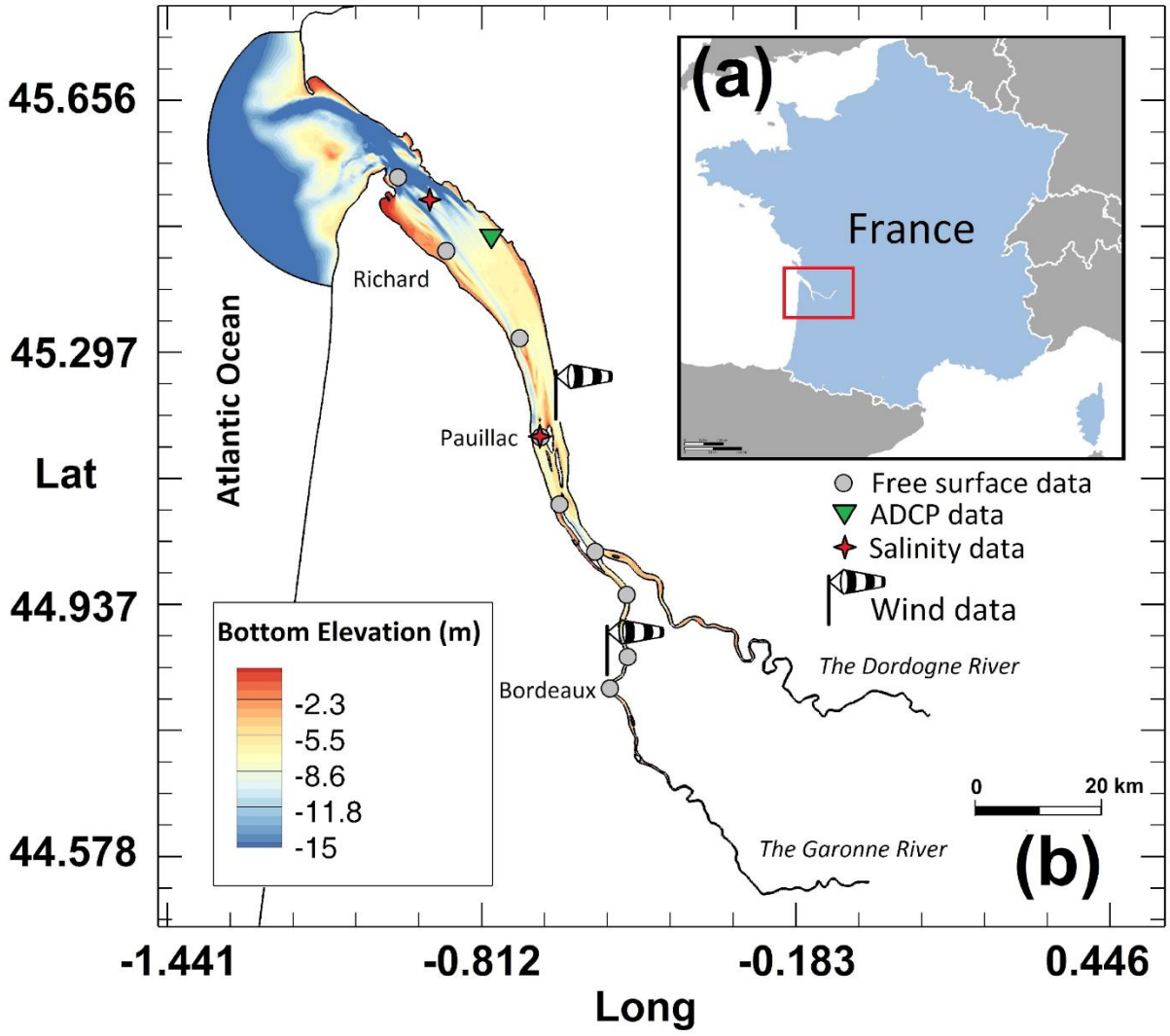

Figure 3. 1. The location of the Gironde (a) in relation to France and (b) a zoom-in of the estuary that details the bathymetry (described by the color map) and the location where the measured free surface level (gray circles), velocity (green triangle), salinity (red stars) and wind data (wind cones) were collected.

Upstream of Pauillac, the estuary contains multiple small islands and channels (Ross et al., 2017). The estuary receives freshwater from two rivers, the Garonne and the Dordogne, that converge ~75 km from the mouth of the estuary. These rivers produce a mean annual flow of 680 m^3/s for the period January 2005 to July 2014 (Jalón-Rojas et al., 2015). The daily river input can vary significantly depending on the season. The river input from Garonne and the Dordogne, for

instance, reached 3,500 m^3/s during the wet season and was reduced to 200 m^3/s during the dry season of 2015 (obtained from the public information system of France, http://www.hydro.eaufrance.fr/). This seasonal variation in freshwater input creates a seasonal variability in the stratification conditions in the estuary, making the estuary well-mixed during the dry season and partially stratified during the wet season (Allen et al., 1980).

3.1.3 Methodology

The proceeding section highlights the numerical model employed in this study, the definition of density driven flow, the model configuration, and the numerical experiments.

3.1.3.1 Numerical Model and Density Driven Flow.

To pursue the objectives of this study, numerical experiments were carried out using Telemac3D, a finite-element model which solves the 3-dimensional shallow-water equations, including water constituent transport such as salinity (Hervouet, 2007; Janin et al., 1992; Moulinec et al., 2011). The numerical results are used to evaluate the lateral structure and strength of along-channel residual flows, as well as the evolution of the forcing mechanism driving these flows along the estuary. The models solves the 3-dimentional Reynolds Averaged Navier-Stokes (RANS) equations (see Hervouet, 2007 for instance). The tidal average of the along-channel momentum balance of the RANS equations for a system with a non-uniform density field (non-homogenous) reads

$$\overline{\mathrm{u}\mathrm{u}_\mathrm{x}} + \overline{\mathrm{v}\mathrm{u}_\mathrm{y}} + \overline{\mathrm{w}\mathrm{u}_\mathrm{z}} - f\overline{v} + \frac{\overline{uv}}{R} = -g\frac{\partial\overline{\eta}}{\partial x} + \overline{\frac{g}{\rho}\int_{-z}^{\eta}\rho_x\,dz} + \overline{\left(Az\ \mathrm{u}_\mathrm{z}\right)_z} \qquad 3.1$$

where u, v and w are the velocity components in x, y and z directions respectively. In this work, x and y refer to the along channel and cross channel direction. f denotes Coriolis frequency, R is the radius of the estuarine curvature ($R \approx 49\ km$ evaluated by averaging the outer and the inner bend radii of the estuary), Although R varies with space, a constant R is considered since the desire is to investigate the order of magnitude of the centrifugal force in Eq. 3. *1*. The free surface elevation is denoted by η in Eq. 3. *1*, ρ_0 is a reference density (1000 kg/m^3), ρ is the water density and Az is the eddy viscosity. The subscripts (x, y, z) denote the differentiation operation with respect to $x, y\ and\ z$ coordinate. The overbar indicates a tidally averaged value. The primary (along-channel) flow, u, and secondary flow, v, are distinguished based on Rhoads & Kenworthy (1998). Although, the terms in Eq. 3. 1 are extensively described in the literature, a brief explanation of each term of Eq. 3. 1 is provided herein. The first term on the left hand side (LHS) of the Eq. 3. 1 is the longitudinal advection, which can be described as the transport of the longitudinal change of the along channel velocity by the along channel velocity. The second term on the LHS represents the lateral advection, which is the transport of the lateral change of the along-channel velocity by the lateral velocity. The third term on the LHS denotes the vertical advection which is the transport of the vertical change of the along-channel velocity by the vertical velocity, w. The forth and the fifth terms on the LHS are Coriolis (due to earth's rotation) and curvature (due to change of direction of the primary flow), respectively. On the right hand side (RHS) of Eq. 3. 1, the first term represents the baroclinic pressure gradient, which can be defined as the along-channel slope of the free surface. The second term on the RHS is the baroclinic pressure gradient, which arises due to the spatial variation in the density field. The third term on the RHS is the stress divergence which represents internal friction.

The presence of the of the density gradient (baroclinic pressure gradient) in estuaries can alter the residual flows not only through baroclinicity as proposed by Hansen & Rattray (1965) or Wong (1994) for instance, but also through impacting other terms such as eddy viscosity, velocity shear (Cheng, Mao, et al., 2019; Dijkstra et al., 2017), and advection (through differential advection) (Lerczak & Geyer, 2004). In this study, the density-driven flow is defined as the difference between the flow in a barotropic system (no density gradient) and the flow in the same system with the presence of a density gradient. With this definition, the density-driven flow is the flow induced by the baroclinic pressure gradient and by the tide-density field interaction (following Guo & Valle-Levinson (2007, 2008) and Li et al. (1998)). The relative contribution of density-driven flow at any section along the estuary can be then evaluated as follows

$$\xi = \frac{\int_A |u_D|}{\int_A |u_{bt}|} \qquad 3.2$$

where *A* denotes the cross-sectional area of the channel, $|u_D|$ and $|u_{bt}|$ are the absolute value of the along channel density-driven flow and the absolute value of the residual flow in the homogeneous (or barotropic) case, respectively. It is worth mentioning that it is possible for ξ to have a value that is greater than unity ($\xi > 1$ or $> 100\%$) if the density-driven flow is stronger than the residual barotropic flow. This is an indicator that the system is density-driven for a given location along the estuary. The study shows that a value of ξ that is greater than 75% at a specific location along the estuary suggests that the residual flow structure will be similar to the density-driven flow structure (in-estuary flow over the deep and out-estuary flow over the shallows).

3.1.3.2 Model Configuration and Validation

The model domain covers the Gironde estuary depicted in Figure 3. 1b. The model is discretized in the horizontal plane using an unstructured mesh that varies in size from 200 m near the ocean boundary to 50 m in the main body of the estuary. In the vertical plane, there are 20 equidistant sigma layers (terrain-following layers). The diffusion terms of the velocity and salinity are discretized using the built-in implicit scheme. The Characteristics scheme is used for the advection of velocity and the Explicit MURD (Multidimensional Upwind Residual Distribution) tidal flat scheme for the advection of salinity (Hervouet, 2007). For turbulence closure, the Tsanis mixing length model is implemented. The closure expresses the eddy viscosity as follows

$$Az = f(Ri)\, Lm^2 \sqrt{\left(\frac{\partial u}{\partial z}\right)^2 + \left(\frac{\partial v}{\partial z}\right)^2} \qquad 3.3$$

where Lm is the mixing length which can be estimated using the following equation

$$Lm = \begin{cases} kz \quad if\ z \leq 0.2h \\ 0.2\ kh\ if\ z \geq 0.2h \\ kd\ if\ z \geq 0.8\ h \end{cases} \qquad 3.4$$

in which, z represents the distance from the bottom, h is the water depth, d is the distance to the free surface and $k = 0.4$ is the Von-Karman constant. Along with the mixing length model, the Munk-Anderson damping function $f = \frac{1}{(1+10Ri)^{1.5}}$ in which Ri is the gradient Richardson number $\left(\frac{\frac{g\partial\rho}{\rho\partial z}}{\left(\frac{\partial u}{\partial z}\right)^2 + \left(\frac{\partial v}{\partial z}\right)^2}\right)$, is implemented to account for stratification (Uittenbogaard, 1994). The stress at the bottom is estimated using the Strickler law whereas the stress at the sidewall (the islands and the boundaries) uses a slip condition. The Strickler coefficient was assigned based on

the sediment type at the bottom provided by Allen (1973) and therefore is spatially variable. Using a built-in algorithm, the wind stress at the surface is imposed by interpolating the wind data provided near Pauillac and Bordeaux (Figure 3. 1b) over the entire domain. The wind is only imposed during the validation process (validation run) and it was excluded for the other runs (see Table 3. 1). The objective of including the wind during the validation process is to avoid over tuning the model to match the measured data. Thus, including the wind during validation makes the model more representative for the Gironde estuary. For the same reason, hourly river discharge obtained from Eaufrance (http://www.hydro.eaufrance.fr/) is forced at the upstream boundaries for model validation (see Figure 3. 2a where the river discharge during the validation period shown in this article is reported for the Garonne and Dordogne). The tide is forced at the ocean boundary based on the recent TPXO (global tidal solution) database (Egbert & Erofeeva, 2002). Salinity, which was initialized along the estuary using data (more details below), is also forced at the ocean boundary with a constant value of 35 psu. and Coriolis were also included in the model.

The simulated water level, velocity, and salinity were compared with the corresponding measured data. The water level along the estuary was collected from nine tide gauge stations from Le Verdon (mouth) up to Bordeaux, ~90 km upstream (see Figure 3. 1b) for the year 2015 (data provided by the Port of Bordeaux). Velocity measurements were obtained from an Acoustic Doppler Current Profiler (ADCP) moored near Richard for six months from June to November of 2015 (during the dry season). Near the mouth, salinity profiles were collected using a Seabird 19 Plus Conductivity, Temperature, Depth (CTD) profiler on November 2, 2016 for one tidal cycle (12

h) whereas the surface salinity near Pauillac was provided from the MAGEST (http://magest.oasu.u-bordeaux.fr/) database.

The numerical model was initialized with a salinity gradient estimated from the measurements. This gave the advantage of shortening the overall model initialization and 'spin-up' process required to equilibrate the salinity field in the estuary.

The model was run for 35 days starting October 1st, 2015, encompassing the time when all field data were available, to capture the fortnightly variation in the tide, and to ensure that the model is spun up (given 30 days before comparing the data with the model) in regards to flow and the salinity field, and was then compared to the data for validation. The model validation run used a time step of 60 s, including the realistic wind field and river discharge and Coriolis was activated. The model output was recorded every 30 minutes. The measured and simulated water level, velocity and salinity are reported in Figure 3. 2.The amplification and the distortion of the tidal wave, downstream to upstream, are both predicted by the model as shown in Figure 3. 2b. The R-square (R) values (0.99 at Richard and 0.98 at Bordeaux) reported in the figure indicate a high correlation between the model and the measurements with a root mean square error (RMSE) of 0.08 m at Richard and 0.2 m at Bordeaux. The model also agrees with the measured velocity near the surface (R=0.94, RMSE=0.08 m/s) and near the bottom (R=0.94, RMSE=0.07 m/s) as depicted in Figure 3. 2c. The model demonstrated a high proficiency in predicting the salinity as compared with the measured values at Richard (R=0.99, RMSE=0.17 psu) and at Pauillac (R=0.8, RMSE=0.56 psu) as stated in Figure 3. 2d.

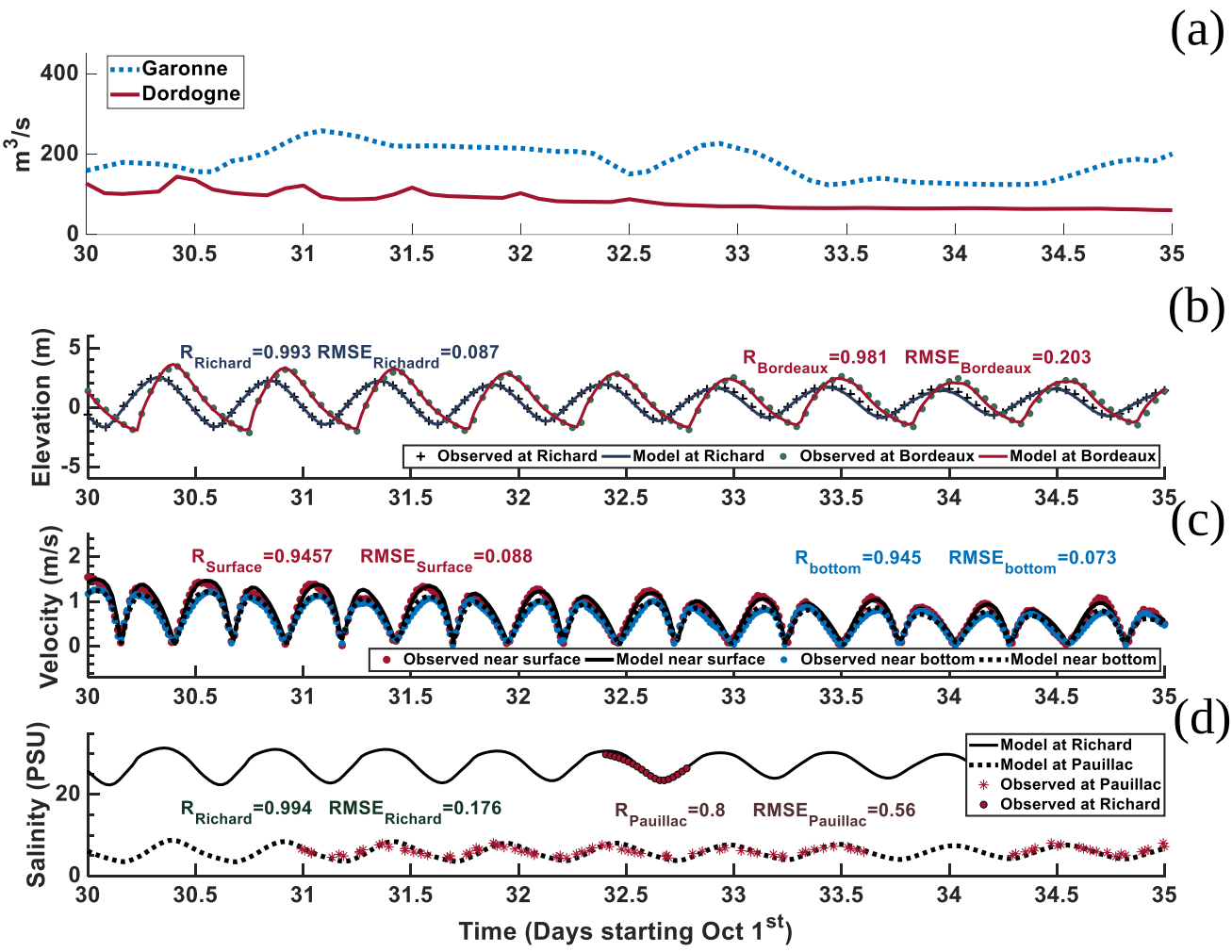

Figure 3. 2. (a) The discharge values for Garonne and Dordogne during the validation period (35 days) starting Oct 1st (b) The measured free surface elevation at Richard (+) and Bordeaux (●) along with the numerical outcome at the same locations (solid blue for Richard and solid red for Bordeaux). (c) the measured velocity near the bottom (●) and near the surface (●) at the ADCP location with the corresponding numerical velocity (dashed line for the bottom velocity and solid line the surface velocity). (d) the salinity near the mouth (●) and near Pauillac (✳) stations and the predicted salinity (solid black for the mouth station and dashed black for the Pauillac station). The R-square value (R) and the Root Mean Square Error (RMSE) is reported for all the model data shown in the figure.

3.1.3.3 Numerical Experiments

To investigate the temporal and spatial variation of the residual flows in the Gironde estuary, two types of simulations were conducted: one for a homogeneous (barotropic) and one for a non-homogeneous (including density gradients) system. A total of four simulations, summarized in Table 3. 1, were performed using the validated Gironde model to explore the along channel residual flow structure and drivers along the estuary under different tidal condition (spring and neap tides) and during dry and wet seasons (low and high river discharge). Two complementary experiments (5 and 6 in Table 1) were performed to survey the influence of the advective terms on the residual flows' magnitude and structure. In both of these latter experiments, the advective terms in the momentum equations are suppressed while the advective terms in the salinity balance are active. Different than in the validation, the experiments are done with a fixed discharge. According to the river discharge data provided in 2015, the mean river discharge during the dry season (June to October) was 300 m^3/s and during the wet season (February to April) was 900 m^3/s (not shown). These values were adopted in the model to exemplify the seasonal variation in the Gironde. A constant salinity value (35 psu, ocean salinity) is imposed at the ocean boundary and wind is not taken into account in the experiments. For each case presented in Table 1 a model simulation of the Gironde hydrodynamics was run for 45 days (physical time), 30 days for spin-up and 15 days for data analysis, allowing for several spring-neap cycles to be captured. The actual tidal conditions were imposed to produce results (i.e. simulated residual flows) that most closely align with actual residual flows in Gironde.

A harmonic analysis considering the semi-diurnal (~12.42 h), quarter-diurnal (~6.21 h) and sixth-diurnal (~4.14 h) tidal species was performed over the entire domain to extract the residual

flow (as well as residual salinity and the terms in the Eq. 3. 1) during spring (after 30 of the simulation period) and neap (after 38 of the simulation period) conditions over one full semi-diurnal tidal cycle (~12.42 h) as follows by least-squares fitting of the relation (R. Cheng & Gartner, 1985; Foreman & Henry, 1989),

$$U = \overline{U} + \sum_{i=1}^{M} A_i \times \cos\left(\omega_i t - \phi\right) \qquad 3.5$$

where $\boldsymbol{U}$ is the intratidal flow (residual + tide), $\boldsymbol{A}$, ω, and φ are the amplitude, frequency and phase of the tidal constituent $\boldsymbol{i}$ of $\boldsymbol{M}$ number of constituents (in this article $\boldsymbol{M}$=3). $\overline{\boldsymbol{U}}$ in Eq. 3. 5 represents the residual flow (here and through the paper). Also, in this work, residual flows and residual circulation are treated as synonymous. All averaging (calculating $\overline{\boldsymbol{U}}$ or any quantity using Eq. 3. 5) is performed in a sigma-layer coordinate system to ensure the presence of water throughout the tidal cycle as suggested by Kjerfve (1975). This implies that the averaged quantity (e.g. $\overline{\boldsymbol{U}}$) at each node ($\mathbf{x}, \mathbf{y}$ and $\mathbf{z}'$: variable vertical location with time) in the vertical plane is assigned to the tidally averaged vertical location of that node ($\mathbf{x}, \mathbf{y}$ and $\overline{\mathbf{Z}}$: tidally averaged vertical location). As a result of using the this method, the residual flow over a cross section (net discharge) may deviate from river discharge as demonstrated by Klingbeil et al (2019). An alternative method such as thickness-weighted averaging (Klingbeil et al., 2019) may be adopted to reduce this error. For each run, the harmonic analysis is performed after at least 30 days of simulation to make sure that the model is adjusted (spun up) to the river discharge.

After the least squares fit, the residual flow obtained from the homogenous case (barotropic) was subtracted from the residual flow obtained from the non-homogeneous case

(total: barotropic + density-driven flow) to extract the density-driven flow. The term "barotropic" will be used for the homogenous simulations and the term "total" will be used for the non-homogeneous simulations. The results of these simulations (1-4 in Table 3. 1) are presented in the next section.

Table 3. 1. The configuration for each numerical experiment carried out. Each case simulates the Gironde hydrodynamics for 45 days to capture the spring-neap variation. The highlighted cases (5 & 6) are the complementary simulations

Run	Density	Advection	River Discharge m^3/s
1	Homogenous (barotropic)	ON	300 (low)
2	Non-Homogenous (total)	ON	300 (low)
3	Homogenous (barotropic)	ON	900 (high)
4	Non-Homogenous (total)	ON	900 (high)
5	Homogenous (barotropic)	OFF	900 (high)
6	Non-Homogenous (total)	OFF	900 (high)

3.1.4 Results

This section presents the results obtained from the first four numerical simulations (runs 1–4) described in Table 3. 1. For each case, the residual flows are evaluated during the maximum spring tide (tidal range = 4.8 m) and the minimum neap tide (tidal range = 2.0 m) from the 45-day simulation. The neap and spring results are presented for both low and high river discharge.

3.1.4.1 Low River Discharge

The results of residual salinity, along-channel velocity, and the along-channel momentum balance for neap-spring tidal conditions during low river discharge case (run 1 and 2 in Table 1) are presented under this sub-section.

3.1.4.1.1 Salinity

The depth-averaged and depth-dependent residual salinity field along the navigation channel are found to be similar during both neap and spring tide during low river discharge (Figure 3. 3). The isohalines along the channel (Figure 3. 3c and Figure 3. 3d) indicate a well-mixed water column (no stratification) similar to Allen (1973) and Prieur et al. (1987), which are the most comprehensive studies of the along-channel salinity distribution in the Gironde to date. This salinity pattern is indicative of mixing dominating over the buoyancy from river input. The lateral residual salinity gradient is relatively low compared to the along channel salinity gradient, with the most pronounced variation near the mouth during spring tide (Figure 3. 3b).

3.1.4.1.2 Along Channel Residual and Density Driven Flow.

During neap tide the total along-channel residual flow magnitude (absolute value of the flow averaged over the cross section) varies from 0.07 m/s to 0.2 m/s near the mouth (S1 section) and 0.02 m/s to 0.1 m/s at S8 (46 km) as reported in Figure 3. 4b. In this case, the along-channel residual flows are latterly sheared with inflow in the channel and outflow over the flanks especially from the mouth to mid-estuary (sections S1 to S5; Figure 3. 4b). The pattern of the barotropic along-channel residual flows (Figure 3. 4a) are qualitatively similar to that observed in the total flow (Figure 3. 4b).

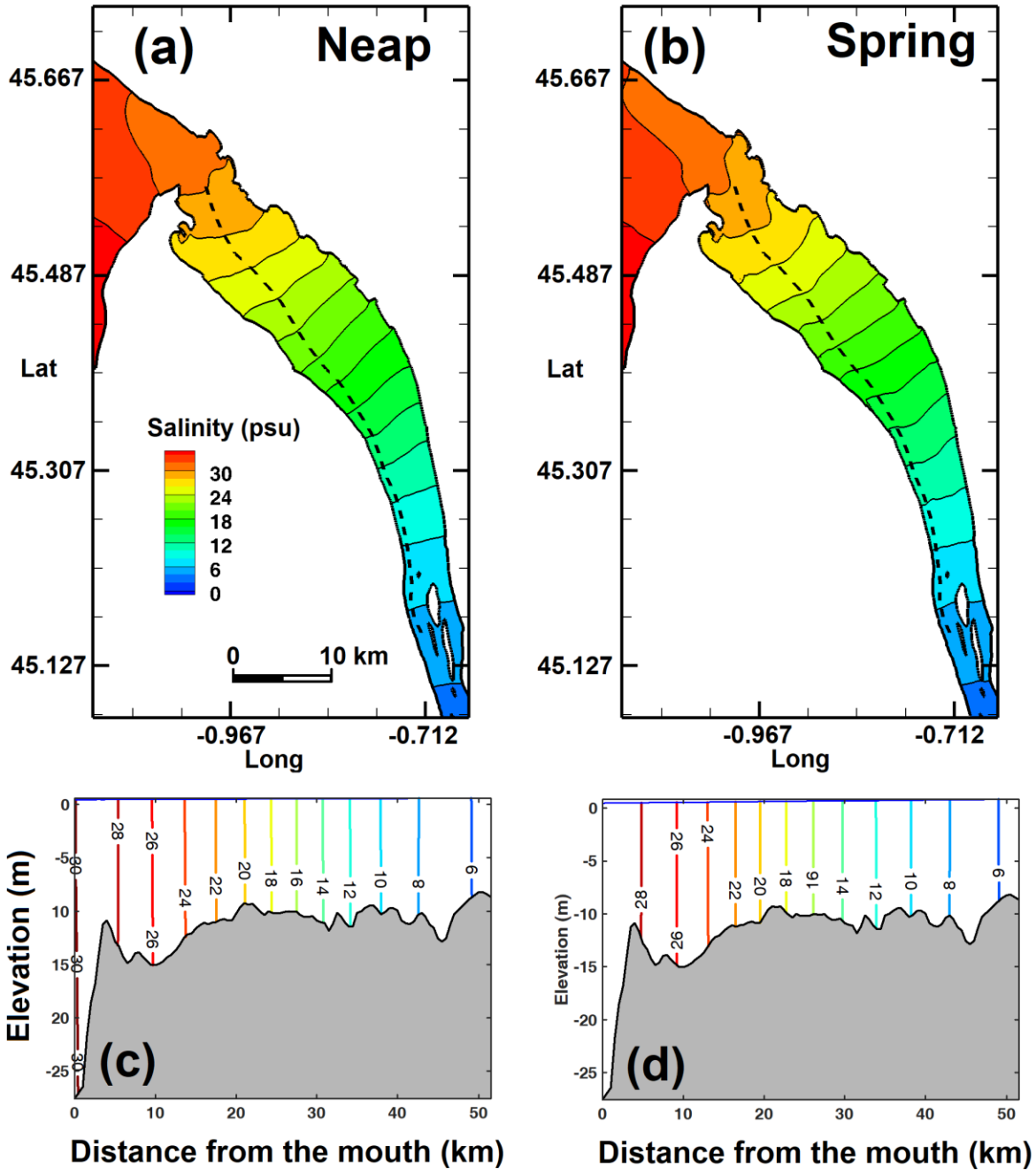

Figure 3. 3. The residual salinity field during neap and spring tides for low river discharge. The upper row details the depth-averaged salinity during neap (a) and during spring (b) tides. The lower row shows residual salinity distribution along the navigation channel depicted by the dashed line in (a) and (b) during neap (c) and spring (d).

The differences between the barotropic flow and the total flow (Figure 3. 4a, b) is mostly noticed in sections S2 to S5, where the barotropic residual flow pattern is slightly altered in the total flow case favoring the classical estuarine circulation structure (inflow in the channel and outflow over the shoals). The outflow in the channel in sections S4 and S5 in the barotropic case is reversed to inflow in the total flow case. This is attributed to the presence of the density gradient in the total flow case, as the density-driven flow is laterally sheared near the mouth with inflow in the channel and outflow over the shoals (Figure 3. 4c). This is due to the baroclinic pressure gradient becoming relevant in the deeper channel sections compared to the barotropic pressure gradient (not depth-dependent) creating a positive pressure gradient that drives the flow in-estuary. Conversely, the baroclinic pressure gradient is reduced at the shoals and the total pressure gradient becomes negative producing out-estuary flow (Valle-Levinson et al., 2003). As the across channel bottom profile becomes less complex (less lateral variability in the bottom depth) toward the head of the estuary, the density-driven flow becomes more vertically sheared (Figure 3. 4c, S4 to S8). Residual flows are engendered from the balance (competition) of at least two forces (e.g. the terms in Eq. 3. 1). Reporting the magnitude of these forces allows to identify which forces lead this balance and where the leading forces change along the estuary. Following the method of Lerczak and Geyer (2004) the absolute value of the area average of each term in Eq. 3. 1 was quantified for the total flow system as reported in Figure 3. 4. Since wind stress is not included, the stress divergence in this case arises from the bottom friction. Thus, integrating the stress divergence over depth, represents the bed stress. At the mouth (S1, 0 km), lateral advective accelerations (~4×10^{-5} m/s^2) dominate over the barotropic (~3×10^{-5} m/s^2) and baroclinic (~2.5×10^{-5} m/s^2) pressure gradients and stress divergence (~2.5×10^{-5} m/s^2).

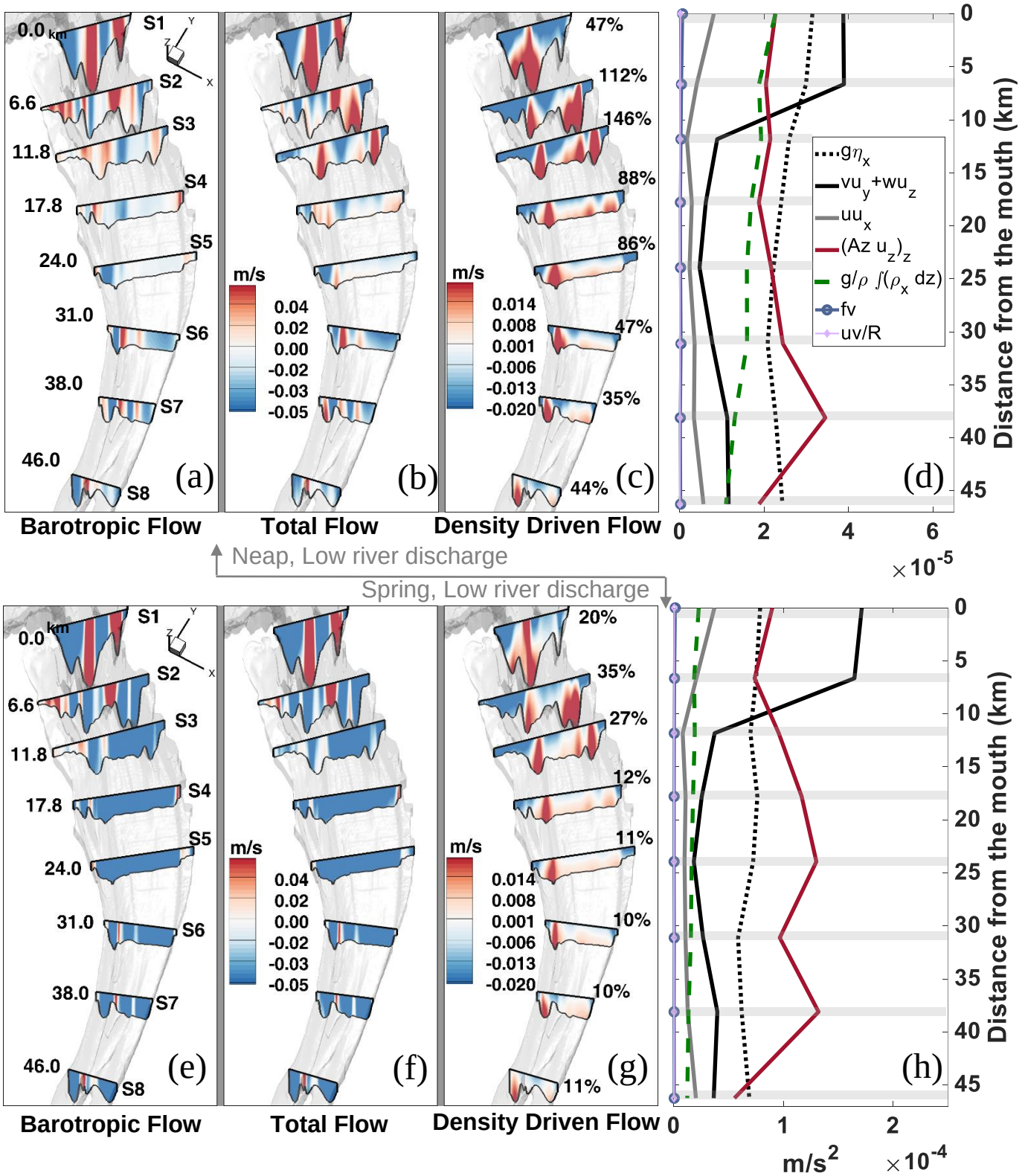

Figure 3. 4. Along-channel Residual flows and forcing mechanisms over a neap-spring cycle for low river discharge over eight transects (S1, 0km to S8 46 km from the mouth as detailed in (e)) along the system. The neap tide results are detailed in the upper panel where; (a) the barotropic residual flow, (b) total residual flows, (c) density-induced flow, and (d) the area and tidally averaged terms from equation 1 (barotropic pressure gradient $[g\eta_x]$ baroclinic pressure gradient $[\frac{g}{\rho}\int \rho_x dz]$, lateral advection $[vu_y + wu_z]$, longitudinal advection $[uu_x]$, stress divergence $[(Az\ u_z)_z]$, Coriolis (fv) and curvature $[\frac{vu}{R}]$. The spring results are detailed in the lower panel; (e) the barotropic residual flows, (f) the total residual flows, (g), density induced flow, and (h) is the area and tidally average of the terms in equation 1 (similar to (d)).

The longitudinal advective acceleration is an order of magnitude less than the lateral advection, similar to that found by Lerczak and Geyer (2004). At S3, 11 km from the mouth, the lateral advection is significantly reduced and reaches its minimum (~0.5×10^{-5} m/s^2) at S5, 24 km from the mouth. At this point, the stress-divergence and the pressure-gradient terms dominate. The lateral advection increases (~1×10^{-5} m/s^2) in the up-estuary direction (S6 to S8) as the channel s narrows and the lateral variability in the bathymetry is becomes more complex. Up-estuary, the barotropic pressure gradient and stress divergence (~2×10^{-5} m/s^2) dominate the flow and both are twice as high as the baroclinic pressure gradient and lateral advection.

During spring tide (Figure 3. 4 e-h), the residual flow magnitude is twice as large as that found during neap tide (Figure 3. 4 a-c). Compared to the residual flow pattern during neap (Figure 3. 4 a-b), the barotropic and total along-channel flow patterns shows less lateral variability, indicating more unidirectional along-channel residual flows. The contribution of density-driven flow to the estuarine residual flows during spring tide (Figure 3. 4g) is significantly less (four to five times less) than its contribution during neap tide as (Figure 3. 4c), yet the structure is similar. During neap tide (spring), density-driven flow is responsible for between 35% (10%) and 146% (35%) of the residual flows with the relative contribution varying along-estuary. During neap, the relative contribution peaks at S3 (146%), 11 km from the mouth, and declines toward the head. The contribution at S8 (45 km from the mouth) is 25% higher than at S7 (38 km from the mouth). This can be attributed to the increase in stress divergence relative to the baroclinic pressure gradient at S7 compared to that at S8 as shown in Figure 3. 4d. The contribution of density-driven flow during spring tide is less important compared to neap, even at its peak contribution (35% at S2, 5 km from the mouth). In terms of the forcing mechanisms

during spring tide(Figure 3. 4h), the advective accelerations, barotropic pressure gradient and stress divergence are an order of magnitude stronger than the baroclinic pressure gradient (Figure 3. 4c). In fact, the baroclinic pressure gradient shows no differences in its magnitude during spring tide compared to neap. This is because that the salinity structure does not vary significantly during neap-spring cycle (see Figure 3. 3).

The dominant forces during spring tide are the barotropic pressure gradient and stress divergence inside the estuary and lateral advection near the mouth. Similar to neap tide, the longitudinal advection, Coriolis and curvature are considered negligible. The density gradient extends further upstream S8 during neap and spring conditions. Therefore, gravitational circulation (the classical estuarine circulation) may be present further upstream. However, the influence of river discharge is more dominant in the upstream sections and this study focuses on the main body of the estuary.

3.1.4.1.3 Transverse Structure of the Forcing Mechanisms

During both spring and neap tide, the along-channel residual flows show complex lateral structure (significant lateral variability), especially near the estuary mouth, due to the complex variation in the depth across the channel at this transect. In fact, the bathymetry at the mouth is generally triangular shaped (S1) with one main navigation channel and two secondary channels on each side. Compared to the mouth (S1, Figure 3. 5 a-c), the cross-channel bathymetry mid-estuary (S4-S6), is almost rectangular (Figures 3. 4 and 3. 5).

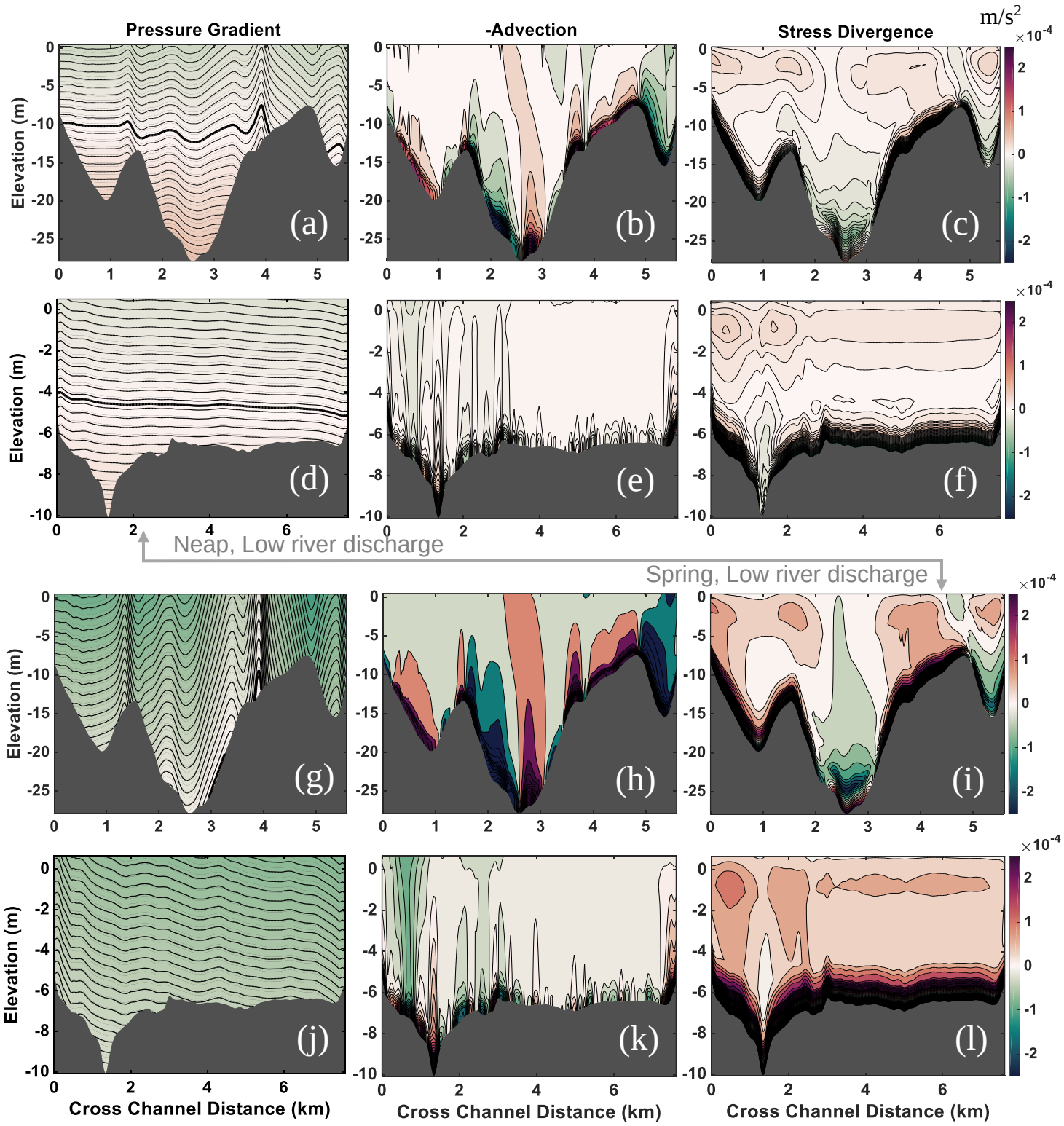

Figure 3. 5. Contours of residual forcing mechanisms for low river discharge during neap (first two rows) and during spring tides (second two rows) at the mouth (S1) and at mid-reach (S5, 24 km upstream of S1) transects. (a) pressure gradient (barotropic+baroclinic), (b) advection and (c) stress divergence at S1 at spring. (d) pressure gradient, (e) advection, and (f) stress divergence at S5 at neaps. (g) pressure gradient, (h) advection and (i) stress divergence at S1 at springs. (j) pressure gradient, (k) advection and (l) stress divergence at S5 at neaps. Positive contours (red) augment the landward flow, negative contour (green) augment the seaward flow and perspective is seaward.

Due to the significant change in the estuarine bathymetry from the mouth to the mid-reach the transverse structure and the magnitude of the dominant drivers of residual flows (i.e. pressure gradient, advection and stress divergence) are modulated. Note that lateral and longitudinal advection in Eq. 3. 1 were combined when investigating the lateral structure of the forcing mechanisms since they are on the same order of magnitude inside the estuary. The baroclinic and the barotropic pressure gradients were also combined. At both the mouth section (S1) and mid-estuary section (S5) during neap tide, the structure of the total residual flows does not follow the structure of the pressure gradient (vertically sheared structure, Figure 3. 5a and d). The residual stress divergence in this case (Figure 3. 5 c and f) at both sections (S1 and S5) counteracts the residual pressure gradient. The residual advection showed a complex transverse structure (Figure 3. 5b and e). At the mouth section the residual advective accelerations augments the pressure gradient at depth and counteracting it at the surface on the right side of channel (2.5-3 km from the left side of the channel) On the left side of the channel (2-2.5 km from the left side of the channel), the advective acceleration counteracts the pressure gradients. At the mid-estuary section (Figure 3. 5e), the residual advective acceleration is an order of magnitude less than it is at the mouth section (Figure 3. 5b) and, in general, it augments the pressure gradients. The transverse structure of the advective acceleration is preserved during the spring-neap cycle (Figure 3. 5b and h). The residual pressure gradients, if they were the only forces acting on the flow, during spring tide (Figure 3. 5g and j) drives the flow out-estuary over the entire cross section at the mouth and mid-estuary sections, in contrast to the pattern observed during neap tide. This is attributed to the fact that the barotropic pressure gradient

stronger than the baroclinic pressure gradient so that the landward forcing induced by the baroclinic pressure gradient is overwhelmed by the seaward barotropic force.

The stress divergence at the mouth in this case (Figure 3. 5i) augments the pressure gradients force in the channel and counteracts them on the shoals. This study focuses on quantifying the forcing mechanisms of residual flows in a system with both barotropic and baroclinic pressure gradients included. The spatial structure of the forcing mechanisms is considered with both pressure gradients included. The spatial structure of the forcing mechanisms, and in particular the stress divergence term, considered in the barotropic case will most certainly show a different structure than that of the baroclinic runs.

3.1.4.2 High River Discharge

The increase of the rivers input (Run 3 and 4 in Table 3. 1) affects the salinity (density) gradient and, as such, can alter the magnitude and structure of the residual flows observed during a low river discharge condition as will be demonstrated in the proceeding sub-sections.

3.1.4.2.1 Salinity

The along-channel salinity gradient and the salinity intrusion length vary over the fortnightly cycle, with the salinity intrusion slightly longer (~3 km) during spring tide (Figure 3. 6b) and more lateral variations present in the salinity field during neap tide (Figure 3. 6a). In terms of vertical salinity structure, the isohalines are more strained during neap than spring tide (Figure 3. 6c and d), as expected due to the decrease in tidal mixing during spring, making the system partially mixed. Compared with the low river discharge (300 m^3/s) case (Figure 3. 3), the increased freshwater input (900 m^3/s) in the system drives the salinity field down-estuary decreasing the

salt intrusion limit by 35 km compared to low river discharge in Figure 3. 3. The along channel salinity gradient, on the other hand, is intensified with the increased river input to ~1 psu/km where it was ~0.5 psu/km during low river discharge.

3.1.4.2.2 The Residual and Density-Driven Flow

In a barotropic system, the increased river discharge enhances the residual outflow (reduces the inflow) by 3% (Figure 3. 7a and e) compared to the low river discharge case. The impact of increasing the freshwater input is more apparent during neap in the total flow case (Figure 3. 7b) than spring (Figure 3. 7f). During neap, the baroclinic pressure gradient (tidally and area-averaged) is as important as the barotropic pressure gradient and stress divergence (~$3 \times 10^{-5}\ \mathrm{m/s^2}$). The magnitude of the baroclinic pressure gradient compares to the magnitude of the barotropic pressure gradient, stress divergence and advection near the mouth (S1, 0 km and S2, 6 km upstream) during high river discharge and neap condition (Figure 3. 7d).

Lateral advection is also relevant near the mouth (~$3 \times 10^{-5}\ \mathrm{m/s^2}$) and it is always greater than the longitudinal advection (~$0.5 \times 10^{-5}\ \mathrm{m/s^2}$). In the upstream sections (S6, 31 km upstream, to S8, 45 km upstream) the density-driven flow diminishes (mean flow magnitude = 0.001 m/s) as reported in Figure 3. 7c. This can be ascribed to the baroclinic pressure gradient as its magnitude is reduced upstream (Figure 3. 7d). During spring tide, the transverse structure of the barotropic (Figure 3. 7e) and the total (Figure 3. 7f) residual flow is predominantly out-estuary from S3 (12 km upstream) to S8 (45 km upstream) except near the mouth (S1 and S2) where the flow structure is laterally sheared.

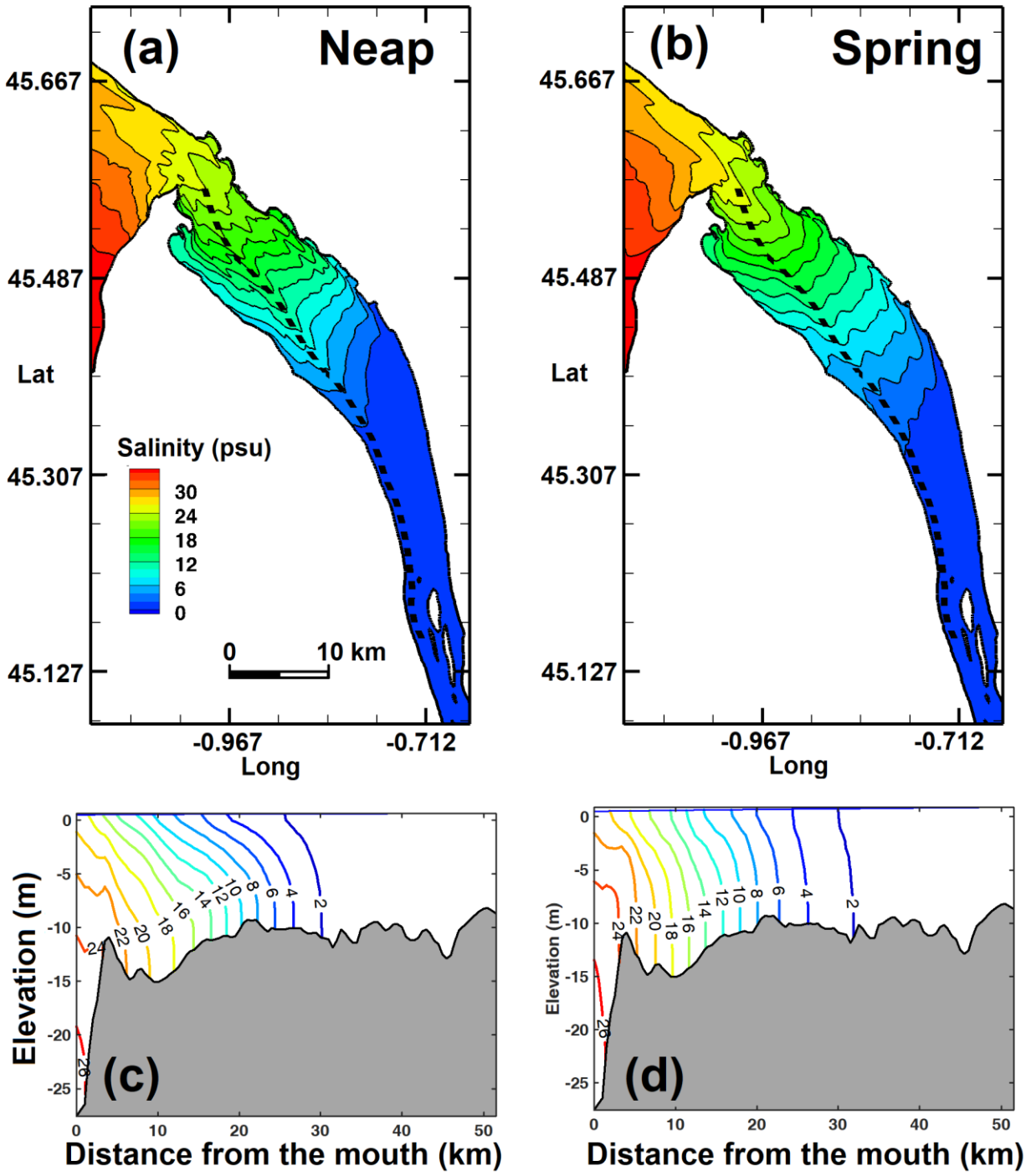

Figure 3. 6. Residual salinity field during neap and spring tides for high river discharge. The upper row details the depth-averaged salinity during neap (a) and during spring (b) tides. The lower row shows residual salinity distribution along the navigation channel (depicted by the dashed line in (a) and (b)) during neap (c) and spring (d).

The magnitude and the structure of the density-driven flow in this case is comparable to the density-driven flow observed during neap tide. The contribution of density-driven flow to the estuarine residual flows, nonetheless, is three times higher during neap than during spring as reported in Figure 3. 7c and g respectively. During neap tide the contribution of density-driven flow to estuarine residual flows increases from the mouth (S1, 74%) to 12 km upstream (S3, 212 %). This contribution then dramatically decreases, becoming negligible (~0%) upstream due to the absence of the density gradient (Figure 3. 7d). The density-induced flow contribution during spring tide is at a maximum at sections S2 (51%) and S3 (43%). Relative to the baroclinic pressure gradient, advective accelerations, stress divergence and the barotropic pressure gradient are an order of magnitude greater during spring (Figure 3. 7h) than during neap (Figure 3. 7d).

3.1.4.2.3 Transverse Structure of the Forcing Mechanisms

The residual stress divergence in this case counteracts the pressure gradient at both sections (Figure 3. 8c and f), and its magnitude is comparable at the mouth and at the mid-estuary sections. Although the pattern of the residual advective acceleration is comparatively more complex (more lateral variability), several significant features emerge. This pattern is reversed in the left side of the channel (1.5 to 2.5 km from the left shoal). Mid-estuary section (Figure 3. 8e), the magnitude of the residual advection is notably reduced (four times less compared to the mouth) compared to pressure gradients and stress divergence. In general, advection at the mid-estuary section augments the pressure gradient.

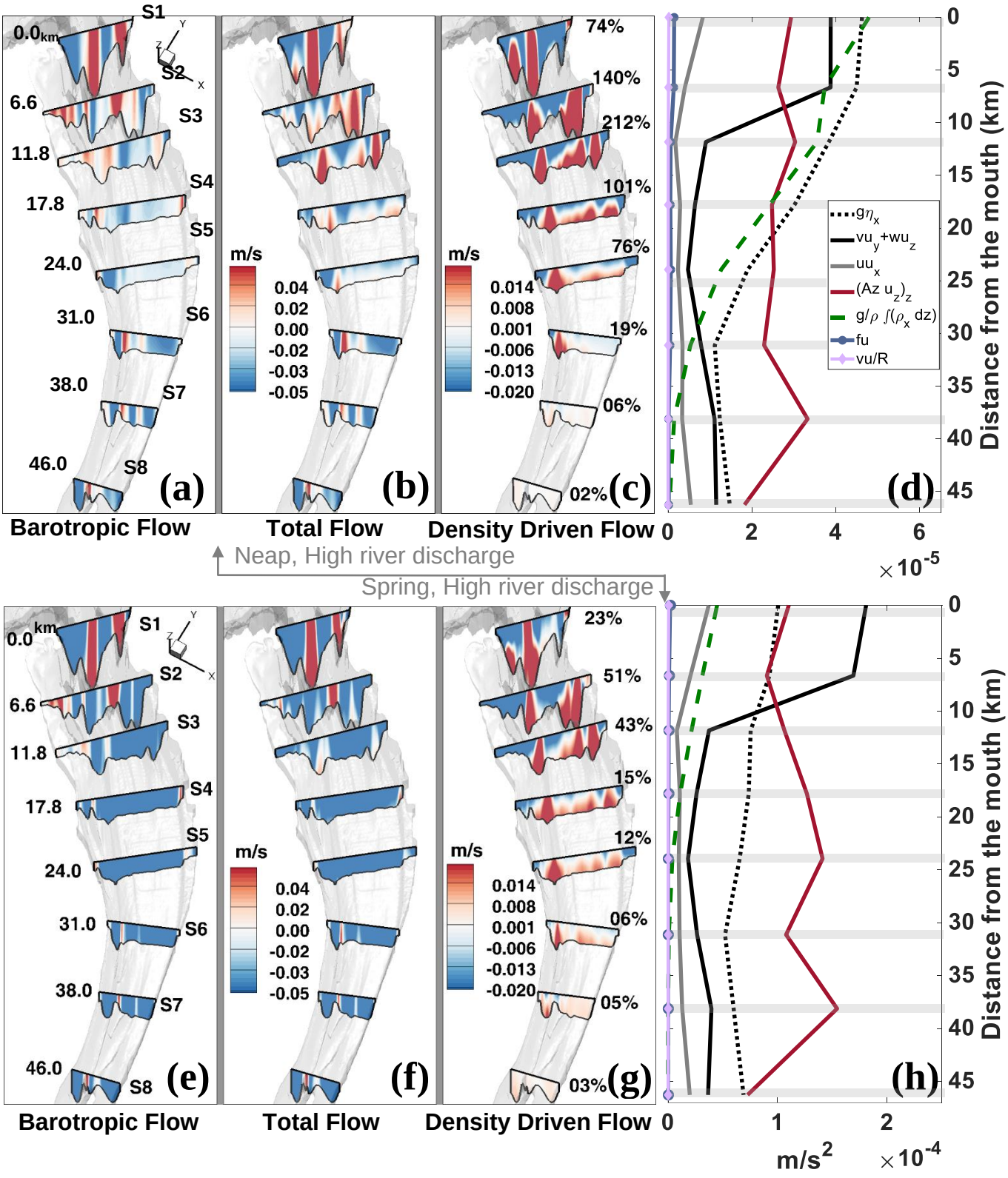

Figure 3. 7. Along-channel residual flows and forcing mechanisms over a neap-spring cycle for high river discharge over eight transects (S1, 0km to S8 46 km from the mouth as detailed in (e)) along the system. The neap tide results are detailed in the upper panel where; (a) the barotropic residual flow, (b) total residual flows, (c) density-induced flow, and (d) the area and tidally averaged terms from equation 1 (barotropic pressure gradient $[g\eta_x]$ baroclinic pressure gradient $[\frac{g}{\rho}\int \rho_x dz]$, lateral advection $[vu_y + wu_z]$, longitudinal advection $[uu_x]$, stress divergence $[(Az\, u_z)_z]$, Coriolis (fv) and curvature $[\frac{vu}{R}]$. The spring results are detailed in the lower panel; (e) the barotropic residual flows, (f) the total residual flows, (g), density induced flow, and (h) is the area and tidally average of the terms in equation 1 (similar to (d)).

During spring, the positive component (near bottom) of the residual pressure gradient at the mouth (Figure 3. 8g) is reduced compared to that observed during neap tide (Figure 3. 8a). This is due to the increase of the barotropic pressure gradient during spring (twice as strong as neap tide Figure 3. 7d and h) which results in a negative forcing. Mid-estuary, however, the baroclinic pressure gradient is overshadowed by the barotropic pressure gradient which drive the flow out-estuary over the entire cross section (Figure 3. 8j) if it was the only forcing in the system. The residual stress divergence, in general, counteracts the pressure gradient at both sections (Figure 3. 8i and l). The pattern (complex lateral variability) of the residual advection (Figure 3. 8h and k) is preserved during the spring-neap cycle. As shown in this section, the density-driven flow is most relevant to the total estuarine residual flow during neap tide during the high river discharge. The contribution of density-driven flow is reduced during spring tide due to the significant increase of the advective acceleration, stress divergence and barotropic pressure gradient relative to baroclinic pressure gradient. The results suggest at estuarine cross-sections when the contribution of density-driven flow to the total residual flows is significant ($\xi \geq 75\%$) (see Figure 3. 4c, g and Figure 3. 7c, g), the typical estuarine circulation is observed, which is inflow in the channel and outflow over the shoals. Nevertheless, this pattern is observed near the mouth for the barotropic and the baroclinic cases raising the question of what promotes this pattern besides the baroclinic pressure gradient?

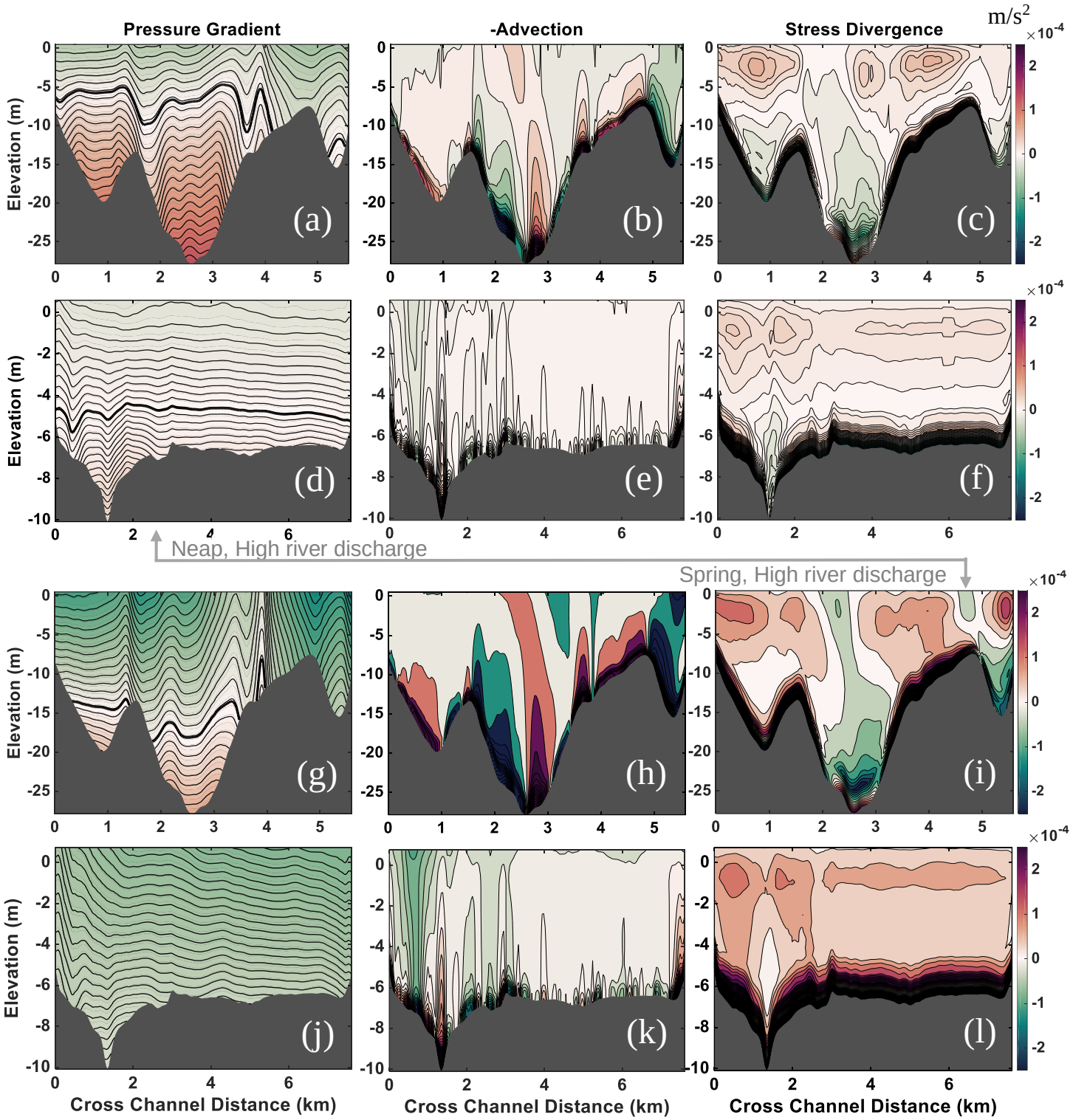

Figure 3. 8. Contours of residual forcing mechanisms for high river discharge during neap (first two rows) and duirng spring (second two rows) at the mouth (S1) and at mid-reach (S5, 24 km upstream of S1) transects. (a) pressure gradient (barotropic+baroclinic) (b), advection, and (c) stress divergence at S1 at neaps. (d) pressure gradient, (e) advection, and (f) stress divergence at S5 at neaps. (g) pressure gradient, (h) advection and (i) stress divergence at S1 at springs. (j) pressure gradient, (k) advection and (l) stress divergece at S5 at springs. Posative contours (red) augment the landward flow, negative contour (green) augment the seaward flow and peripective is seaward.

3.1.5 Discussion

This study aims to determine the along-channel structure of residual flows and their forcing mechanisms using a numerical model with realistic bathymetry in a macrotidal estuary and to determine the contribution of density-driven flow to the total estuarine circulation over various temporal scales. It was found that the along-channel residual flow structure at the mouth is laterally sheared in both the barotropic and baroclinic cases over all temporal scales, indicating that another forcing mechanism is producing a residual flow pattern similar to that of density-driven flow. Since advection is a dominat force near the mouth, it is suspected to be the mechanism responsible for this presistent residual flow structure. This section will, therefore, explore the role of advection and bathymetric variability in producing these flows.

3.1.5.1 The Role of Advection

The role of advection in modifying the along-channel variation of residual flows has been previously explored in many studies. It has been shown that in tidally energetic (Burchard et al., 2011) and weakly stratified (Cheng, 2014) estuaries, advection produces a flow structure that is landward in the channel and seaward over the flanks, augmenting the density-driven flow structure. This is due to the differential advection of salinity that creates a lateral baroclinic pressure gradient which, as a result, develops lateral circulation cells with patterns that depend on the tidal phase. Over a tidal cycle, the average of the along-channel flow results in a non-zero net flow that is landward in the channel and seaward over the shoals augmenting the classical estuarine circulation (Chant, 2010; W Rockwell Geyer & MacCready, 2014; MacCready & Geyer, 2009). In other studies based on the Chesapeake bay, both Huijts et al. (2009) and Zitman & Schuttelaars (2012) showed that advective accelerations induce a laterally sheared flow with a

complex structure. In all these studies, the role of advection was examined with the presence of the density gradient (salinity gradient).

In the Gironde, when considering a barotropic system (model runs 1 and 3 in Table 3. 1, spring and neap), the residual flow structure at the estuary mouth shows inflow in the channel and outflow over the shoals (Figure 3. 4a & e and Figure 3. 7a & e), the pattern is associated with density-influence, yet only tidal processes are present. This raises the question: Does advection manifest in a similar manner to deferential advection in the absence of a salinity gradient? To aid this presumption, the along and across channel velocity (intratidal and subtidal) obtained from the run 3, a barotropic system with advection on, run 5, a barotropic system with advection off, and run 6, a non-homogenous system with advection off (see Table 3. 1) during spring tide (when advection is most prevalent) are investigated.

When advection is on and during maximum ebb, a clockwise lateral circulation is developed over the channel (Figure 3. 9b) advecting the faster along-channel outflow near the surface over slower along-channel outflow at the shoals (Figure 3. 9a). In the same case during maximum flood (Figure 3. 9c and d), the lateral circulation is comparatively less complex, featuring two circulation cells with convergence at the surface over the channel and divergence at the bottom (Figure 3. 9d). This lateral flow pattern concentrates the velocity maximum in the channel (between 2-3 km in Figure 3. 9c). The tidal average of these patterns result in a net inflow in the channel and outflow over the shoals (Figure 3. 10a). Over a tidal cycle, the tidally averaged lateral flow (Figure 3. 10b, Advection on) shows a similar pattern to the lateral flow during flood tide: two counteracting circulation cells with convergence at the surface over the

channel and divergence at the bottom. This can be reasoned, similar to Lerczak & Geyer (2004), by the lateral flow during flood (Figure 3. 9c) being stronger than it is during ebb (Figure 3. 9b).

To verify that the intratidal lateral flow patterns, and thus the residual flow structure, are due to advection, a similar scenario was considered with advection turned 'off' in the model. These results show that during maximum ebb and flood tides, the maximum along-channel velocity is found over the thalweg (2-3 km) and in the secondary channels (0-1 km and 5-5.5 km, Figure 3. 9e and g). This is attributed to that fact that lateral advection has no impact in re-distributing the along-channel flow and, therefore, the flow will be faster over the deeper channel sections than it is over the shoals due to friction. Further, the lateral flow patterns during ebb and flood are indicative of a single-cell circulation attributed to the balance between the lateral pressure gradient and Coriolis (geostrophic balance, Figure 3. 9f and h). The net-lateral flow over a tidal cycle in the case with advection 'off' will be near zero (Figure 3. 10d). It is worth mentioning that the results during neap tide for the barotropic system (not shown) are qualitatively similar (in terms of residual flows) to the results in spring tide presented in this section. The lateral sheared along-channel residual flow induced by density driven flow (from run 6 in Table 3. 1, not shown) is augmented by the advective accelerations near the mouth. That is to say, the lateral structure of the residual flows near the mouth is induced solely by advection during spring and by the density gradient and advection during neap.

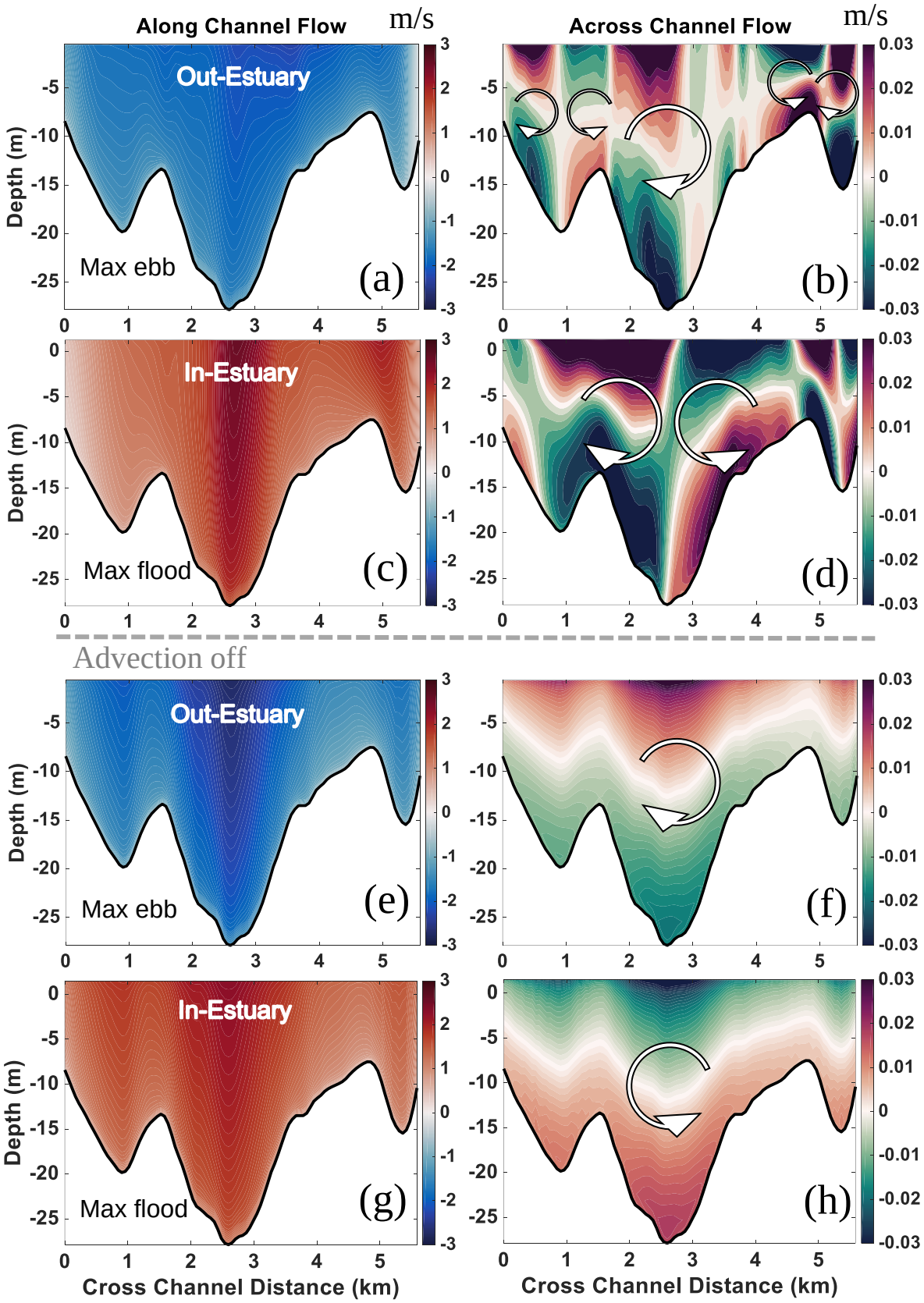

Figure 3. 9. Along and cross-channel flow at the estuary mouth (S1) during maximum ebb and flood tide for the barotropic and high river discharge cases, with advection on (the first two rows, run 3) and off (last two rows, run 5) as described in Table 1. (a) along-channel and (b) cross-channel flow during maximum ebb, and (c) along-channel and (d) cross-channel flow during maximum flood for run 3. (e) along-channel and (f) cross-channel flow during maximum ebb, and (g) along-channel and (h) cross-channel flow during maximum flood for run 5. Red (blue) color denotes inflow(outflow) for the along-channel velcoity. Red (green) color denotes a flow directed to the right (left) for the cross channel flow. Transect perspective is seaward.

3.1.5.2 The Impact of Estuarine Bathymetry

The variation of advection along the estuary (from dominant near the mouth to negligible upstream) is linked to the longitudinal variation in bathymetry. The convergence of the Gironde estuary (upstream reduction in width and depth) is a key feature germane to its topography. The width of the estuary decreases at a rate of 0.14 km/km (see Figure 3. 1b) and the cross-sectionally and tidally averaged depth decreases from 13.5 m to 6.5 m from the S1 to the S8.

Another key factor in the estuary topography is the constriction at the estuary mouth (5 km wide and 6 km long). Results suggest this topographic feature enhances advection (see Figure 3. 4d, h, and Figure 3. 7d, h). At the mouth section (S1), advection is of leading order in the along-channel momentum balance, and, as the estuary gets wider (11 km wide) and shallower after up-stream the constriction, advection decreases by one order of magnitude. This finding reiterates that in a channel with sloping sides, the relative importance of advection increases as the cross-section narrows and deepens (see Burchard et al., 2011; Scully et al., 2009; Lerczak & Geyer, 2004). In such channels, the time required for the flow to advect a water parcel is less than the time scale of vertical mixing (diffusion) to disperse the flow, thus the influence of lateral advection increases. In a wide and shallow channel, the flow needs more time to advect a water parcel than the time scale of diffusion, hence, advective acceleration becomes less significant. Within this context, the Gironde estuary is dynamically deep and narrow near the mouth and dynamically shallow elsewhere. In addition, the lateral variability in the channel depth at the mouth (S1) increases the lateral (u_y) and vertical (u_z) variability in the along channel velocity and as such the relative contribution of advection to the momentum balance (see Eq. 3. 1). To be brief, tidal flows interacting with lateral and longitudinal variability in bathymetry and channel

width near the mouth of the Gironde Estuary collectively enhance advective accelerations. In the mid-reaches of the estuary, when the channel width and bottom profiles become more uniform, the advective acceleration decrease. This implies that the longitudinal variations in bathymetry and width alter forcing mechanisms and thus the magnitude and structure of residual flows in this macrotidal estuary. Although, the baroclinic pressure gradient shows no correlation with the longitudinal variation in bathymetry (Figure 3. 4d, g and Figure 3. 7d, g), the latter affects the contribution of the density-driven flow to the estuarine circulation through affecting other terms (such as advection and mixing) making the density-driven flow contribution varies along the system. Studies on macrotidal estuaries such as Passamaquoddy Bay (Thompson et al., 2002) and Willapa bay (Banas & Hickey, 2005) suggest that the presence of complex morphologic features such as constrictions and islands could significantly affect exchange properties of these estuaries. Compared to Passamaquoddy and Willapa Bay, the Gironde estuary is considered less complex in terms of the number of constrictions, islands and the general shape (no branches), yet the impact of longitudinal variation of bathymetry prevails, specially near the mouth where the residual flows show a persistent lateral structure. Because the tide is strong in macrotidal estuaries, the abrupt axial change in bathymetry results in significant change in estuarine residual flows (magnitude and structure) due to advection.

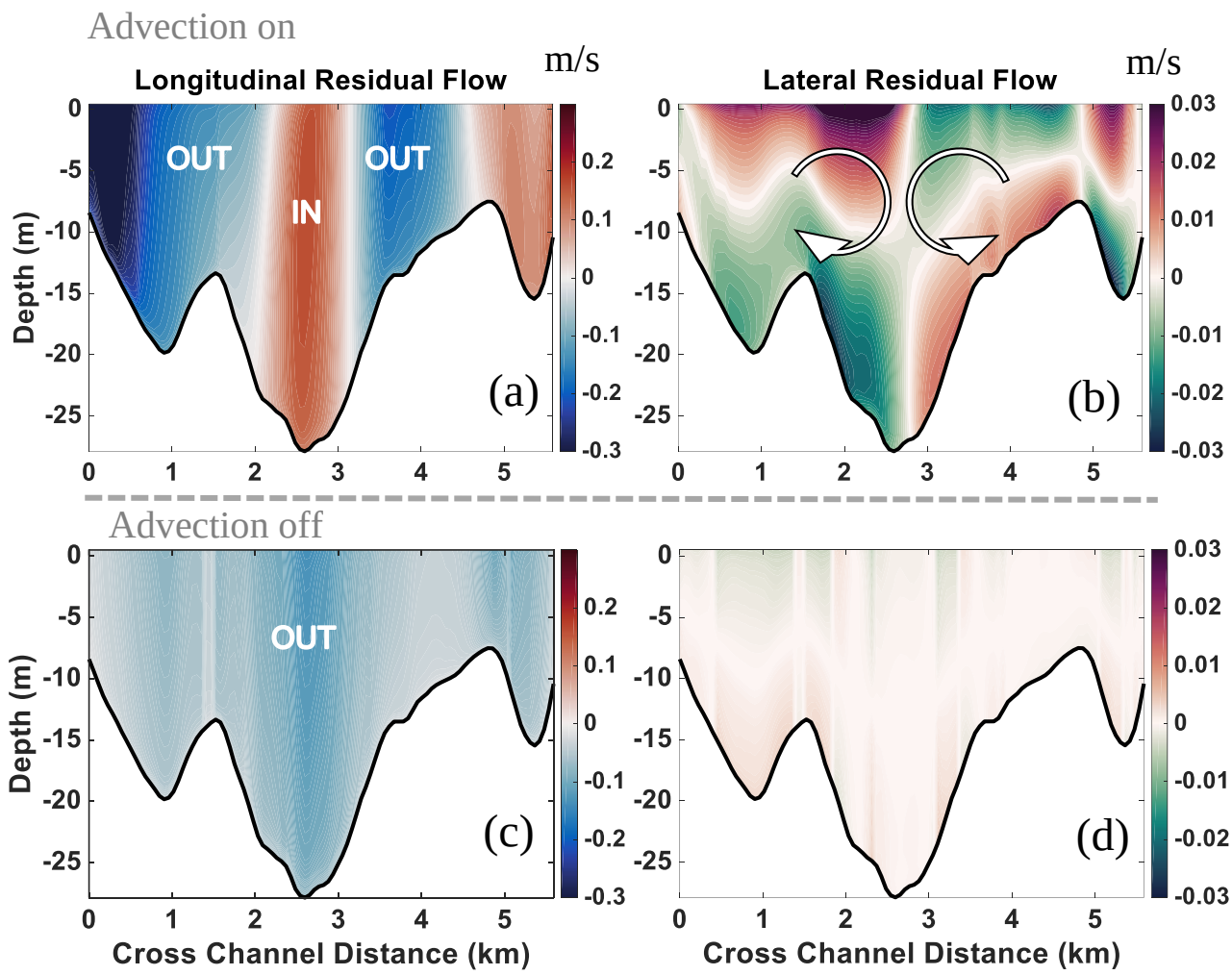

Figure 3. 10. The along and cross channel residual flows during spring tide and high river discharge when advection is on for (a) along channel flow and (b) cross channel flow, and when advection is off for (c) along channel flow and (d) cross channel flow. Red (blue) color denotes inflow(outflow) for the along-channel velcoity. Red (green) color denotes flow directed to the right (left) for the across channel flow. Transect perspective is seaward.

3.1.6 Conclusion

A three-dimensional numerical model was utilized to study the along-channel variation of residual flow structure and forcing mechanisms in a non-idealized macrotidal estuary. Results showed that the density-driven flow is a main driver of the total residual flows only during neap for both high and low river discharge conditions. In addition, even during neap tide, the contribution of density-driven flow to the total residual flow exhibits significant spatial variation from the mouth of the estuary to the head. In addition, the structure of the residual flows varied from the mouth to the head as a result of changing the relative importance of pressure gradient, advection and mixing as the bathymetry changes along the estuary. In fact, during neap tide and high river discharge, a combination of the baroclinic pressure gradient and advection dominated the tidally averaged along-channel momentum balance near the mouth of the estuary, producing a laterally sheared residual flow pattern that mimicked typical density-induced flow. This same residual flow pattern was found at the mouth during spring tide, yet was produced solely by advection, indicating that during certain tidal conditions (spring tide) advection-driven residual flows could be mistaken for density-driven residual flows, which has been the case in the Gironde estuary up to now.

CHAPTER 4

TRANSPORT TIMESCALES IN A MACROTIDAL ESTUARY

The relative importance of density gradients, river discharge, and advection on the Eulerian residual flow were identified along the Gironde estuary in the previous Chapter. This section underlines the effect of these mechanisms on the flushing and residence time of a tidally driven estuary.

4.1 Introduction

River discharge can be an important driver for the transport process in tidal estuaries (Castaing & Allen, 1981; John et al., 2020; Wan et al., 2013) as it contributes to the net residual circulation (Cheng, 2014; L. Guo et al., 2014; Huijts et al., 2009). Thus, river discharge may notably impact the water quality in estuaries (Azevedo et al., 2010). Haddout et al (2020), for example, investigated the impact of river discharge time in Bourgreg and Loukkos estuaries (macrotidal estuaries) using the freshwater fraction method. They found that the flushing time in the Bourgreg estuary reduced from 6.3 days to 2.7 days as the river discharge increased from 17 to 22 m^3/s, and from 3.4 days during neap tide to 2.7 days during spring tide, indicating that the influence of river discharge can overshadow that of fortnightly tidal variations even in macrotidal and convergent estuaries. When dividing the estuary into multiple segments, they also found that the flushing time of the upstream part of the estuary was shorter during neap tide than spring tide due to the enhanced density-driven circulation. However, the freshwater fraction method does not provide any information about the particle pathways in relation to the circulation in the estuary.

In addition to river discharge and the horizontal density gradients that it produces, tidal currents interacting with complex morphologic features can enhance residual flow drivers such as advection. This effect can be exacerbated in estuaries with strong tidal currents such as macrotidal estuaries (Alahmed et al., 2020). The residual circulation induced by the interactions of the river, density gradients, and estuarine bathymetry can be complex, yet ultimately affect how waterborne material is transported in estuaries. Yuan et al. (2007), in their study on Mersey Estuary, UK, found that the residence time dramatically varied spatially due to changes in the bathymetry. Mitra et al (2020) showed that in macrotidal estuaries, residence time can be increased due to the development of residual eddies that prevent particles from leaving the estuary.

Although studies have investigated residual circulation and transport timescales independently in tidal estuaries, the implications of residual circulation on transport timescales remain unclear. This is particularly true in tidally dominated estuaries where the barotropic tide can play a notable role in the transport process. The question then to which extent residual flow drivers, such as advection, river discharge, density gradients, and their interactions affect transport timescales and water quality in macrotidal estuaries? The aim of this study is to answer this question by investigating and linking spatial variations in residual flow structure and drivers to transport timescales in macrotidal estuaries. The goal will be met through the following research objectives: 1) Investigating the impact of advection, river discharge, and thus density gradients, on flushing times in a macrotidal estuary, and 2) Identifying if along-channel variations of residual circulation and drivers produce along-channel variations in transport timescales and if this varies on fortnightly or seasonal timescales. In order to address these objectives a case

study will be carried out in the macrotidal Gironde Estuary located on the southwest coast of France using a three-dimensional numerical model with Lagrangian particle tracking.

The remainder of this chapter will be as follows. Section 4.2 details the numerical model of the Gironde Estuary and model validation. Section 4.3 elaborates on the numerical experiments carried out in this work. The model flushing and residence time results for the numerical experiments are reported in Section 4.4. Section 4.5 discusses the major findings of this study and how it compares and contrasts with the transport timescale results found in chapter 2. Finally, the concluding remarks are made in Section 4.6.

4.2 Study Site

The Gironde estuary is a macrotidal estuary located on the Bay of Biscay in southwest France. The tide ranges from 1.5 m during neap to 5.5 m during spring near the estuary mouth (Castaing & Allen, 1981). The tidal effect in the Gironde (change in current and water level) can reach up to 150 km upstream during low river discharge (Cancino & Neves, 1999) while the salinity intrusion can extend 180 km upstream (Jalón-Rojas et al., 2015). The Garonne and Dordogne rivers drain into the Gironde with a mean combined discharge of 700 m^3/s. However, the instantons river discharge value can range from 200 m^3/s during dry season (June to October) to 3000 m^3/s during wet season (November to May) (Castaing & Allen, 1981). Studies on the Gironde showed that the river discharge is a major contributor to the transport of sediment in the system (Doxaran et al., 2009). The estuary can be classified as partially mixed to well-mixed as the vertical salinity gradient is small (Cancino & Neves, 1999). The Gironde estuary is funnel-shaped (convergent) with relatively simple morphology of the estuary is relatively

simple morphology featured with simple bed profile and few islands of different sizes (Figure 4. 1a). The width can vary between 12 km near the mouth to 1.5 km near the confluence of the rivers (85 km from the mouth). The tidally averaged flow in the upper estuary is primarily seaward (Alahmed et al., 2020; Cancino & Neves, 1999). Near the mouth, however, the residual flow pattern is more complex due to the complexity of the bathymetry therein (Alahmed et al., 2020). The average flushing time in the estuary is 20 days, however, it can reach up to 85 days during the dry season (Elbaz-Poulichet et al., 1984). Little effort has been, nonetheless, done to clearly study the flushing time in the Gironde and identify what drives the transport time scales and water quality in the system. This will be covered in the current work as will be presented in the following sections.

4.3 Numerical Model

Three-dimensional numerical simulations are used to track Lagrangian particles in the Gironde estuary using the TELEMAC3D finite element model (Figure 4. 1a). The model includes 20 terrine-following layers in the vertical plane and a non-uniform horizontal mesh that ranges from 15 km near the ocean to 20 m in the upstream rivers resulting in 21,242 nodes per vertical layer. This model domain was extended from that presented and validated in Alahmed et al. (2020) to include a larger ocean domain. The ocean boundary is forced by tidal water levels and velocities based on the TPXO9-atalas local solution (Egbert & Erofeeva, 2002). The river boundaries are forced by hourly measured river discharge obtained from the French water department (http://www.hydro.eaufrance.fr/). The measured river discharge values were used for the model validation process. Strickler's Law is used to evaluate the bottom friction and

Strickler's Coefficient was assigned based on the sediment type at the estuary bottom based on Allen (1973). Wind is not considered in the current model including the validation process.

The $\kappa - \varepsilon$ turbulence closure model was implemented as it has been found to be the most suitable for accurately capturing turbulence and mixing in estuarine environments (Celik & Rodi, 1985).

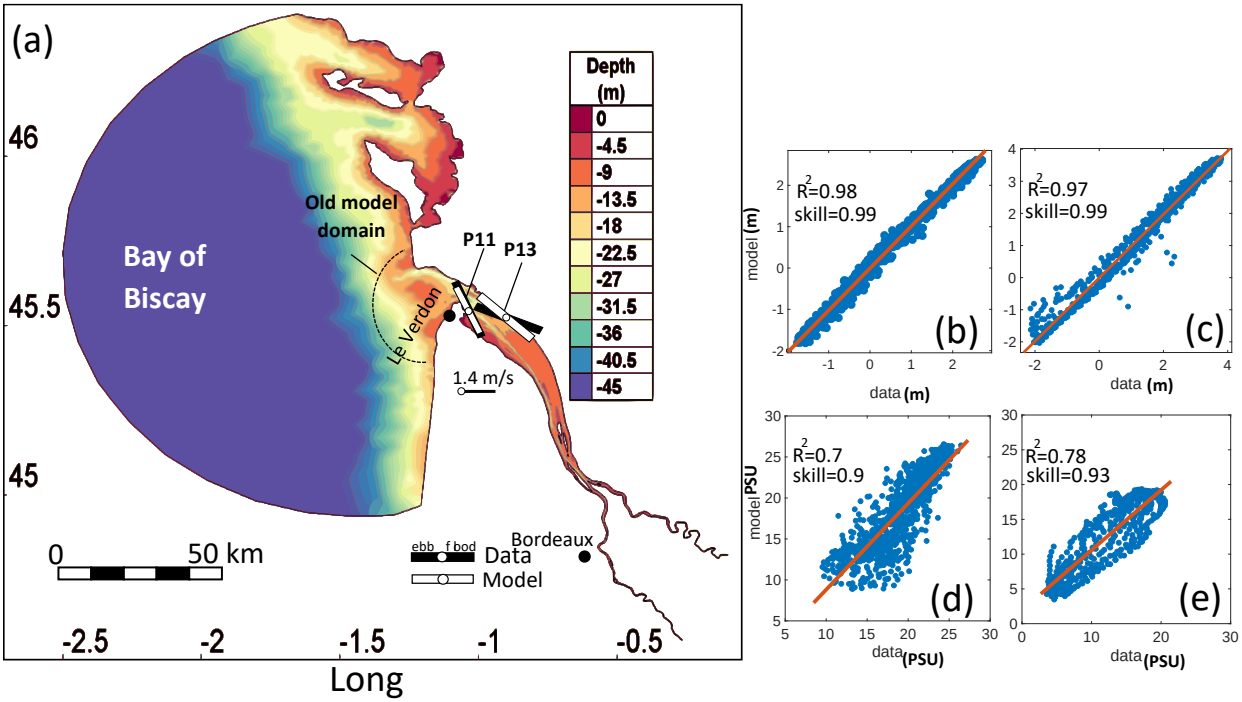

Figure 4. 1 (a) The model domain detailing the estuary and adjacent coastal shelf bathymetry. The bars denote the measured (black) and predicted (white) depth averaged velocity at locations P11 and P13. (b) and (c) The correlation between the measured (data) and predicted (model) water level at Le Verdon and Bordeaux respectively, (d) The correlation between the measured and predicted salinity near the surface at P11, and (e) The correlation between the measured and predicted salinity of the bottom at P11. The data presented were collected in March 2018.

The model was spun up for 6 months before validation and was validated against water level, velocity, and salinity collected at several locations along the estuary in 2018 (Figure 4. 1a-e). The correlation coefficient (R^2) and the predictive skill were both used as metrics to assess

the model validity. The skill values reported in Figure 4. 1 are close to 1 indicating that the model is suitable to carry out idealized scenarios to investigate particle transport.

4.4 Numerical Experiments

Conservative and passive Lagrangian particles were released over the model domain from the ocean into the estuary up to Labarde (near the confluence of the rivers, Figure 4.2a). The particles were released near the surface, mid-water column, and near the bottom as illustrated in Figure 4. 2b. The particles are evenly spaced in the horizontal plane with a resolution of 250 m

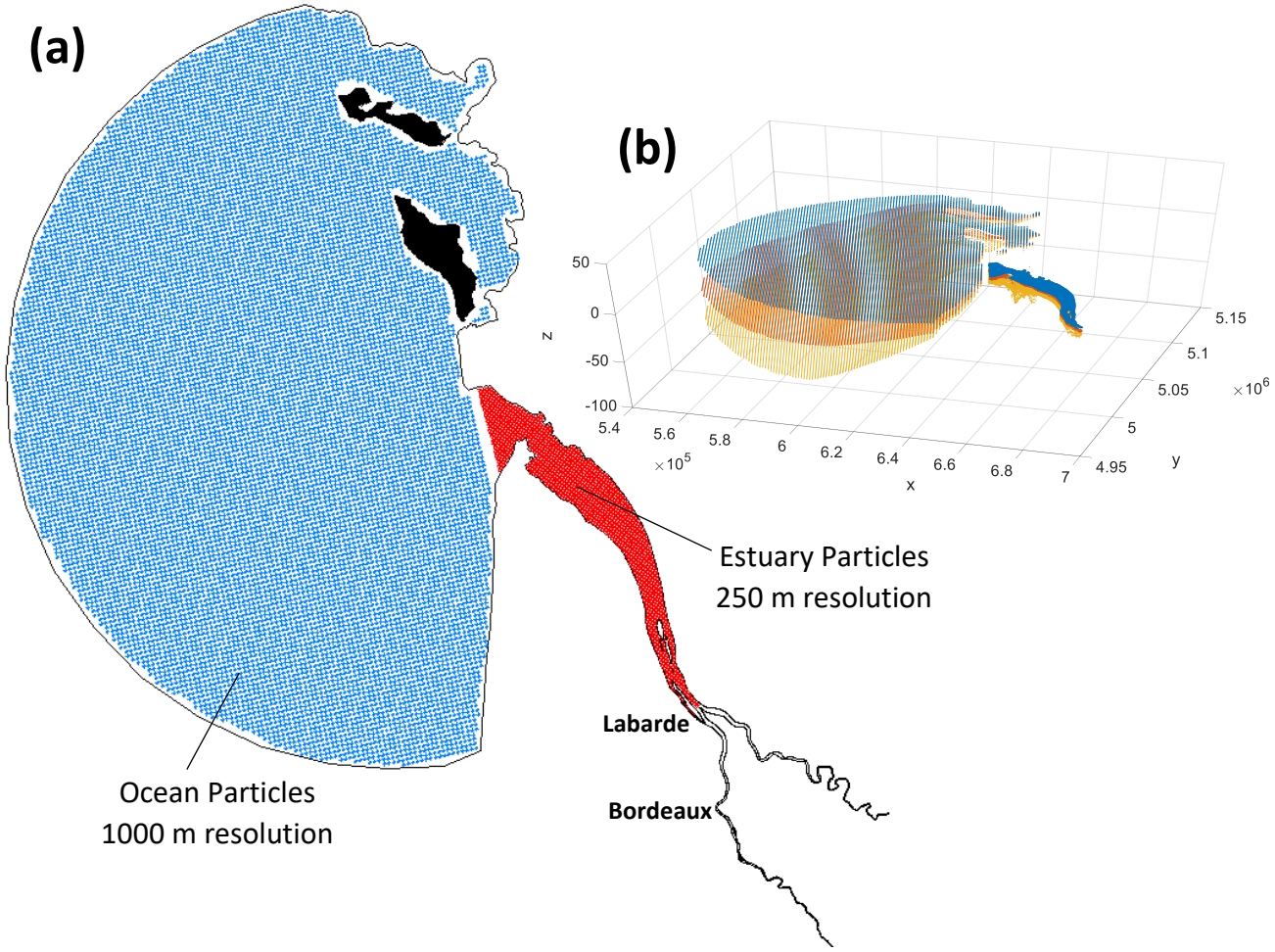

Figure 4. 2. (a) Lagrangian particles in the Gironde Estuary (red dots) and in the adjacent ocean (blue dots) in (b) Three-dimensional view of the particle placement in the model indicating particles at the surface (blue dots), mid water column (orange dots) and near the bottom (yellow dots).

in the estuary and 1000 m in the ocean (Figure 4. 2a), resulting in approximately 90,000 particles

placed and tracked during each simulation. Several numerical experiments were performed to understand the Lagrangian transport in the Gironde Estuary under varied forcing conditions and are detailed in Table 4. 1. Three cases were considered with varying tidal (neap vs spring release) and river discharge (seasonal variations) conditions including salinity and advection. Four additional cases were run to examine the effect of salt (density gradients) and advection on the transport timescales in an attempt to isolate dominant mechanisms. For each case in Table 4. 1, particles were released at slack before the ebb tide and were tracked for 40 days. The outcomes of the numerical experiments are presented in the following sections.

Table 4. 1. Overview of numerical scenarios run to examine transport timescales in the Gironde Estuary.

Case	Tidal Conditions	River Discharge High: 900 m^3/s Low: 300 m^3/s	Salinity	Advection	Coriolis
Realistic					
1	neap	low	on	on	on
2	neap	high	on	on	on
3	spring	low	on	on	on
Experimental					
4	neap	high	-	on	on
5	neap	high	-	-	on
6	spring	low	-	on	on
7	spring	low	-	-	on
8	neap	-	-	on	on

4.5 Results

4.5.1 Flushing Time

The longest flushing time (28.2 d) occurs during neap tide when river discharge is low river (Case 1) while the shortest value (19.4 d) is also found during neap, but when river discharge is high (Case 2), indicating that river discharge is more influential on flushing time than fortnightly variations of the tidal cycle (Figure 4. 3).

When particles are released during spring tide and river discharge is low river (Case 3), the flushing time is reduced by 5 d compared to when particles are released during neap tide with the same river discharge (Case 1). The flushing time from the spring tide release is shorter than from the neap tide release because a larger portion of the particles initially leaves the estuary during the spring tide release. The initial release is approximately three times larger based on the slope of the flushing time curve (not shown), which affects the overall flushing of the system. This is also the case in Moroccan estuaries as demonstrated by Haddout et al. (2020)

where the flushing time was found to be less during spring tide due to the enhancement of tidal currents compared to neap tide.

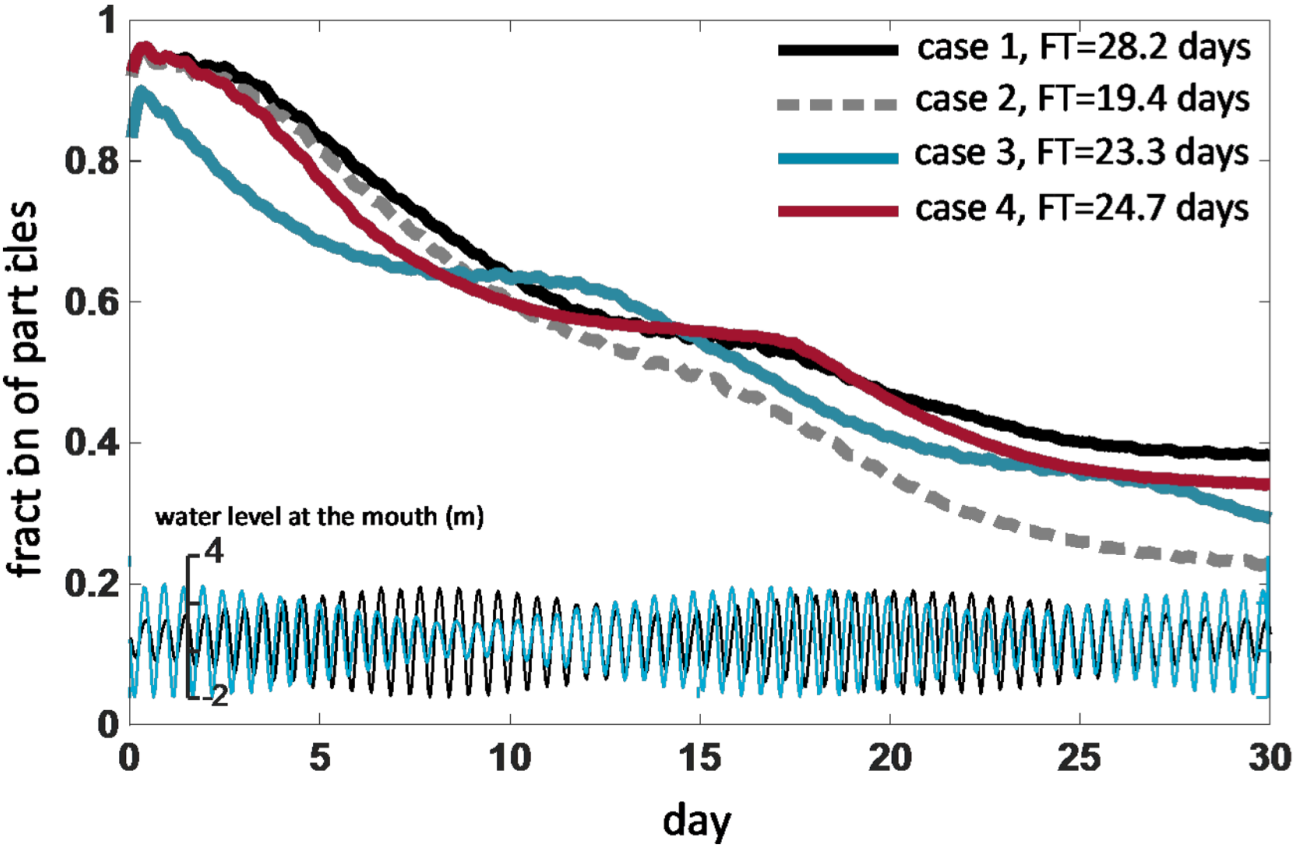

Figure 4. 3. Flushing time (FT) in the Gironde Estuary for the realistic cases (Case 1- neap tide release and low river discharge, Case 2- neap tide release and high river discharge, and Case 3- spring tide release and low river discharge), the barotropic case (Case 4 - neap tide release, high river discharge with no salinity). The tidal range for the neap tide release (black) and the spring tide release (blue) are shown at the bottom.

Suppressing salinity (Case 4 in Table 4. 1) results in an increase in the flushing time by 5 d (Case 4 compared to Case 2) as portrayed in Figure 4. 3. This indicates that the presence of density gradient enhances the flushing time and that this enhancement is as important as the spring-neap tidal variation. When suppressing advection and salinity (Case 5 in Table 4. 1), the flushing time increases from 24.7 d (Case 4, neap tide release, high river discharge, no salt) to 27.5 d (Case

5, neap tide release, high river discharge, no advection, so salt) (~3 d increase). This suggests that advection also enhances the flushing of the estuary and may act in concert with the density gradients. To further explore this, Case 3 with a spring tide release, low river discharge, and advection and salinity both included was compared to cases 6 and 7 with the same tide and river discharge conditions, but with salinity not included and neither salinity nor advection included, respectively.

When salinity was not included during the spring tide release and low river discharge, the flushing time in the Gironde increased from 23.3 d (Case 3) to 34.0 d (Case 6). When advection

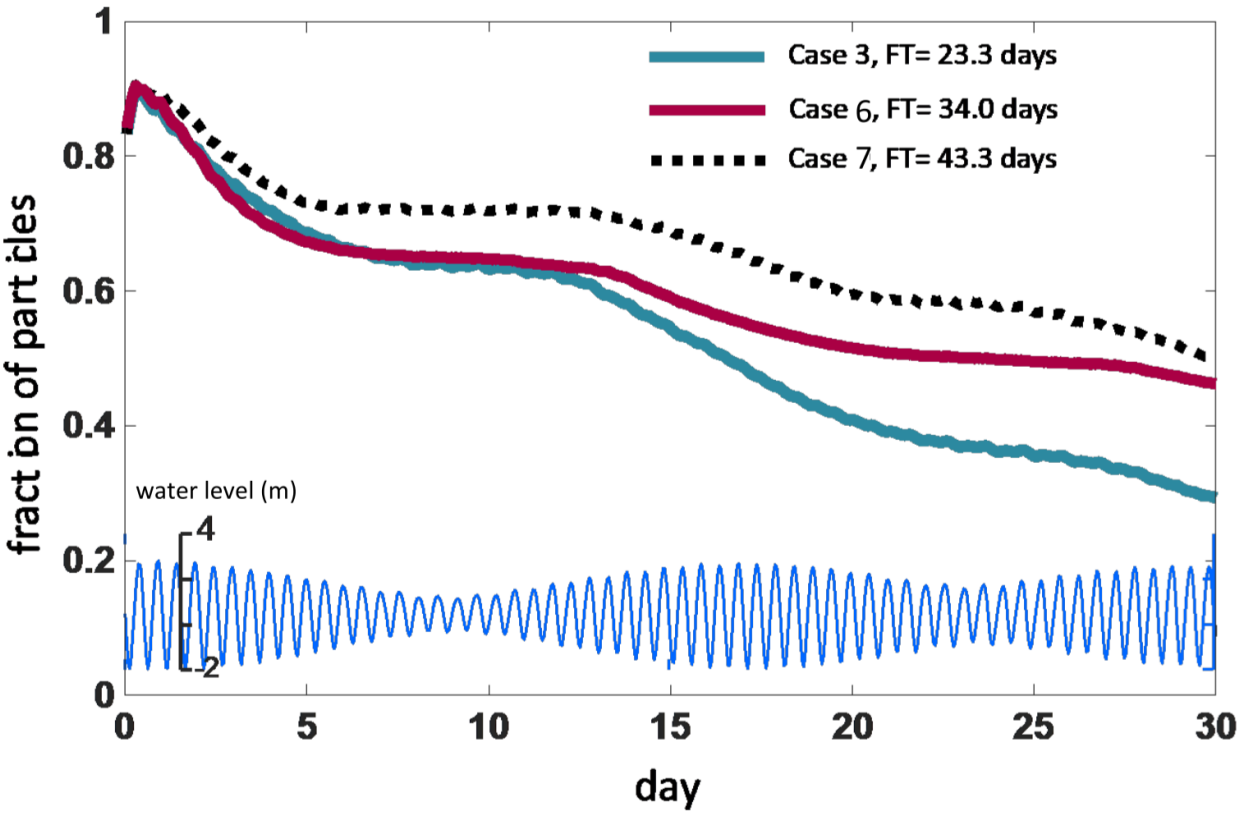

Figure 4. 4. The flushing time (FT) in the Gironde considering Case 3 (spring tide release and low river discharge), Case 6 (spring tide release, no salt and low river) and Case 7 (spring tide release, no salt, no advection). The flushing time value for each case is reported in the figure legend in days. The tidal range for the spring tide release (blue) is shown at the bottom.

and salinity were both excluded, the flushing time increased to 43.3 d (~20 d of increase) when (Case 7). During the spring tide release, the flushing time of the Gironde Estuary for both cases 3 (with salinity) and Case 6 (no salinity) are similar up until approximately day 12 and thereafter start to deviate. This will be further elaborated upon later in this section.

4.5.2 Ocean-Estuary Transport

As particles in the Gironde Estuary escape to the Bay of Biscay, some particles from the ocean will inevitably enter the estuary. The fraction of the ocean particles (normalized based on the total number of the particles initially released in the estuary) in the Gironde reaches a maximum of approximately 20% after 15 d for the neap tide release during low river discharge (Case 1) (Figure 4. 5a). For the neap tide release when the river discharge is high (Case 2) a maximum of approximately 15% is reached after 12 days. The ocean particles travel up to ~30 km from the mouth during high river discharge (Figure 4. 5b) and ~37 km during low river discharge (up to Lamena, Figure 4. 5c). This does not comply with the extent of the salinity intrusion, especially during low river discharge conditions, as it can reach up to Bordeaux which is ~110 km from the estuary mouth (Deborde et al., 2007).

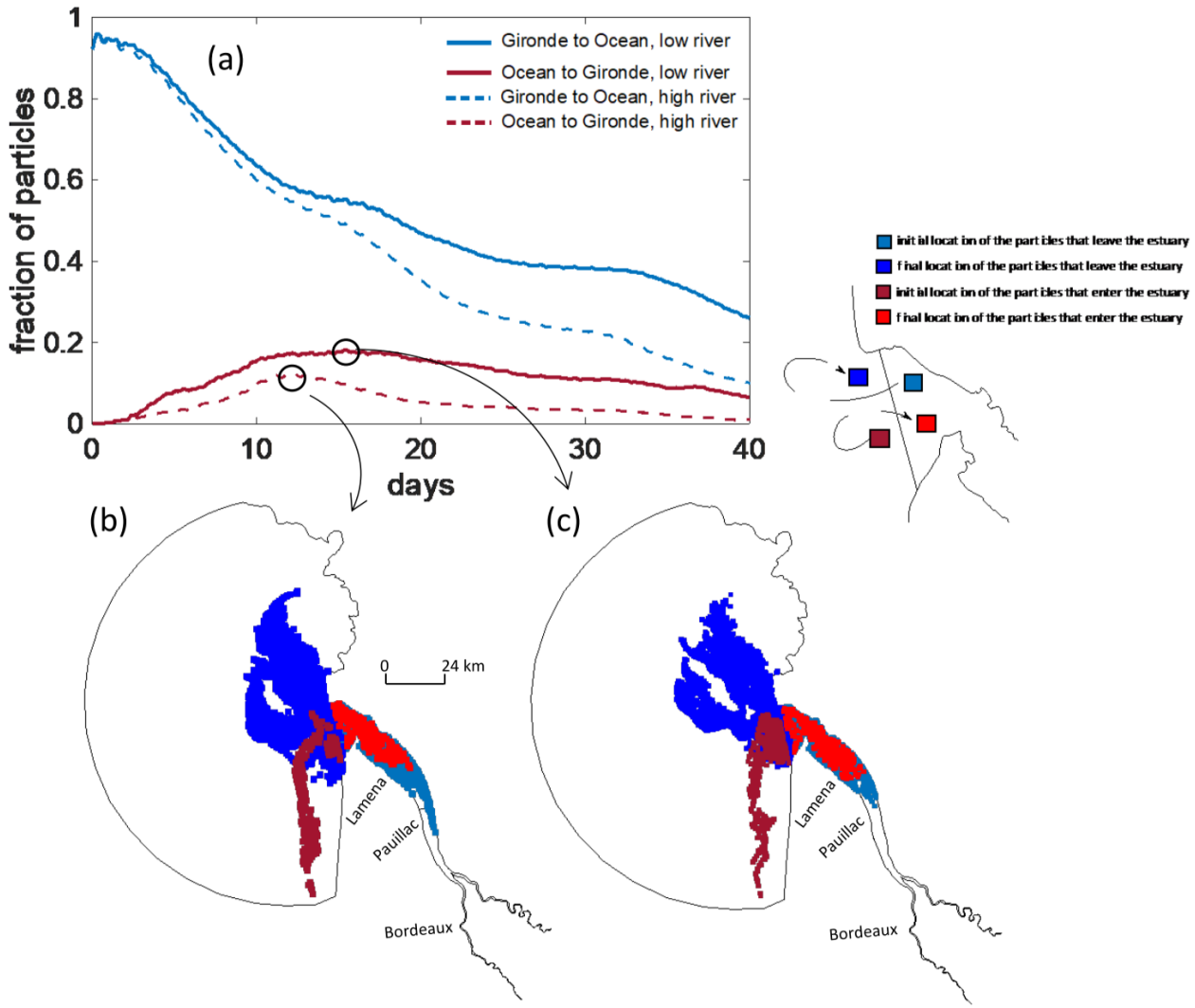

Figure 4. 5. The transport between the Gironde Estuary and the ocean for a neap tide release for high and low river discharge conditions (a). The initial and the final location of particles from the Gironde Estuary and the ocean when ocean-estuary transport is maximum (maximum number of the ocean particles enter the estuary) are detailed during high (b) and low (c) river discharge conditions.

4.5.3 Residence Time

The residence time increases from the mouth (~0-5 d) upstream (>40 days) in all of the realistic cases (case1, 2 and 3; Figure 4. 6). This is expected since particles near the mouth have a shorter distance to travel to leave the estuary than particles upstream. However, a notable increase in residence time values (from 15 days to >40 days) is observed in upstream Lamena (~ 40 km from the mouth) (Figure 4. 6).

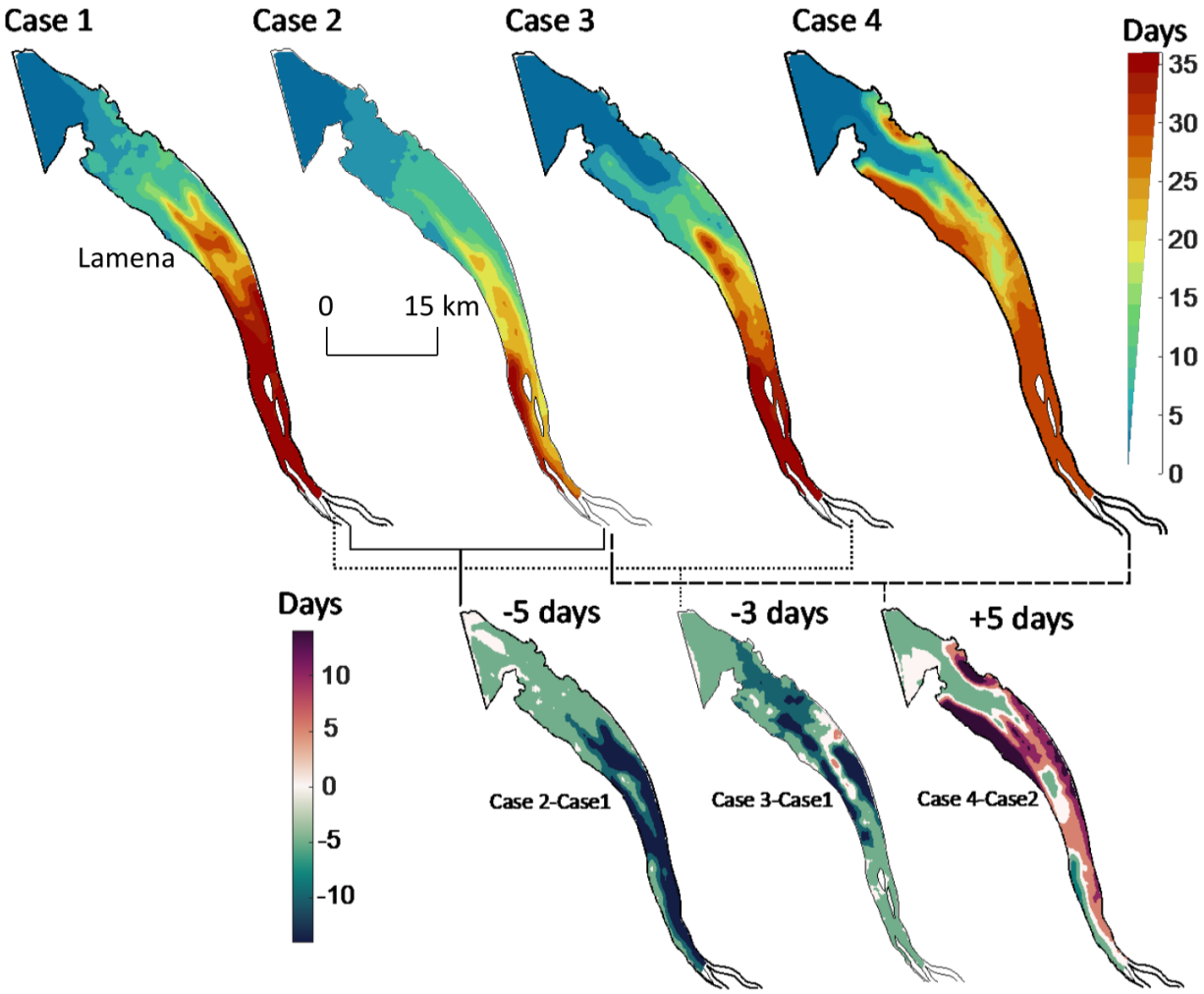

Figure 4. 6. The top panel shows the residence time in the Gironde Estuary for Case 1 (neap tide release and low river discharge), Case 2 (neap tide release and high river discharge), Case 3 (spring tide release and low river discharge) and Case 4 (neap tide release and high river discharge with no salinity). The bottom panel shows maps of the difference in residence time between the cases and highlights the area average difference in residence time as well. (Approximated values)

When salinity was not included during the neap tide release and high river discharge (Case 4, Table 4. 1) a different residence time pattern (Figure 4. 6, Case 4) resulted than that found in Case 2 (same case with salinity included, Figure 4. 6). In Case 4, residence time increased downstream of Lamena over the shoals. This is in line with the findings of Alahmed et al. (2020)

who showed that residual outflow over the shoals due to density gradients was weakened when density gradients were excluded. They found that this is attributed to density-gradients augmenting the seaward flows over the shoals in the downstream estuary.

The average residence time of the Gironde is reduced by ~3 d when comparing the spring tide release to the neap tide release with low river discharge (Figure 4. 6, Case 1 and 3). Near the estuary mouth residence times were low (~0-5 days) during the neap tide release (Case 1 and 2) but during the spring tide release the low residence time of ~0-5 days increases ~10 km landward (Case 3, Figure 4. 6). This can be attributed to the increase in tidal excursion during spring tide (~20 km) compared to that of neap tide (~5 km) allowing more particles along the estuary to reach the exit over a tidal cycle. Increasing the river discharge reduces the average residence time of the estuary by ~5 d (Figure 4. 6, Case 2). Upstream Lamena (~40 km from the estuary mouth), the residence time reduces by ~10 d during high river discharge compared to low river discharge (Case 1 and 2; Figure 4. 6), while the residence time in the downstream estuary (< 40 km from the mouth) reduces by less than ~5 days (Case 1 and 2; Figure 4. 6). This indicates that river discharge is more influential on the residence time in the upper-estuary (> 40 km from the mouth) than downstream (< 40 km from the mouth).

The extent to which salinity and river discharge impact the residence time varies along the estuary. However, the residence time values are evaluated based on a predetermined delineation line that was chosen as the estuary mouth. The residence time, as well as the flushing time, may drastically change as the delineation line is relocated spatially in the estuary.

4.5.4 Flushing Time in the Estuarine Subdomain

The flushing time of the Gironde estuary is greater than the fortnightly variation of tide, making it difficult to foresee the impact of the spring-neap tide release on transport timescales along the estuary. This becomes more apparent when considering that the tidal excursion in the Gironde Estuary is much less than the length of the estuary, which indicates that the residual circulation could influence the transport process. As Alahmed et al. (2020) found that residual flow structure and forcing mechanisms can vary along macrotidal estuaries, transport timescales will likely have varying degrees of sensitivity to changes in river discharge, density gradients, and advection along-estuary. To investigate this, the Gironde Estuary numerical domain was divided into four segments as shown in Figure 4. 7. Each segment is 20 km long, which is equivalent to the average tidal excursion length during spring tide in the estuary. The flushing time in each segment is calculated considering some of the scenarios presented in Table 4. 1 as reported in Table 4. 2. The flushing time values are compared within the same row to understand the role of river discharge, advection, density gradients, and tide in modulating the flushing time along the macrotidal estuary.

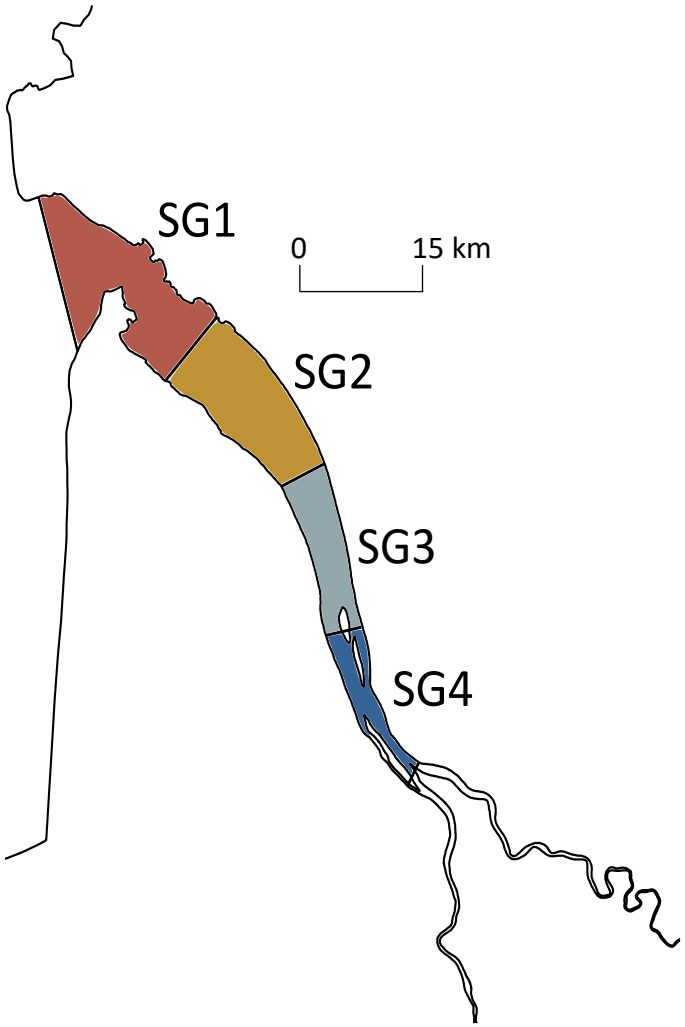

Figure 4. 7. The Gironde Estuary divided into segments. The length of each segment is 20 km and was determined based on the average tidal excursion length in the estuary during spring tide.

Table 4. 2. The flushing time value for each segment in the estuarine subdomain for several numerical simulation cases highlighting the importance of advection, density gradient, river discharge and tide. The case numbers reflect the same scenarios as presented in Table 4.1.

segment	Case 1 neap, low river	Case 2 neap, high river	Case 3 spring, low river	Case 4 neap, high river, no salt	Case 5 neap, high river, no salt, no advection	Case 8 neap, no river
SG1	8.1	7.5	4.9	5.3	9.0	5.8
SG2	12.7	7.3	7.7	13.0	13.7	49.4
SG3	17.4	5.6	7.0	5.2	6.14	28.95
SG4	12.7	2.5	3.0	2.5	2.3	55.618

Suppressing the density gradient impacts the flushing time in SG2 the most (80% increase from Case 2 vs Case 4, Table 4. 2). In the Gironde Estuary, this segment was found to have the largest influence from density-driven pressure gradients on residual circulation (Alahmed et al., 2020 , see Figure 4d and Figure 7d in manuscript), which indicates that residual flow strength and structure is directly related to flushing time in this segment of the estuary. In contrast to SG2, the flushing time is reduced by 30% (Case 2 vs Case 4) in SG1 when the density gradient is suppressed. Suppressing the density gradient has the least impact on flushing time in the upstream segments (SG3 and SG4). This is attributed to the relative contribution of density-induced flow to the residual circulation reducing upstream and barotropic pressure gradients from a combination of tidal and river influence dominating residual flows (Alahmed et al., 2020 , Figure 4d and Figure 7d).

The river discharge had the minimum impact on flushing time in SG1 (Table 4. 2, Case 4 vs Case 8) and maximum in all upstream sections (SG2, SG3, and SG4; Table 4.2). Suppressing the river discharge in the upstream segments increased the flushing time by 280% in SG2, 400% in SG3, and by 2000% in SG4. Advection, on the other hand, had a minimum impact on the flushing time in these regions (SG2-SG4) as the relative importance of advection to the residual

momentum balance reduces upstream compared to the mouth where the bathymetry is most complex (Alahmed et al., 2020). In SG1, suppressing advection increased flushing time by 100% (Table 4. 2, Case 5 vs Case 4). When comparing neap tide to spring tide release with low river discharge, the flushing time is reduced in all segments during spring tide (Case 1 vs Case 3 in Table 4. 2), which is likely due to the residual flow magnitude increasing from neap to spring tide (Alahmed et al., 2020). It has been found that flushing times respond differently to changes in river discharge, advection, and density gradients along the macrotidal estuary. It is surmised that this is due to the along-channel variations in residual flow structure and drivers. The following section aims to directly link residual flow dynamics to transport times in macrotidal estuaries.

4.6 Discussion

This study aims to investigate the impact of temporal variations of advection, river discharge, and thus density gradients, on flushing times in macrotidal estuaries, and to identifying if along-channel variations of residual circulation and drivers produce along-channel variations in transport timescales. The results indicate that along-channel changes in residual flow drivers, such as density gradients and advection, correlate with the along-channel variations in transport timescales with qualitatively comparing transport timescale results to those of Alahmed et al.(2020). However, it is still unclear how and why advection and density gradients link to flushing times along the estuary and why river discharge is the most important driver for the transport inside the macrotidal estuary.

4.6.1 Advection and Density Gradients.

When the residual streamlines are longer than the tidal excursion, it is expected for the particles' motion and the transport timescales to be governed by the residual flow (Zimmerman,

1976). This is because the distance traveled by the particles due to the tidal current is smaller than the residual eddy size and, therefore, their motion will be determined by the residual eddy. The residual streamlines are defined as the curve tangent to the residual velocity vector (Zimmerman, 1981). The length of the streamline can be defined as the radius of the residual eddy or can be quantified by the arc length method. The flushing time in the Gironde Estuary is influenced by the residual flow because the residual streamline length is longer than the tidal excursion during neap and spring tide (Figure 4. 8a) except near the mouth (up to 20 km up estuary). While the tidal excursion in the estuary can reach up to 25 km during spring tide (maximum tidal excursion), the residual streamline length inside the estuary surpasses 60 km (during neap and spring) allowing for the residual flow to drive the flushing inside the estuary. Due to the width constriction and intricate bathymetry near the mouth, horizontal residual eddies develop (Figure 4. 8b, c). As a result, the tidal excursion length exceeds the residual streamline length (Figure 4. 8a) and the tide has a greater impact on the flushing time than the residual flow. The impact of bathymetry and estuarine morphology is eliminated when advection is suppressed. Thus, no residual eddies develop near the mouth (Figure 4. 8d), and the length of residual streamlines increase (>80 km) allowing for the residual flow to drive the flushing time. It was found that advection is a dominant driver of residual flow near the mouth of the Gironde Estuary (Alahmed et al., 2020). Therefore, when advection is suppressed the residual flow magnitude near the mouth (SG1) reduces (Figure 4. 9c compared to Figure 4. 9b), resulting in an increase in the flushing time in SG1 (Table 4. 2). This implies that advection is important to the flushing time near the mouth not only because it augments the magnitude of residual flow, but

also because it reduces the residual streamline length by generating horizontal residual eddies allowing for the tide to be more influential in flushing the system.

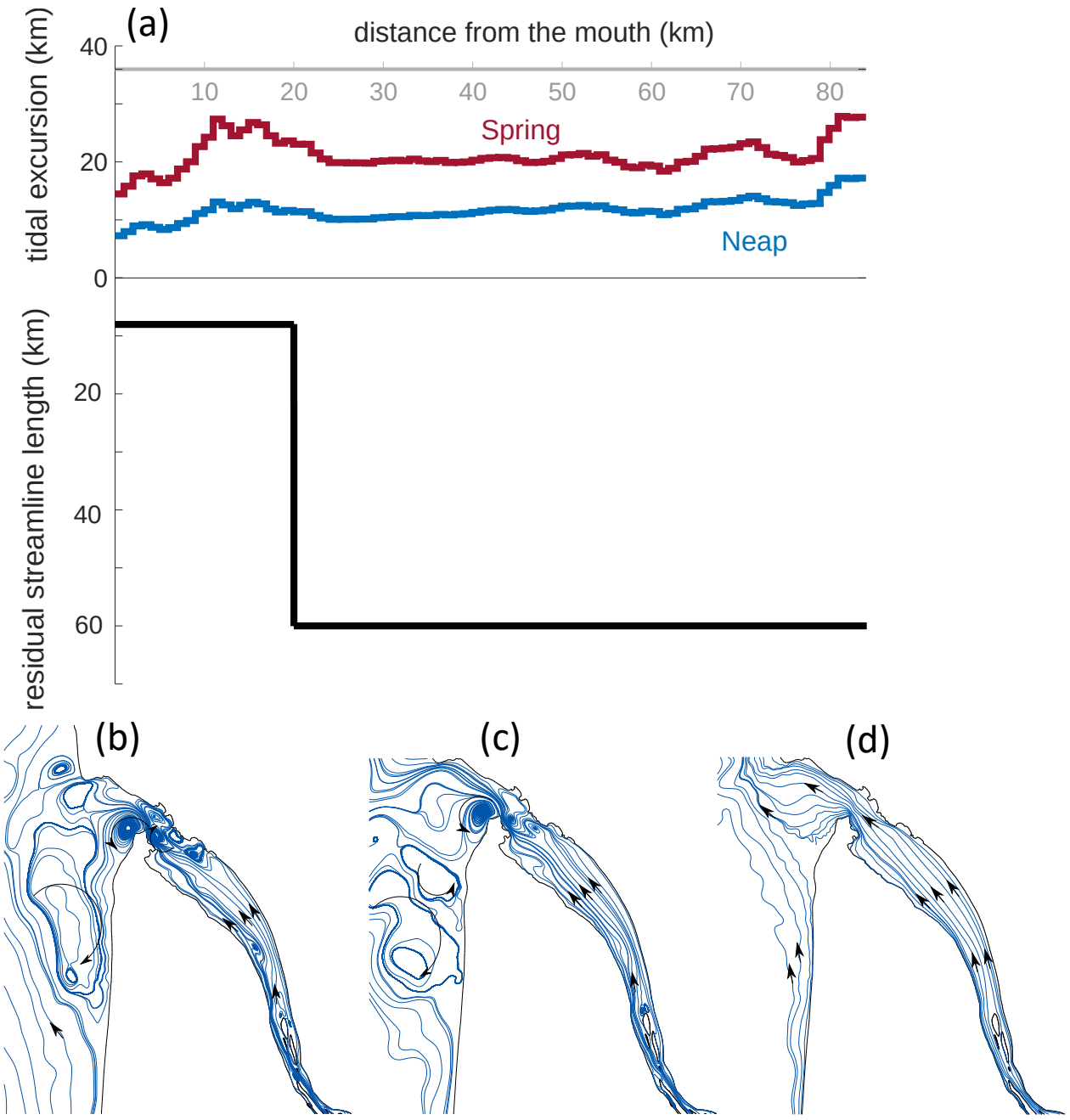

Figure 4. 8. The tidal excursion and residual streamline length during neap (blue line) and spring (red line) tide (a), the depth-averaged residual streamlines during neap (b), spring (c) and neap tide with advection off (d). The arrows in b, c, and d denote the flow direction.

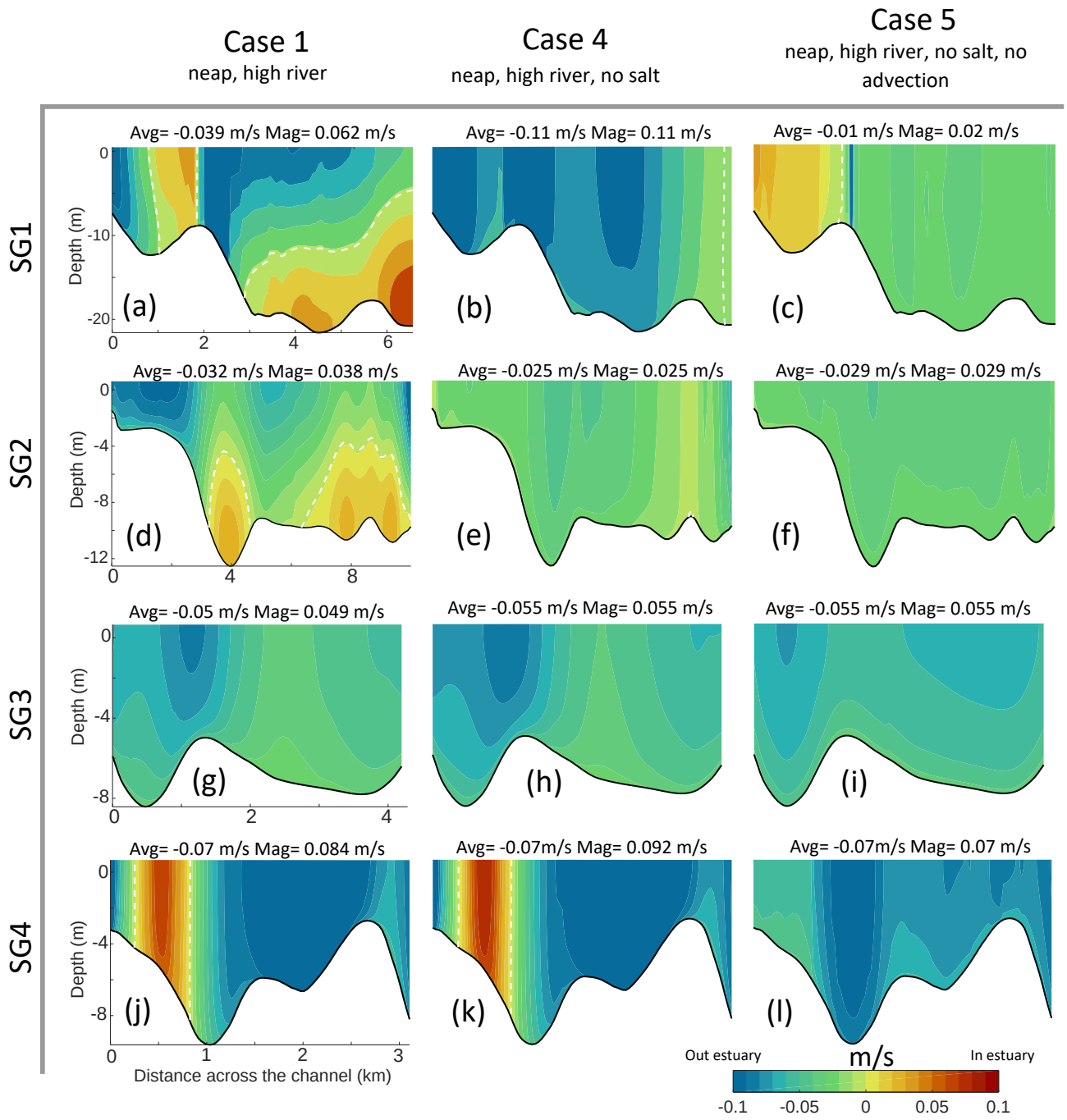

Figure 4. 9. Contours of the along-channel residual velocity at transects in each segment along the estuary for Case 2 (neap tide release and high river discharge), Case 4 (neap tide release and high river discharge with no salt) and Case 5 (neap tide release and high river discharge with no salt nor advection). Perspective of the transects is seaward. The white dashed line denotes zero flow. The area average of the residual flow (Avg) and the area average of the residual flow magnitude (Mag) are reported for each case above each subplot.

The area-averaged residual flow (-0.039 m/s) near the mouth is negative indicating a net seaward transport in SG1 (Figure 4. 9a). When density gradient is suppressed, the area-averaged residual flow is enhanced (-0.11 m/s) as the landward flow that would be induced by the density gradient is removed (Figure 4. 9b). Therefore, suppressing the density gradient results in a decrease in the flushing time in SG1 as indicated in Table 4. 2. Conversely, the flushing time increases at SG2 when the density gradient is suppressed because the seaward net flow (Figure 4. 9d, -0.032m/s) is reduced (Figure 4. 9e, -0.025 m/s). The density gradient is a primary driver for the residual flow at SG2 (Alahmed et al., 2020) and creates a two-layer flow with seaward flow at the surface and landward flow at the bottom (Figure 4.10d), explaining why the net seaward component is reduced when suppressing the density gradient at SG2 (Figure 4.10e), causing an increase in the flushing time. In the upstream segments (SG3 and SG4), suppressing the density gradient has little influence on the residual flow (Figure 4. 9h, k) and, therefore, does not affect the flushing time. This is in accordance with Alahmed et al., (2020) as they demonstrated that the density gradient in the estuary upstream is not important to the residual flow. Advection does not affect the average residual flow at the upstream segments (SG3 and SG4) and, does not impact the flushing time as a result. The reason that the advection impact on the residual flow pattern in SG4 is more pronounced than it in SG3 because the transect of SG4 is located near the island by the river confluence (Figure 4. 7) where tidal nonlinearities may be promoted. The influence of river discharge on flushing times is therefore investigated.

4.6.2 River Discharge

The river discharge velocity calculated per unit width and depth was found to be 0.01 m/s, during high river discharge mid-estuary. This is an order of magnitude less than the residual flow

magnitude during neap and spring tide with no river discharge at the same along-estuary location (not shown). This implies that the river discharge does not notably contribute to the residual flow magnitude although it remains influential to the flushing time in the upper estuary (SG3 and SG4; Table 4.2). This could be due to the combined influence of barotropic pressure gradients caused by the river discharge working in concert with amplification of the water level due to tides entering a macrotidal and convergent estuary (Ross & Sottolichio, 2016). Therefore, the along-

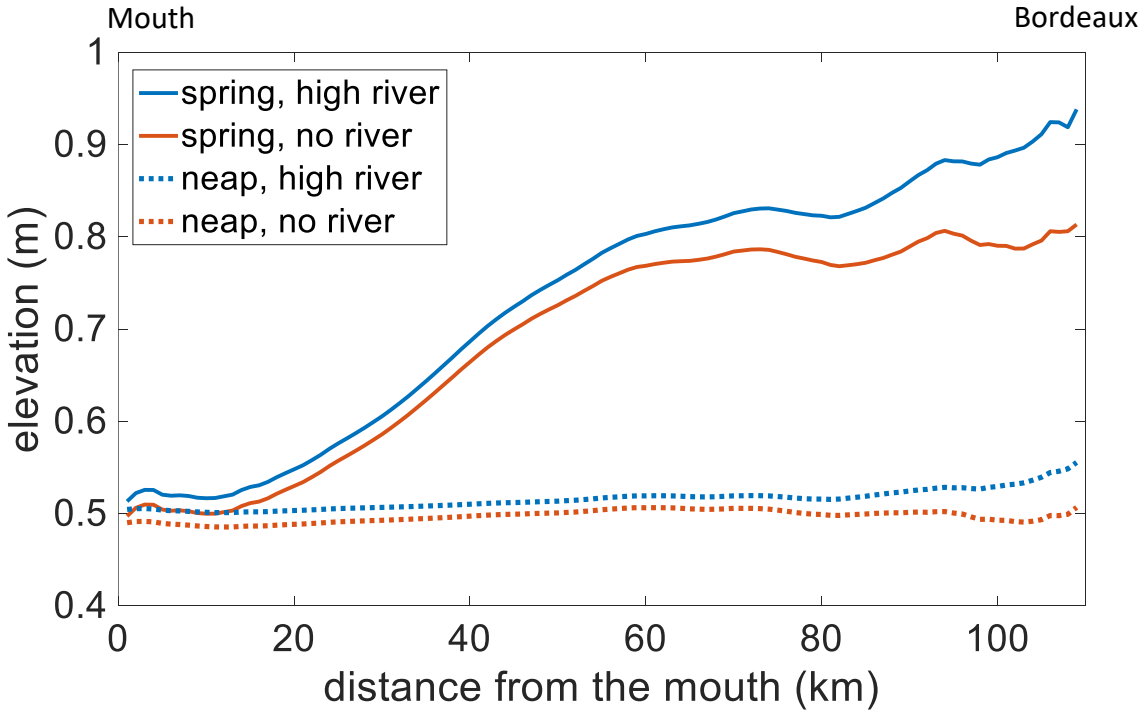

Figure 4. 10. The residual free surface elevation along the estuary during spring (solid lines) and neap tide (dashed line) with high river and no river discharge conditions.

channel variation in the residual water level was investigated during neap and spring tides and high and low river discharge scenarios (Figure 4.11). The spring neap variation of the residual free surface elevation ($\bar{\eta}$) is more pronounced than that due to the river discharge. The question then remains, why river discharge is critically important to the flushing of the system at the location where tidal variations in the barotropic pressure gradient dominate?

To determine the relative influence of the barotropic river discharge on the transport, the river-induced flow is compared to the Stokes drift. The Stokes drift is a product of the covariance between the water level and velocity (L. Guo et al., 2014) and generates a residual current estimated by the following equation (L. Guo et al., 2014; Moftakhari et al., 2016),

$$V_s = \frac{1}{2} U\eta \, cos(\phi) \, / h_o \qquad 4.1$$

in which, U and η are the tidal current magnitude and tidal amplitude, respectively, ϕ denotes the phase difference between the tidal current and tidal elevation, and h_o is the mean depth. Not that this flow must be compensated by a return flow, coined the Eulerian Stokes Drift Return Flow in Moftakhari et al. (2016). It is this return flow that would augment river-induced residual flows. If it is assumed that the barotropic pressure gradient in the upper-estuary (SG3 and SG4)

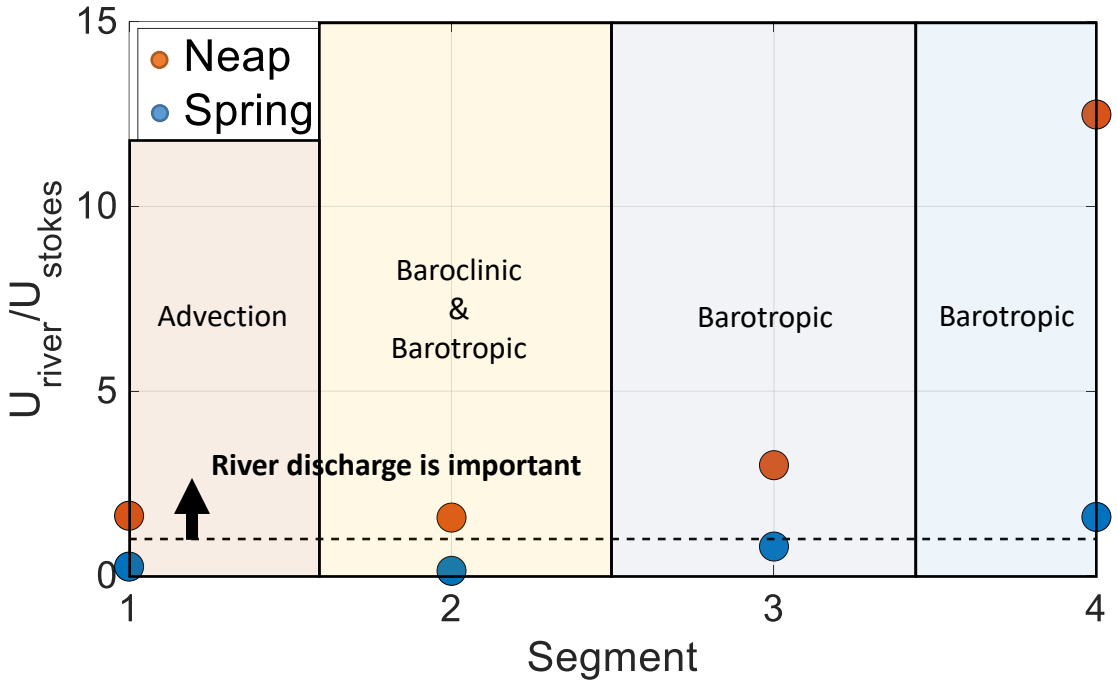

Figure 4. 11. The relative importance of river discharge to Stokes drift at each segment along the estuary during neap and spring tide. The figure highlights the dominant forces of the residual flow at each segment. The dashed line is where the ration of the river flow to the Stokes drift is one.

is the dominant force of the residual flow, then in the absence of river discharge, the residual flow induced by the barotropic pressure gradient is equivalent to the residual flow induced by the Stokes drift (Li & O'Donnell, 2005). The ratio of the river velocity during high river discharge to the flow induced by the Stokes drift (barotropic tide with no river discharge) are evaluated at each along-estuary segment (area averaged) as reported in Figure 4. 11.

The ratio between the barotropic river flow and the barotropic tide flow shows that the river discharge is important in the upstream segments (SG2-SG4, $\frac{U_{river}}{U_{stokes}} > 1$) during neap tide (Figure 4. 11). Furthermore, the river discharge shows to be as or more important than the barotropic tide flow in SG3 and SG4 even during spring tide. This indicates that the river discharge is critical for the flushing time of the estuary in upstream (SG3 and S4), which may also help explain why the river discharge is critical to the sediment transport upstream as well (Castaing & Allen, 1981). At SG1, tidal currents interacting with the complex bathymetry elevate advection and thus the residual flow. Therefore, the ratio between the river flow and the Stokes drift return flow (barotropic tide) may not be reliable.

4.6.3 Limitation and Uncertainties

The boundaries of the model are forced by the realistic tide, realistic river discharge, and salinities based on satellite data obtained from HYCOM, https://www.hycom.org/. The intention is to reproduce a flushing behavior in a macrotidal estuary, however, the model does not take into account the impact of wind, which could change the residual circulation and the transport timescales (Mitra et al., 2020). A seaward wind, for example, produces a seaward flow at the surface layer and landward flow at the bottom layer augmenting the density-driven circulation

(Wong, 1994) and may result in a decrease in flushing time in regions where density-driven flow is important to the circulation of the estuary. This requires further analysis to understand the extent to which the wind can contribute to the flushing of the Gironde estuary.

The numerical model is validated based on measured data at few locations along the estuary. This may raise some questions about the model validity in other locations within the domain. In addition, even at these few locations, the numerical outcome does not show a perfect agreement with the measured data (Figure 4. 1d and e) indicating some level of uncertainties in the numerical outcomes. Uncertainties in the numerical outputs may arise due to the error in bathymetry, bottom drag, numerical computation/setup, for example, and propagate into the numerical outcome (Laborie et al., 2020). The uncertainties in the numerical outcomes can be determined by performing a sensitivity analysis. Time step sensitivity analysis is carried out in this work to assure the convergence of the model and to determine the uncertainty in the transport timescales that may arise due to this factor (i.e., numerical time step).

When varying the time step from 1.5s (the time step considered for all the cases in Table 4. 1) to 1s and 0.5s, the flushing time of the Gironde estuary is reduced by only 0.3 days as seen in Figure 4. 12a. The average residence time of the estuary is also reduced by 0.3 days when varying the time step from 1.5 s to 0.5 s while the uncertainties in the residence time value can reach up to $\pm$ 2 days as reported in Figure 4. 12b. This is due to the chaotic behavior of the

particles as well as the truncation error in the numerical model and the precision capacity of the computer being utilized

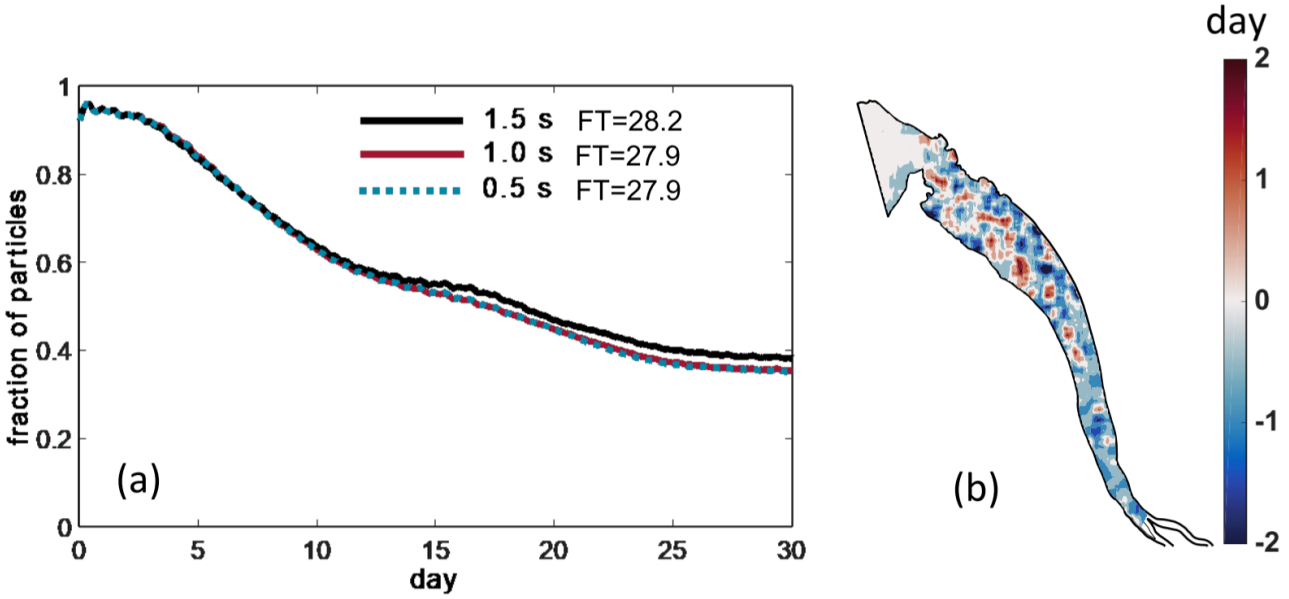

Figure 4. 12. The flushing time of the Gironde estuary for different numerical time step during neap release and low river discharge (a), and the uncertainties in residence time due to the numerical outcomes resulted from the numerical time step (b).

4.7 Conclusion

A comprehensive Lagrangian tracking approach is adopted to understand the flushing and residence time in a macrotidal estuary with realistic geometry using a three-dimensional hydrodynamic model. Results show that the flushing time of the estuary varies between 19. 4 days to 28.2 days from high to low river discharge, and from 23.3 days to 28.2 days depending on neap or spring tide particle release. The residence time results indicate that the transport timescales can vary remarkably along the estuary and in response to changes in density gradients, tidal range, and river discharge and are attributed to along-estuary variations in residual dynamics. It has been found the density-gradients are critical to the flushing at locations where the density-gradient is relative to the residual flow dynamics. Suppressing the density gradient in these locations resulted in an 80% increase in the flushing time. It has also been found that the

river discharge is the most prominent driver of flushing time in the upper reaches of the estuary. This was confirmed by quantifying and comparing the river-induced flow to the Stokes drift return flow, the latter of which is driven by tides. This effect of the river is so pronounced that when it is not included flushing times can be enhanced by up to 2000% in the upper estuary and by more than 500% for the entire estuary. The flushing near the estuary mouth is not affected by the river discharge. This is because advection becomes a dominant force in driving the residual flow, creating residual eddies when tidal currents come in contact with the complex geometry.

These results imply that the health of the Gironde estuary, as well as other macrotidal and convergent estuaries, may heavily depend on the river discharge. As such, monitoring and regulating contaminants from freshwater inflow should be a priority in these systems. Further, the implications of installing dams in upper river branches will likely reduce estuary flushing and ocean-estuary transport. Future studies should include the role of wind forcing on flushing times.

CHAPTER 5
SUMMARY AND CONCLUSIONS

This thesis aims to better characterize circulation and transport in tidally dominated estuaries considering a wide variety of realistic estuaries of varying shape and freshwater input. To attain the goal, three-dimensional numerical models were developed and validated based on two distinct natural systems as case study sites, the Frenchman Bay-Blue Hill Bay multi-estuary, mesotidal (2 m < tidal range < 4 m) system in Maine, USA, and the Gironde Estuary, a macrotidal (tidal range > 4m) and convergent estuary in France. Several numerical experiments were performed considering the impact of river discharge, density gradients, and tidal range in driving the residual circulation and the transport timescales (flushing and residence time). The flushing and residence times were quantified by using a Lagrangian tracking analysis. Concluding remarks of each study in this thesis as well as overall conclusions and future work recommendations are provided in the following sections.

5.1 Chapter 2: Residual Flow in Mesotidal Estuaries

This chapter investigated residual circulation and transport timescales in mesotidal estuaries. It was concluded that river inflow rates and density gradients related to salt concentration can play a major role in determining estuary flushing behavior. This was found to be particularly true in estuaries where the length of residual streamlines exceeded the tidal excursion length. In this case, the presence of residual eddies induced by estuary geometric complexity (constrictions, headlands, etc.) trapped particles resulting in high residence time and therefore potential water quality issues.

In systems where the tidal excursion length is comparable to estuary length, residence time was found to be less than or equal to the tidal period. Such systems are likely less sensitive to pollution issues such as the Jordan River Estuary presented in this study. Based on the results presented in chapter 2, it can be concluded that in locations where the tidal excursion is longer than residual eddy size and shorter than the length of the system, particles will be retained in the system for some time longer than one tidal cycle, indicating that the estuary is susceptible to pollution.

5.2 Chapter 3: Residual Flow in a Macrotidal Estuary

Chapter 3 aimed to understand the along-channel variability of residual flow structure and forcing mechanisms in tidally dominated estuaries. It was found that the density gradients are an important driver of the residual flow during neap tide and in the downstream estuary (>30 km from the mouth). In the upper-estuary (> 30 km from the mouth), residual flows were driven by the barotropic pressure gradient during both neap and spring tide, but the effect was enhanced during spring tide and high river discharge, creating a predominant seaward residual flow. Near the estuary mouth, however, advection became the dominant driver of the residual flow during spring tide due to the width constriction and complex bathymetric features creating a laterally sheared along-channel residual flow with inflow in the channel and outflow over the shoals.

5.3 Chapter 4: Transport Timescales in a Macrotidal Estuary

This chapter investigates the residence time and flushing time in a macrotidal estuary and links these transport timescales to residual flow dynamics. Results showed that the sensitivity of the flushing time to advection, density gradients, and river discharge varied along the estuary

corresponding to longitudinal changes in the dominant residual flow driving mechanisms. In the upper estuary (> 40 km from the estuary mouth) barotropic pressure gradients became the dominant driver of the residual flow and river discharge was found to be the mechanism responsible for transport. This is because the upper estuary is characterized by relatively simple geometry (simple bed profile and no complex geometry such as headlands or islands). In the downstream estuary (> 40 km from the estuary mouth) advection dominated the residual flow and the flushing time was less sensitive to river discharge and other residual flow drivers such as density gradients.

5.4 Overall Conclusions

The work attempts to comprehensively study transport timescales in tidal estuaries by drawing a relationship between tidal excursion (the distance traveled by a water parcel over half tidal cycle), residual circulation, tide, and the estuarine shape. The interaction between tide, freshwater input, and estuarine bathymetry engenders a complex residual flow pattern and changes the sensitivity of the transport to these drivers in estuaries.

In wide mesotidal estuaries, the river discharge contributes to the residual flow and transport timescales through baroclinicity allowing the density gradients to drive the flushing time in such estuaries. In macrotidal estuaries, the density gradient becomes comparatively less important due to increased stress divergence attributed to the strong tide. Therefore, the barotropic river drives the flushing time as it augments the seaward net flow.

The presence of complex morphological features such as islands and headlands gives a rise for advection to dominate the residual flow creation generating residual eddies. In such locations,

the flushing and the transport process may be less sensitive to river discharge and density gradients.

The flow in estuaries can be intricate and may exhibit drastic temporal and spatial variations. The thesis, however, shows that regardless of this intricacy in the flow, it is possible to foretell what mechanism (river, tide, density gradient) drive the transport process in estuaries and whether to expect high or low flushing time based on simple metrics such as estuarine width and tidal excursion. Such knowledge and tool can be of great value for managers to create, at least as a first step, a general idea about the transport and the water quality in estuarine environments.

5.5 Future Work and Recommendations

Based on the work limitations of the work presented in this theses, the following recommendations are suggested for future research,

1- The Impact of Wind: The role of freshwater input, tidal range, advection, and density gradients in driving residual flow and the transport process in tidally-dominated estuaries were investigated, yet the wind impact was not considered in the current work. Wind can alter the residual circulation by augmenting or counteracting the density-driven flow and river discharge and, consequently, affect the flushing time of the estuaries. Therefore, future studies should consider the interaction of wind forcing with other relevant forcing mechanisms in tidally-dominated systems.

2- Idealization for Parametrization: This thesis has investigated when and in what type of estuaries river discharge, density gradients, and tides can be important to transport

processes. This was done considering several case study systems in the USA and France forced with the realistic tide and river discharge values. Studies based on idealized estuaries would identify the thresholds beyond which a specific mechanism (e.g. river discharge) is considered to be important to residual and transport timescales.

3- Pollution from River During a Rainfall Event: It has been found that the river discharge can be critical to the flushing time of tidally dominated estuaries. The higher the river discharge, the shorter flushing time. The study, however, considers a constant river discharge value over a period of one month. The river discharge value may drastically change over a relatively short time (24 hours) during a rainfall event. A high river discharge event may bring about high pollution loads to estuaries, affecting the water quality. It is therefore recommended that future studies investigate the impact of river-flushed pollution during heavy rainfall events in estuaries for better water quality assessment and management.

4- Salinity Intrusion: The Lagrangian analysis suggests that the transport of ocean particles into a macrotidal estuary is at least 40 km less than the salinity intrusion. This indicates that diffusion (horizontal and vertical) plays a role in extending the salinity intrusion up-estuary. The role of advection/diffusion process on salinity intrusion may be considered in a follow-up study.

BIBLIOGRAPHY

Alahmed, S., Ross, L., & Sottolichio, A. (2020). The role of advection and density gradients in driving the residual circulation along a macrotidal and convergent estuary with non-idealized geometry. *Continental Shelf Research*, 104295. https://doi.org/https://doi.org/10.1016/j.csr.2020.104295

Allen, Salomon, J. C., Bassoullet, P., Du Penhoat, Y., & De Grandpre, C. (1980). *Effects of tides on mixing and suspended sediment transport in macrotidal estuaries*. *Sedimentary Geology* (Vol. 26). Elsevier.

Allen, G. P. (1973). *Etude des processus sédimentaires dans l'estuaire de la Gironde* (Vol. 5). Institut de géologie du bassin d'Aquitaine.

Azevedo, I. C., Bordalo, A. A., & Duarte, P. M. (2010). Influence of river discharge patterns on the hydrodynamics and potential contaminant dispersion in the Douro estuary (Portugal). *Water Research*, *44*(10), 3133–3146.

Banas, N. S., & Hickey, B. M. (2005). Mapping exchange and residence time in a model of Willapa Bay, Washington, a branching, macrotidal estuary. *Journal of Geophysical Research: Oceans*, *110*(C11).

Bárcena, J. F., Gómez, A. G., Garc\'\ia, A., Álvarez, C., & Juanes, J. A. (2017). Quantifying and mapping the vulnerability of estuaries to point-source pollution using a multi-metric assessment: The Estuarine Vulnerability Index (EVI). *Ecological Indicators*, *76*, 159–169.

Basdurak, N. B., & Valle-Levinson, A. (2012). Influence of advective accelerations on estuarine exchange at a Chesapeake Bay tributary. *Journal of Physical Oceanography*, *42*(10), 1617–1634.

Bilgili, A., Proehl, J. A., Lynch, D. R., Smith, K. W., & Swift, M. R. (2005). Estuary/ocean exchange and tidal mixing in a Gulf of Maine Estuary: A Lagrangian modeling study. *Estuarine, Coastal and Shelf Science*, *65*(4), 607–624.

Bonneton, P., Bonneton, N., Parisot, J.-P., & Castelle, B. (2015). *Tidal bore dynamics in funnel-shaped estuaries*. *Journal of Geophysical Research: Oceans* (Vol. 120). Wiley Online Library.

Bordalo, A. A., Onrassami, R., & Dechsakulwatana, C. (2002). Survival of faecal indicator bacteria in tropical estuarine waters (Bangpakong River, Thailand). *Journal of Applied Microbiology*, *93*(5), 864–871.

Braunschweig, F., Chambel, P., Martins, F. A. B. da C., & Neves, R. (2008). A methodology to estimate the residence time of Estuaries.

de Brye, B., de Brauwere, A., Gourgue, O., Delhez, E. J. M., & Deleersnijder, E. (2012). Water renewal timescales in the Scheldt Estuary. *Journal of Marine Systems*, *94*, 74–86.

Burchard, H., & Hetland, R. D. (2010). *Quantifying the contributions of tidal straining and gravitational circulation to residual circulation in periodically stratified tidal estuaries*. *Journal of Physical Oceanography* (Vol. 40).

Burchard, H., Hetland, R. D., Schulz, E., & Schuttelaars, H. M. (2011). *Drivers of residual estuarine circulation in tidally energetic estuaries: Straight and irrotational channels with parabolic cross section*. *Journal of Physical Oceanography* (Vol. 41).

Callies, U., Plüß, A., Kappenberg, J., & Kapitza, H. (2011). Particle tracking in the vicinity of Helgoland, North Sea: a model comparison. *Ocean Dynamics*, *61*(12), 2121–2139.

Camacho, R. A., Martin, J. L., Diaz-Ramirez, J., McAnally, W., Rodriguez, H., Suscy, P., & Zhang, S. (2014). Uncertainty analysis of estuarine hydrodynamic models: an evaluation of input data uncertainty in the weeks bay estuary, alabama. *Applied Ocean Research*, *47*, 138–153.

Cameron, W. M., & Pritchard, D. W. (1963). Estuaries. In 'The Sea, vol. 2'.(Ed. MN Hill.) pp. 306--324. John Wiley & Sons: New York.

Cancino, L., & Neves, R. (1999). Hydrodynamic and sediment suspension modelling in estuarine systems: Part II: Application to the Western Scheldt and Gironde estuaries. *Journal of Marine Systems*, *22*(2–3), 117–131.

Carpenter, S. R., Caraco, N. F., Correll, D. L., Howarth, R. W., Sharpley, A. N., & Smith, V. H. (1998). Nonpoint pollution of surface waters with phosphorus and nitrogen. *Ecological Applications*, *8*(3), 559–568.

Castaing, P., & Allen, G. P. (1981). Mechanisms controlling seaward escape of suspended sediment from the Gironde: a macrotidal estuary in France. *Marine Geology*, *40*(1–2), 101–118.

Celik, I., & Rodi, W. (1985). Calculation of wave-induced turbulent flows in estuaries. *Ocean Engineering*, *12*(6), 531–542.

Chang, J. H. (1968). Climate and Agriculture and Ecological Survey. University of Hawaii. Ed. Aldine Publishing Company. Chicago.(USA). 304p.

Chant, R. J. (2002). *Secondary circulation in a region of flow curvature: Relationship with tidal forcing and river discharge*. *Journal of Geophysical Research: Oceans* (Vol. 107). Wiley Online Library.

Chant, R. J. (2010). *Estuarine secondary circulation*. *Contemporary Issues in Estuarine Physics*. Cambridge University Press Cambridge.

Cheng. (2014). *Decomposition of residual circulation in estuaries*. *Journal of Atmospheric and Oceanic Technology* (Vol. 31).

Cheng, P., & Valle-Levinson, A. (2009). Influence of lateral advection on residual currents in microtidal estuaries. *Journal of Physical Oceanography*, *39*(12), 3177–3190.

Cheng, P., Valle-Levinson, A., & de Swart, H. E. (2011). A numerical study of residual circulation induced by asymmetric tidal mixing in tidally dominated estuaries. *Journal of Geophysical Research: Oceans*, *116*(C1).

Cheng, P., Wang, A., & Jia, J. (2017). Analytical study of lateral-circulation-induced exchange flow in tidally dominated well-mixed estuaries. *Continental Shelf Research*, *140*, 1–10.

Cheng, P., Mao, J., Yu, F., Chen, N., Wang, A., & Xu, F. (2019). A numerical study of residual flow induced by eddy viscosity-shear covariance in a tidally energetic estuary. *Estuarine, Coastal and Shelf Science*, *230*, 106446.

Cheng, P., Yu, F., Chen, N., & Wang, A. (2019). Observational study of tidal mixing asymmetry and eddy viscosity-shear covariance--induced residual flow in the Jiulong River estuary. *Continental Shelf Research*, 104035.

Cheng, R., & Gartner, J. W. (1985). Harmonic analysis of tides and tidal currents in South San Francisco Bay, California. *Estuarine, Coastal and Shelf Science*, *21*(1), 57–74.

Costanza, R., D'Arge, R., De Groot, R., Farber, S., Grasso, M., Hannon, B., et al. (1997). The value of the world's ecosystem services and natural capital. *M. VAN DEN BELT*, 253–260.

Cucco, A., Umgiesser, G., Ferrarin, C., Perilli, A., Canu, D. M., & Solidoro, C. (2009). Eulerian and lagrangian transport time scales of a tidal active coastal basin. *Ecological Modelling*, *220*(7), 913–922.

Davies, J. L. (1964). A morphogenic approach to world shorelines. *Zeitschrift Für Geomorphologie*, 127–142.

Deborde, J., Anschutz, P., Chaillou, G., Etcheber, H., Commarieu, M.-V., Lecroart, P., & Abril, G. (2007). The dynamics of phosphorus in turbid estuarine systems: Example of the Gironde estuary (France). *Limnology and Oceanography*, *52*(2), 862–872.

Defne, Z., & Ganju, N. K. (2015). Quantifying the residence time and flushing characteristics of a shallow, back-barrier estuary: Application of hydrodynamic and particle tracking models. *Estuaries and Coasts*, *38*(5), 1719–1734.

Dijkstra, Y. M., Schuttelaars, H. M., & Burchard, H. (2017). Generation of exchange flows in estuaries by tidal and gravitational eddy viscosity-shear covariance (ESCO). *Journal of Geophysical Research: Oceans*, *122*(5), 4217–4237.

Disney, J. (2015). *Frenchman Bay Partners Conservation Target Report: Mudflats*. Retrieved from www.frenchmanbaypartners.org

Doxaran, D., Froidefond, J.-M., Castaing, P., & Babin, M. (2009). Dynamics of the turbidity maximum zone in a macrotidal estuary (the Gironde, France): Observations from field and MODIS satellite data. *Estuarine, Coastal and Shelf Science*, *81*(3), 321–332.

Du, J., & Shen, J. (2016). Water residence time in Chesapeake Bay for 1980--2012. *Journal of Marine Systems*, *164*, 101–111.

Du, J., Park, K., Yu, X., Zhang, Y. J., & Ye, F. (2020). Massive pollutants released to Galveston Bay during Hurricane Harvey: Understanding their retention and pathway using Lagrangian numerical simulations. *Science of The Total Environment*, *704*, 135364.

Dyer, K. R. (1973). *Estuaries: a physical introduction*.

Egbert, G. D., & Erofeeva, S. Y. (2002). Efficient inverse modeling of barotropic ocean tides. *Journal of Atmospheric and Oceanic Technology*, *19*(2), 183–204.

Elbaz-Poulichet, F., Holliger, P., Huang, W. W., & Martin, J.-M. (1984). Lead cycling in estuaries, illustrated by the Gironde estuary, France. *Nature*, *308*(5958), 409–414.

Evans, K. S., Athearn, K., Chen, X., Bell, K. P., & Johnson, T. (2016). Measuring the impact of pollution closures on commercial shellfish harvest: The case of soft-shell clams in Machias Bay, Maine. *Ocean & Coastal Management*, *130*, 196–204.

Fitts, C. R. (2013). 11 - Groundwater Contamination. In C. R. Fitts (Ed.), *Groundwater Science (Second Edition)* (Second Edi, pp. 499–585). Boston: Academic Press. https://doi.org/https://doi.org/10.1016/B978-0-12-384705-8.00011-X

Foreman, M. G. G., & Henry, R. F. (1989). The harmonic analysis of tidal model time series. *Advances in Water Resources*, *12*(3), 109–120.

Frenchman Bay. (n.d.). Retrieved September 9, 2020, from https://coagis.maps.arcgis.com/apps/webappviewer/index.html?id=29d7fa7aeccb49d3b6ebb4906829b627

Friedrichs, C. T., & Hamrick, J. M. (1996). Effects of channel geometry on cross-sectional variations in along-channel velocity in partially stratified estuaries. *Coastal and Estuarine Studies*, 283–300.

Gerkema, T. (2019). *An introduction to tides*. Cambridge University Press.

Geyer, W R. (1997). Influence of wind on dynamics and flushing of shallow estuaries. *Estuarine, Coastal and Shelf Science*, *44*(6), 713–722.

Geyer, W Rockwell, & MacCready, P. (2014). The estuarine circulation. *Annual Review of Fluid Mechanics*, *46*, 175–197.

Geyer, W Rockwell, & Signell, R. P. (1992). A reassessment of the role of tidal dispersion in estuaries and bays. *Estuaries*, *15*(2), 97–108.

Greening, H., & Janicki, A. (2006). Toward reversal of eutrophic conditions in a subtropical estuary: Water quality and seagrass response to nitrogen loading reductions in Tampa Bay, Florida, USA. *Environmental Management*, *38*(2), 163–178.

Guo, L., der Wegen, M., Roelvink, J. A., & He, Q. (2014). The role of river flow and tidal asymmetry on 1-D estuarine morphodynamics. *Journal of Geophysical Research: Earth Surface*, *119*(11), 2315–2334.

Guo, X., & Valle-Levinson, A. (2007). Tidal effects on estuarine circulation and outflow plume in the Chesapeake Bay. *Continental Shelf Research*, *27*(1), 20–42.

Guo, X., & Valle-Levinson, A. (2008). Wind effects on the lateral structure of density-driven circulation in Chesapeake Bay. *Continental Shelf Research*, *28*(17), 2450–2471.

Haddout, S., Priya, K. L., & Ljubenkov, I. (2020). The calculation of estuarine flushing times in convergent estuaries using fresh-water fraction method. *International Journal of River Basin Management*, 1–14.

Hansen, D. V, & Rattray, M. (1965). Gravitational circulation in straits and estuaries. *J. Mar. Res.*, *23*, 104–122.

Hervouet, J.-M. (2007). *Hydrodynamics of free surface flows: modelling with the finite element method*. John Wiley & Sons.

Hillyer, G. V. (2019). Participatory Modeling of Tidal Circulation on Maine Mudflats to Improve Water Quality Management of Shellfish Areas.

Huijts, K. M. H., Schuttelaars, H. M., De Swart, H. E., & Friedrichs, C. T. (2009). *Analytical study of the transverse distribution of along-channel and transverse residual flows in tidal estuaries*. *Continental Shelf Research* (Vol. 29). Elsevier.

Iglesias, I., Almeida, C. M. R., Teixeira, C., Mucha, A. P., Magalhães, A., Bio, A., & Bastos, L. (2020). Linking contaminant distribution to hydrodynamic patterns in an urban estuary: The Douro estuary test case. *Science of The Total Environment*, *707*, 135792.

Jalón-Rojas, I., Schmidt, S., & Sottolichio, A. (2015). Turbidity in the fluvial Gironde Estuary (southwest France) based on 10-year continuous monitoring: sensitivity to hydrological conditions. *Hydrology and Earth System Sciences*, *19*(6), 2805–2819.

Janin, J. M., Lepeintre, F., & Pechon, P. (1992). *TELEMAC-3D: A finite element code to solve 3D free surface flow problems*. *Computer modelling of seas and coastal regions*. Springer.

Jiang, W., & Feng, S. (2011). Analytical solution for the tidally induced Lagrangian residual current in a narrow bay. *Ocean Dynamics*, *61*(4), 543–558.

John, S., KR, M., Azeez S, A., Cazenave, P. W., & others. (2020). What Controls the Flushing Efficiency and Particle Transport Pathways in a Tropical Estuary? Cochin Estuary, Southwest Coast of India. *Water*, *12*(3), 908.

Joyce, T. M. (1989). On in situ “calibration” of shipboard ADCPs. *Journal of Atmospheric and Oceanic Technology*, *6*(1), 169–172.

Kämpf, J., Payne, N., & Malthouse, P. (2010). Marine connectivity in a large inverse estuary. *Journal of Coastal Research*, *26*(6), 1047–1056.

Kennish, M. J. (1991). *Ecology of estuaries: anthropogenic effects* (Vol. 1). CRC press.

Kenov, I. A., Garcia, A. C., & Neves, R. (2012). Residence time of water in the Mondego estuary (Portugal). *Estuarine, Coastal and Shelf Science*, *106*, 13–22.

Kjerfve, B. (1975). Velocity averaging in estuaries characterized by a large tidal range to depth ratio. *Estuarine and Coastal Marine Science*, *3*(3), 311–323.

Klingbeil, K., Becherer, J., Schulz, E., de Swart, H. E., Schuttelaars, H. M., Valle-Levinson, A., & Burchard, H. (2019). Thickness-Weighted Averaging in tidal estuaries and the vertical distribution of the Eulerian residual transport. *Journal of Physical Oceanography*, *49*(7), 1809–1826.

Laborie, V., Ricci, S., De Lozzo, M., Goutal, N., Audouin, Y., & Sergent, P. (2020). Quantifying forcing uncertainties in the hydrodynamics of the Gironde estuary. *Computational Geosciences*, *24*(1), 181–202.

Lerczak, J. A., & Geyer, W. (2004). Modeling the lateral circulation in straight, stratified estuaries. *Journal of Physical Oceanography*, *34*(6), 1410–1428.

Li, C., & O'Donnell, J. (1997). Tidally driven residual circulation in shallow estuaries with lateral depth variation. *Journal of Geophysical Research: Oceans*, *102*(C13), 27915–27929.

Li, C., & O'Donnell, J. (2005). The effect of channel length on the residual circulation in tidally dominated channels. *Journal of Physical Oceanography*, *35*(10), 1826–1840.

Li, C., Valle-Levinson, A., Wong, K. C., & Lwiza, K. M. M. (1998). Separating baroclinic flow from tidally induced flow in estuaries. *Journal of Geophysical Research: Oceans*, *103*(C5), 10405–10417.

Lin, L., & Liu, Z. (2019). Partial residence times: determining residence time composition in different subregions. *Ocean Dynamics*, *69*(9), 1023–1036.

Liu, W.-C., Chen, W.-B., Kuo, J.-T., & Wu, C. (2008). Numerical determination of residence time and age in a partially mixed estuary using three-dimensional hydrodynamic model. *Continental Shelf Research*, *28*(8), 1068–1088.

Liu, W.-C., Ke, M.-H., & Liu, H.-M. (2020). Response of Salt Transport and Residence Time to Geomorphologic Changes in an Estuarine System. *Water*, *12*(4), 1091.

Lucas, L. V. (2010). Implications of estuarine transport for water quality. *Contemporary Issues in Estuarine Physics*, 273–303.

MacCready, P., & Geyer, W. R. (2009). Advances in estuarine physics.

McGreavy, B., Randall, S., Quiring, T., Hathaway, C., & Hillyer, G. (2018). Enhancing adaptive capacities in coastal communities through engaged communication research: Insights from a statewide study of shellfish co-management. *Ocean & Coastal Management*, *163*, 240–253.

MDMR. (n.d.). Shellfish Sanitation and Management: Maine Department of Marine Resources, Bureau of Public Health. Retrieved September 7, 2020, from https://www.maine.gov/dmr/shellfish-sanitation-management/index.html

Meyers, S. D., & Luther, M. E. (2008). A numerical simulation of residual circulation in Tampa Bay. Part II: Lagrangian residence time. *Estuaries and Coasts*, *31*(5), 815–827.

Mitra, A., Kumar, V. S., & Naidu, V. S. (2020). Circulation in the Gulf of Khambhat—A Lagrangian Perspective. *Journal of Marine Science and Engineering*, *8*(1), 25.

Moftakhari, H. R., Jay, D. A., & Talke, S. A. (2016). Estimating river discharge using multiple-tide gauges distributed along a channel. *Journal of Geophysical Research: Oceans*, *121*(4), 2078–2097.

Monsen, N. E., Cloern, J. E., Lucas, L. V, & Monismith, S. G. (2002). A comment on the use of flushing time, residence time, and age as transport time scales. *Limnology and Oceanography*, *47*(5), 1545–1553.

Moulinec, C., Denis, C., Pham, C.-T., Rougé, D., Hervouet, J.-M., Razafindrakoto, E., et al. (2011). *TELEMAC: An efficient hydrodynamics suite for massively parallel architectures*. *Computers & Fluids* (Vol. 51). Elsevier.

Nikuradse, J. (1950). *Laws of flow in rough pipes* (Vol. 2). National Advisory Committee for Aeronautics Washington.

Nixon, S. W. (1995). Coastal marine eutrophication: a definition, social causes, and future concerns. *Ophelia*, *41*(1), 199–219.

Oberkampf, W. L., DeLand, S. M., Rutherford, B. M., Diegert, K. V, & Alvin, K. F. (2002). Error and uncertainty in modeling and simulation. *Reliability Engineering \& System Safety*, *75*(3), 333–357.

Parsa, J., & Shahidi, A. E. (2010). Prediction of tidal excursion length in estuaries due to the environmental changes. *International Journal of Environmental Science & Technology*, *7*(4), 675–686.

Prandle. (2004). How tides and river flows determine estuarine bathymetries. *Progress in Oceanography*, *61*(1), 1–26.

Prieur, D., Troussellier, M., Romana, A., Chamroux, S., Mevel, G., & Baleux, B. (1987). Evolution of bacterial communities in the Gironde Estuary (France) according to a salinity gradient. *Estuarine, Coastal and Shelf Science*, *24*(1), 95–108.

Rhoads, B. L., & Kenworthy, S. T. (1998). Time-averaged flow structure in the central region of a stream confluence. *Earth Surface Processes and Landforms: The Journal of the British Geomorphological Group*, *23*(2), 171–191.

Ribeiro, D. C., Costa, S., & Guilhermino, L. (2016). A framework to assess the vulnerability of estuarine systems for use in ecological risk assessment. *Ocean & Coastal Management*, *119*, 267–277.

Ries III, K. G., Guthrie, J. D., Rea, A. H., Steeves, P. A., & Stewart, D. W. (2008). *StreamStats: A water resources web application*.

Ross, L., & Sottolichio, A. (2016). Subtidal variability of sea level in a macrotidal and convergent estuary. *Continental Shelf Research*, *131*, 28–41.

Ross, L., Valle-Levinson, A., Sottolichio, A., & Huybrechts, N. (2017). *Lateral variability of subtidal flow at the mid-reaches of a macrotidal estuary*. *Journal of Geophysical Research: Oceans* (Vol. 122). Wiley Online Library.

Sanay, R., & Valle-Levinson, A. (2005). *Wind-induced circulation in semienclosed homogeneous, rotating basins*. *Journal of physical oceanography* (Vol. 35).

Santana, R., Teixeira, C., & Lessa, G. (2018). The impact of different forcing agents on the residual circulation in a tropical estuary (Ba{\'\i}a de Todos os Santos, Brazil). *Journal of Coastal Research*, *34*(3), 544–558.

Schulz, E., Schuttelaars, H. M., Gräwe, U., & Burchard, H. (2015). Impact of the depth-to-width ratio of periodically stratified tidal channels on the estuarine circulation. *Journal of Physical Oceanography*, *45*(8), 2048–2069.

Scully, M. E., Geyer, W. R., & Lerczak, J. A. (2009). The influence of lateral advection on the residual estuarine circulation: A numerical modeling study of the Hudson River estuary. *Journal of Physical Oceanography*, *39*(1), 107–124.

Van Sebille, E., Griffies, S. M., Abernathey, R., Adams, T. P., Berloff, P., Biastoch, A., et al. (2018). Lagrangian ocean analysis: Fundamentals and practices. *Ocean Modelling*, *121*, 49–75.

Shaha, D. C., Cho, Y.-K., Kim, T.-W., & Valle-Levinson, A. (2012). Spatio-Temporal Variation of Flushing Time in the Sumjin River Estuary. *Terrestrial, Atmospheric & Oceanic Sciences*, *23*(1).

Shen, J., & Wang, H. V. (2007). Determining the age of water and long-term transport timescale of the Chesapeake Bay. *Estuarine, Coastal and Shelf Science*, *74*(4), 585–598.

Signell, R. P., & Butman, B. (1992). Modeling tidal exchange and dispersion in Boston Harbor. *Journal of Geophysical Research: Oceans*, *97*(C10), 15591–15606.

Smolders, S., Meire, P., Temmerman, S., Cozzoli, F., Ides, S., & Plancke, Y. M. G. (2013). *A 2Dh hydrodynamic model of the Scheldt estuary in 1955 to assess the ecological past of the estuary*. *XXth TELEMAC-MASCARET. User Conference 2013*.

Stacey, M. T., Burau, J. R., & Monismith, S. G. (2001). *Creation of residual flows in a partially stratified estuary*. *Journal of Geophysical Research: Oceans* (Vol. 106). Wiley Online Library.

Stammer, D., Ray, R. D., Andersen, O. B., Arbic, B. K., Bosch, W., Carrère, L., et al. (2014). Accuracy assessment of global barotropic ocean tide models. *Reviews of Geophysics*, *52*(3), 243–282.

Tassi, P., & Villaret, C. (2014). Sisyphe v6. 3 user's manual. *Recherche et Développement, Électricité de France: Chatou, France*.

Thompson, K. R., Dowd, M., Shen, Y., & Greenberg, D. A. (2002). Probabilistic characterization of tidal mixing in a coastal embayment: a Markov Chain approach. *Continental Shelf Research*, *22*(11–13), 1603–1614.

True, E. D. (2018). Using a Numerical Model to Track the Discharge of a Wastewater Treatment Plant in a Tidal Estuary. *Water, Air, & Soil Pollution*, *229*(8), 267.

Tsanis, I. K. (1989). Simulation of wind-induced water currents. *Journal of Hydraulic Engineering*, *115*(8), 1113–1134.

Uittenbogaard, R. E. (1994). Testing some Damping Functions for Mixing Length Turbulence Models. *Delft Hydraulics, Rep., Z721*.

Valle-Levinson, A. (2010). *Contemporary issues in estuarine physics*. Cambridge University Press.

Valle-Levinson, A., Reyes, C., & Sanay, R. (2003). *Effects of bathymetry, friction, and rotation on estuary--ocean exchange*. *Journal of Physical Oceanography* (Vol. 33).

Wan, Y., Qiu, C., Doering, P., Ashton, M., Sun, D., & Coley, T. (2013). Modeling residence time with a three-dimensional hydrodynamic model: Linkage with chlorophyll a in a subtropical estuary. *Ecological Modelling*, *268*, 93–102.

Willmott, C. J. (1981). On the validation of models. *Physical Geography*, *2*(2), 184–194.

Winant, C. D. (2008). *Three-dimensional residual tidal circulation in an elongated, rotating basin*. *Journal of Physical Oceanography* (Vol. 38).

Wong, K.-C. (1994). *On the nature of transverse variability in a coastal plain estuary*. *Journal of Geophysical Research: Oceans* (Vol. 99). Wiley Online Library.

Yuan, D., Lin, B., & Falconer, R. A. (2007). A modelling study of residence time in a macro-tidal estuary. *Estuarine, Coastal and Shelf Science*, *71*(3–4), 401–411.

Zhu, J., Weisberg, R. H., Zheng, L., & Han, S. (2015). On the flushing of Tampa Bay. *Estuaries and Coasts*, *38*(1), 118–131.

Zimmerman, J T F. (1978). *Topographic generation of residual circulation by oscillatory (tidal) currents*. *Geophysical & Astrophysical Fluid Dynamics* (Vol. 11). Taylor & Francis.

Zimmerman, J T F. (1979). On the Euler-Lagrange transformation and the Stokes' drift in the presence of oscillatory and residual currents. *Deep Sea Research Part A. Oceanographic Research Papers*, *26*(5), 505–520.

Zimmerman, J T F. (1981). Dynamics, diffusion and geomorphological significance of tidal residual eddies. *Nature*, *290*(5807), 549–555.

Zimmerman, Joseph Theodoor Frans. (1976). Mixing and flushing of tidal embayments in the western Dutch Wadden Sea part I: Distribution of salinity and calculation of mixing time scales. *Netherlands Journal of Sea Research*, *10*(2), 149–191.

Zitman, T. J., & Schuttelaars, H. M. (2012). Importance of cross-channel bathymetry and eddy viscosity parameterisation in modelling estuarine flow. *Ocean Dynamics*, *62*(4), 603–631.

BIOGRAPHY OF THE AUTHOR

Sohaib Alahmed was born in Mosul city in the Northern Iraq on June 13, 1989. He attended the University of Mosul in 2007 and graduated with a Bachelor's degree in water resources engineering. Alahmed earned his Master of Science from University of Maine in civil and environmental engineering in 2017. Then he earned his Ph.D. from the same school in 2021. Alahmed attended the Summer school in Friday Harbor Lab, University of Washington in 2019. Over the course of his Ph.D. study, Alahmed was awarded with David spencer fellowship for sustainability (2020), Chase award (2019) and The University of Maine Trustee scholarship (2018-2019). Alahmed is a candidate for the a doctoral degree in civil and environmental engineering from the University of Maine in May 2021.